Università degli Studi di Padova

Dipartimento di Fisica e Astronomia "Galileo Galilei"

Corso di Dottorato di Ricerca in Astronomia

XXXVI Ciclo

Multiple Populations in Globular Clusters: Investigating the Uncharted Territories with Photometry

Coordinator: Prof. Giovanni Carraro

Supervisor: Prof. Antonino P. Milone

Co-supervisors: Dott.ssa Anna F. Marino

Dott. Edoardo P. Lagioia

Ph.D. candidate: Emanuele Dondoglio

Contents

Abstract

As established by decades of observational studies, Globular Clusters' (GCs) stars exhibit light-elements variation. Combined spectroscopy, photometry, and modeling efforts revealed that these chemical inhomogeneities arise from GCs harboring multiple stellar populations. While a fraction shares the chemical composition with stars typically found in the Galactic halo, the rest present unexpected abundances of light elements such as helium, carbon, nitrogen, oxygen, and sodium. This latter group of stars has been detected only inside GCs and in no other structure in the Universe. Their origin is nowadays an unresolved riddle of stellar astrophysics.

The theoretical framework predicts that the stars with peculiar abundances formed from a gas polluted by massive stars. The several polluters proposed throughout the years have different implications that impact multiple research fields, such as stellar evolution, galaxy assembly, and cosmology. However, none of the proposed scenarios can provide a fulfilling explanation of all the observed features of the multiple populations.

Understanding the phenomenon is a mandatory step to shed light on the formation and evolution of GCs and their contribution to building the galaxies and, therefore, shaping the Universe we observe today. Driven by this need, this thesis focuses on revealing new sides of multiple populations by exploiting multi-band photometry -from UV to NIR- taken from several facilities. This work aims to tackle different aspects of this enigma, providing novel constraints for theoretical scenarios. Three main projects constitute the body of my work during the three years of my Ph.D., which are the following:

(i) The first focuses on the red Horizontal Branch (HB) and the red clump stars, defining a new set of tools to analyze the phenomenon. UV photometry (both space- and ground-based) is effective in spotting multiple populations among metal-rich GCs in these evolutionary phases and revealing them when Red Giant Branch (RGB) photometry - typically used for this kind of investigation - does not allow a clear separation between chemically different populations. The red HB and red clump stars also allow exploring several aspects of the phenomenon, such as its link with the host galaxy, the radial

distribution of the multiple populations, and the chemical inhomogeneities among the stars without peculiar light-elements variations.

(ii) Secondly, I explored the Very-Low Mass (VLM) regime of Galactic GCs thanks to *H*ubble Space Telescope (HST) NIR photometry, detecting in all of them the phenomenon even among these particularly faint stars. For two of the GCs in our sample, the combination of this dataset with optical and UV photometry disentangles chemically different populations among the whole Main Sequence (MS). The properties of the phenomenon do not vary within this stellar mass range, as proven by the lack of differences between their Mass Function (MF) slopes and their constant ratios. These results have implications for constraining the formation scenarios and the nature of the initial MF of the multiple stellar populations.

(iii) The third project concerns the Type II GCs, a subclass of clusters that, beyond the light-elements variations, can also exhibit a spread in heavier elements, such as [Fe/H] and s-process elements, and in total C+N+O amount. Here, I show the case of NGC 1851, for which it is performed the most-detailed photometric analysis on Type II GCs yet, defining new tools to study this class of objects. This analysis disentangled four subpopulations and revealed their chemical composition by combining the information from photometry with spectroscopy measurements and stellar spectra. Moreover, the multi-facility approach employed in this work allows the investigation of the spatial and radial distribution of all the populations in NGC 1851 from the center up to beyond the tidal radius.

List of Publications

During my PhD, I participated in a total amount of 23 published papers (plus one accepted for publication) with more than 250 overall citations. In particular, I published three works as the first author and one conference proceeding. In the following, I list these papers (as also visible in the NASA ADS database) in chronological order, from the most recent to the oldest:

1 **Dondoglio et al. (2023)**: *"A deep dive into the Type II Globular Cluster NGC 1851"*, MNRAS, 526, 2960.
Link: https://ui.adsabs.harvard.edu/abs/2023MNRAS.526.2960D/abstract

2 **Mohandasan et al. (2023)**: *"Photometric Binaries in 14 Magellanic Cloud Star Clusters"*, accepted for publication on A&A.
Link: https://ui.adsabs.harvard.edu/abs/2023arXiv231015345M/abstract

3 **Marino et al. (2023)**: *"The Metallicity Variations Along the Chromosome Maps: The Globular Cluster 47 Tucanae"*, ApJ, 958, 31.
Link: https://ui.adsabs.harvard.edu/abs/2023ApJ...958...31M/abstract

4 **Milone et al. (2023)**: *"Hubble Space Telescope survey of Magellanic Cloud star clusters: UV-dim stars in young clusters"*, MNRAS, 524, 6149.
Link: https://ui.adsabs.harvard.edu/abs/2023MNRAS.524.6149M/abstract

5 **Cordoni et al. (2023)**: *"Multiple stellar populations found outside the tidal radius of NGC 1851 via Gaia DR3 XP spectra"*, A&A, 678, 155.
Link: https://ui.adsabs.harvard.edu/abs/2023A%26A...678A.155C/abstract

6 **Ziliotto et al. (2023)**: *"Multiple Stellar Populations in Metal-poor Globular Clusters with JWST: A NIRCam View of M92"*, ApJ, 953, 62.
Link: https://ui.adsabs.harvard.edu/abs/2023ApJ...953...62Z/abstract

7 **Milone et al. (2023)**: *"Multiple stellar populations in globular clusters with JWST: an NIRCam view of 47 Tucanae"*, MNRAS, 522, 2429.
Link: https://ui.adsabs.harvard.edu/abs/2023MNRAS.522.2429M/abstract

8 **Legnardi et al. (2023)**: *"Differential reddening in the direction of 56 Galactic globular clusters"*, MNRAS, 522, 367.
Link: https://ui.adsabs.harvard.edu/abs/2023MNRAS.522.2429M/abstract

9 **Milone et al. (2023)**: *"Hubble Space Telescope survey of Magellanic Cloud star clusters. Photometry and astrometry of 113 clusters and early results"*, A&A, 672, 161.
Link: https://ui.adsabs.harvard.edu/abs/2023A%26A...672A.161M/abstract

10 **Cordoni et al. (2023)**: *"Photometric binaries, mass functions, and structural parameters of 78 Galactic open clusters"*, A&A, 672, 29.
Link: https://ui.adsabs.harvard.edu/abs/2023A%26A...672A..29C/abstract

11 **Carlos et al. (2023)**: *"The chemical compositions of multiple stellar populations in the globular cluster NGC 2808"*, MNRAS, 519, 1695.
Link: https://ui.adsabs.harvard.edu/abs/2023MNRAS.519.1695C/abstract

12 **Jang et al. (2022)**: *"Chromosome maps of globular clusters from wide-field ground-based photometry"*, MNRAS, 517, 5687.
Link: https://ui.adsabs.harvard.edu/abs/2022MNRAS.517.5687J/abstract

13 **Cordoni et al. (2022)**: *"NGC1818 unveils the origin of the extended main-sequence turn-off in young Magellanic Clouds clusters"*, Nat. Commun., 13, 4325.
Link: https://ui.adsabs.harvard.edu/abs/2022NatCo..13.4325C/abstract

14 **Legnardi et al. (2022)**: *"Constraining the original composition of the gas forming first-generation stars in globular clusters"*, MNRAS, 513, 735.
Link: https://ui.adsabs.harvard.edu/abs/2022MNRAS.513..735L/abstract

15 **Dondoglio et al. (2022)**: *"Survey of Multiple Populations in Globular Clusters among Very-low-mass Stars"*, ApJ, 927, 207.
Link: https://ui.adsabs.harvard.edu/abs/2022ApJ...927..207D/abstract

16 **Marino et al. (2021)**: *"Spectroscopy and Photometry of the Least Massive Type II Globular Clusters: NGC 1261 and NGC 6934"*, ApJ, 923, 22.
Link: https://ui.adsabs.harvard.edu/abs/2021ApJ...923...22M/abstract

17 **Jang et al. (2021)**: *"Integrated Photometry of Multiple Stellar Populations in Globular Clusters"*, ApJ, 920, 129.
Link: https://ui.adsabs.harvard.edu/abs/2021ApJ...920..129J/abstract

18 **Tailo et al. (2021)**: *"Mass-loss law for red giant stars in simple population globular clusters"*, ApJ, 503, 694.
Link: https://ui.adsabs.harvard.edu/abs/2021MNRAS.503..694T/abstract

19 **Lagioia et al. (2021)**: *"Multiple Stellar Populations in Asymptotic Giant Branch Stars of Galactic Globular Clusters"*, ApJ, 910, 6.
Link: https://ui.adsabs.harvard.edu/abs/2021ApJ...910....6L/abstract

20 **Dondoglio et al. (2021)**: *"Multiple Stellar Populations along the Red Horizontal Branch and Red Clump of Globular Clusters"*, ApJ, 906, 76.
Link: https://ui.adsabs.harvard.edu/abs/2021ApJ...906...76D/abstract

21 **Tailo et al. (2020)**: *"Mass-loss along the red giant branch in 46 globular clusters and their multiple populations"*, MNRAS, 498, 5745.
Link: https://ui.adsabs.harvard.edu/abs/2020MNRAS.498.5745T/abstract

22 **Milone et al. (2020)**: *"A chromosome map to unveil stellar populations with different magnesium abundances. The case of ω Centauri"*, MNRAS, 497, 3846.
Link: https://ui.adsabs.harvard.edu/abs/2020MNRAS.497.3846M/abstract

23 **Cordoni et al. (2020)**: *"Gaia and Hubble Unveil the Kinematics of Stellar Populations in the Type II Globular Clusters ω Centauri and M22"*, ApJ, 898, 147.
Link: https://ui.adsabs.harvard.edu/abs/2020ApJ...898..147C/abstract

24 **Milone et al. (2020)**: *"Multiple populations in globular clusters and their parent galaxies"*, MNRAS, 491, 515.
Link: https://ui.adsabs.harvard.edu/abs/2020MNRAS.491..515M/abstract

CHAPTER 1

INTRODUCTION

Globular Clusters (GCs) have been, and currently are, one of the most reliable tools in Astronomy. They are the birthplace of thousands to millions of stars, which are gravitationally bound to compose a very dense environment in a limited space, allowing us to study a plenteousness of stars with minimum observational efforts. Being such crowded and rich celestial objects, GCs have implications in several research topics, from stellar astrophysics to galaxy formation, passing through planetary exploration, cosmology, and black hole physics. Moreover, they were also instrumental in testing evolutionary models that aimed at predicting the behavior of a stellar population. Thanks to the proximity of some of the Galactic GCs, we had, in the past century, the opportunity to explore their nature with increasing details as telescopes became more and more powerful. Moreover, the improvement brought by technological advances allowed astronomers to move further away, reaching these structures in galaxies outside our Milky Way.

To date, every galaxy in the Universe is believed to harbor, during its lifetime, a population of GCs. Intriguingly, they are as old as or even older than their host galaxy, thus making them strong candidates in shaping the galaxies -and the Universe- that we observe today. Many GCs, such as the ones populating the Milky Way, are the oldest objects for which we can measure age, reaching 12-13 Gyr, hence making them relics of the earliest phases of the Universe's life, where most of the first stars that ever lit the cosmos were born. From a cosmological standpoint, their old age also puts them in the picture of having a role in the re-ionization of the Universe.

Notwithstanding the towering amount of studies carried out on these objects, many fundamental questions about their nature are still unanswered. Indeed, a complete picture of the formation and subsequent evolution of GCs is still lacking, as well as an

understanding of their role in building galaxies. Shedding light on these issues requires a combined effort from stellar photometry, spectroscopy, and dynamics, but also from galaxy evolution and cosmology, and synergy between observations and theoretical predictions, making the GCs field a crossroads of different research topics.

The framework of the extensively studied yet mysterious GCs got further complicated by the fact that these structures are not composed, as classically believed, of a single stellar population (i.e., with the same age and chemical composition) but harbor several groups of stars with chemical anomalies, in what has been dubbed the *multiple stellar populations phenomenon*. This finding revolutionized our conception of GCs and constitutes one of the most intriguing and challenging duties of stellar astrophysics.

All our questions on the formation and evolution of GCs necessarily pass through the explanation of the presence of this unique phenomenon, making the multiple populations' enigma a mandatory step in reconstructing the chain of events that led to shaping the Universe that we observe today.

1.1 Multiple Populations in Globular Clusters

The first observational pieces of evidence of chemical inhomogeneities among GC stars come from the late seventies and have been confirmed by subsequent spectroscopic studies in the following years, which detected star-to-star variations in the strengths of the CH, CN, and NH molecular absorption bands, as well as their sodium and oxygen abundances, in several GCs, such as NGC 104 (47 Tuc), NGC 5272, NGC 6121 (M4), NGC 6205, NGC 7078, NGC 6838, NGC 6341, and NGC 6752 (e.g., Cohen, 1978; Cottrell & Da Costa, 1981; Norris, 1981; Norris & Freeman, 1982; Smith & Penny, 1989; Brown et al., 1991; Sneden et al., 1991; Kraft et al., 1992). The general picture that arose from these studies was that the chemical variations were not random but displayed carbon-nitrogen and sodium-oxygen abundance anticorrelations, such that the stars with unusually high nitrogen and sodium also exhibit lower oxygen and carbon content.

These works raised the concern that in GCs, some unknown mechanisms were acting to produce the observed abundance anticorrelations. At the time, since the detection of the phenomenon was limited to giant stars, the possibility that some still-to-know stellar evolution mechanism formed these stars, rather than having a primordial origin and constituting a fully separated population of stars, was still particularly appealing and debated (see Smith & Tout, 1992; Kraft, 1994).

Later, the advent of new and more powerful telescopes opened the exploration of larger samples of stars, with more detail and down to fainter magnitudes. The presence of light element variations was at this point well established as a common characteristic of Galactic GCs, with the phenomenon being detected among several evolutionary phases, from the bright giant stars in the Red Giant Branch (RGB) and Horizontal Branch (HB) to the fainter stars in the Sub-Giant Branch (SGB) and even among the brightest members of the Main Sequence (MS; e.g., Briley et al., 2004; Carretta et al., 2009b,a; Marino et al., 2011b; Gratton et al., 2012b; Lardo et al., 2012). These works

seriously challenged the idea that the chemical inhomogeneities had an evolutionary origin, favoring a primordial provenance and, therefore, a picture where GCs host different populations: a group of stars with chemical abundances similar to halo field stars and another with peculiar chemical composition, enhanced in nitrogen, sodium, and aluminum, and depleted in carbon, oxygen, and magnesium. Intriguingly, this latter population shows, among some of the studied clusters, signs of being composed of more than one population, displaying different extensions of the anticorrelation patterns (see Gratton et al., 2012a, for a review on the framework arose from spectroscopy at the time).

Meanwhile, the *Hubble Space Telescope (HST)* provided photometry with unprecedented quality, allowing studying the phenomenon also from a photometric standpoint over a large set of filters, ranging from UV to NIR wavelengths. First glances of the power of the *HST* came from analyzing NGC 5139 (ωCen) and NGC 2808, where separated MSs, associated with different helium abundances, were detected by exploiting optical CMDs (Bedin et al., 2004; Piotto et al., 2007). Smaller spread among MS stars, interpreted as smaller helium variations, has also been found in 47 Tuc, NGC 6752, and NGC 6397 (Anderson et al., 2009; Milone et al., 2010, 2012c). These results provided the first evidence of a helium heterogeneity among GC stars, a feature that is particularly challenging to observe through spectroscopy[1]. The comparison of these results with spectroscopy and stellar models revealed that the stars with peculiar chemical composition are also enhanced in helium (e.g., Milone et al., 2012a).

A game-changing contribution came from the WFC3/UVIS camera onboard the *HST* and its capability to retrieve accurate photometry in the UV regime. Indeed, this wavelength range encompasses the absorption bands of the CN, CH, NH, and OH molecules, thus allowing photometry to spot differences in the carbon, nitrogen, and oxygen abundances. In particular, the F275W, F336W, and F438W (and F343N, F410M, F435W) filters are an exquisite tool for separating populations with different light-elements abundances, as shown by Sbordone et al. (2011) utilizing synthetic spectra. An example of the power of this approach comes from Milone et al. (2012b), who analyzed 47 Tuc with this set of filters, detecting two separate sequences among the MS, SGB, RGB, and HB stars. By comparing their findings with synthetic spectra, they concluded that two main populations are harbored by this cluster: a first one with primordial helium abundance and carbon, nitrogen, and oxygen abundances similar to field stars, and a second one made by stars enriched in helium and nitrogen and depleted in carbon and oxygen. Similarly to spectroscopy, even through photometry, it was possible to identify the multiple populations in basically every analyzed Galactic GC. Currently, the most effective tool to do that is the Chromosome Map (ChM), a pseudo-two-color diagram that combines information from several UV and optical photometric *HST* filters to maximize the separation between stellar populations that differ in their helium, carbon, nitrogen, and oxygen content (see Milone et al., 2015, 2017a). In this diagram, a single stellar

[1] Direct spectroscopic helium evidences are rare since reliable estimates from spectral lines are limited only for HB stars with effective temperature ($T_{\rm eff}$) in the ∼8000-11,500 K range. Indeed, colder stars do not exhibit strong enough helium lines, whereas hotter stars experience the gravitational settling of helium atoms, that diffuse inwards in the star depleting its abundance in the atmosphere, thus leading to helium underestimations in spectroscopic observations (e.g., Michaud et al., 1983; Behr, 2003).

population would form a blob as extended as the observational errors clustered around its origin, a behavior that no massive Galactic GC shows, presenting instead several distinct elongated aggregations of stars, as I will discuss later on in this Chapter. Furthermore, studies of multiple populations were also extended to ground-based photometry, with several works that proved how high-quality UBVI multi-band observations can disentangle stars with differences in their helium, carbon, nitrogen, and oxygen abundances (e.g., Marino et al., 2008; Monelli et al., 2013; Stetson et al., 2019; Jang et al., 2022).

From now on, it was possible to identify the different populations within GCs with both spectroscopy and photometry, hence combining the precise chemical tagging provided by the former with the ability to analyze efficiently a huge number of cluster stars provided by the latter. The following bullet list summarizes the main features of the multiple populations in GCs found by observational studies:

- **Two main populations.** GCs are populated by two main groups of stars, usually referred to as first and second generations (1G and 2G; or populations, 1P and 2P), differing in their light-element abundances. The former share a similar chemical composition to field stars with equal metallicity, whereas the latter presents the peculiar patterns introduced before in this Section. These stars can be detected by both spectroscopy and photometry, as illustrated in Figure 1.1, which displays the ChM (left panel) from Milone et al. (2017a) and the [Na/Fe] vs. [O/Fe] (right panel) from Carretta et al. (2009b) diagrams for RGB stars in NGC 288. In this ChM, 1G stars lie below $\Delta_{\rm CF275W,F343N,F438W}$ $\sim$0.1, while 2G stars form the cloud of points at y-axis values larger than $\sim$0.2. The encircled stars in the ChM have available sodium and oxygen abundances from spectroscopy and are colored in green and azure whether they belong to the 1G or 2G populations, respectively. In the [Na/Fe] vs. [O/Fe] plane, 2G stars display, on average, higher sodium and lower oxygen than 1G stars. This comparison, performed by Marino et al. (2019a) for 29 Galactic GCs, proves the existence of a strong link between the differences in chemical abundances and the separate sequences observed in photometric diagrams.

- **A widespread phenomenon (but only in GCs).** The presence of the multiple populations phenomenon has been observed to be a common characteristic of old and massive GCs, being detected both with photometry and spectroscopy in the large majority of the studied objects (e.g., Carretta et al., 2009b; Milone et al., 2017a; Marino et al., 2019a). The only Galactic GCs without sign of chemical anomalies are the least massive ones, thus suggesting a threshold in their initial mass, around $1.5\times10^5 M_\odot$, for its manifestation (e.g., Bragaglia et al., 2012; Milone et al., 2020a). Notably, multiple populations have been observed only within GCs, not being found, to date, in any other structure in the Universe. Indeed, analyses of halo field stars in our galaxy showed that the contribution of 2G stars is way smaller than in GCs, and it is consistent with them originating within GCs and then escaping (e.g., Vesperini et al., 2010; Martell et al., 2011).

- **Present in several evolutionary phases.** The presence of multiple populations

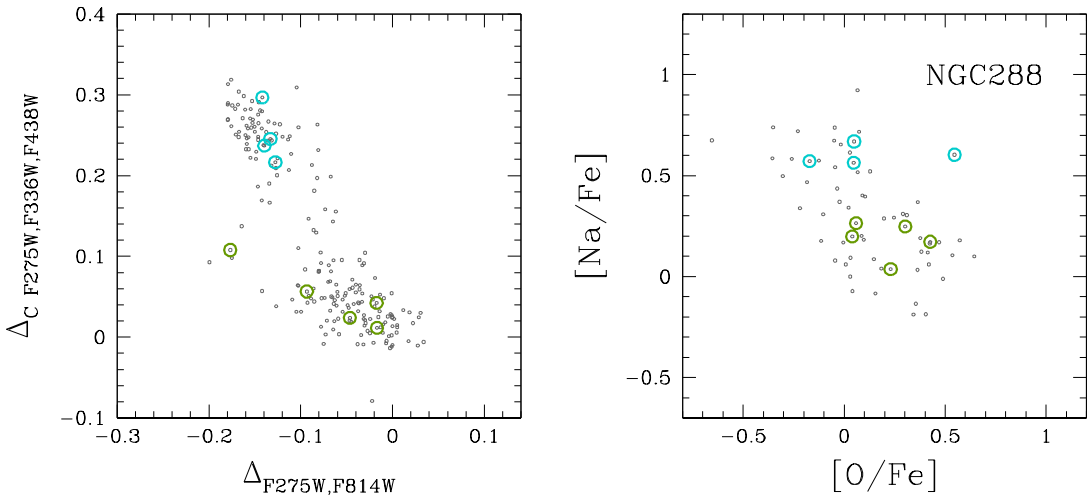

Figure 1.1: *Left Panel:* $\Delta_{CF275W,F336W,F438W}$ vs. $\Delta_{F275W,F814W}$ ChM for the RGB stars of NGC 288 (from Milone et al., 2017a). *Right Panel:* [Na/Fe] vs. [O/Fe] diagram from Carretta et al. (2009b) spectroscopy. Stars encircled in green and azure represent the 1G and 2G stars in common between the two datasets, respectively. (Result taken from Marino et al. (2019a)).

has been detected in stars from several evolutionary phases, namely the MS, SGB, RGB, HB, and AGB. In Figure 1.2, 47 Tuc is used as a template to prove that. The upper-left panel presents the ChM of RGB and Asymptotic Giant Branch (AGB) stars superimposed in black and red, respectively, while the upper-right panel displays the same diagram for MS stars. Here, 1G stars form the elongated distribution centered at around $\Delta_{CF275W,F343N,F438W}$ ∼0.05, while the cloud of stars at higher y-axis values is composed of 2G stars.

Lower-left and -right panels illustrate the separated sequences among SGB and HB stars, respectively, thanks to the $m_{F343N} - m_{F435W}$ vs. $m_{F275W} - m_{F343N}$ two-color diagram. In this plane, 1G stars describe the sequences with redder F275W-F343N and bluer F343N-F435W colors, while the remaining sequence is populated by 2G stars.

The presence of multiple populations in every observed evolutionary phase is a common characteristic of the phenomenon, being observed in all the clusters for which data allowed this kind of exploration (e.g., Milone et al., 2017a; Lagioia et al., 2021; Dondoglio et al., 2021, 2022).

- **Discreteness.** The chemical variations between 1G and 2G stars do not show continuous patterns but form well-separated groups with different chemical abundances and positions on the appropriate diagrams. This feature is evident from Figure 1.1 and 1.2, where the two groups of stars form discrete distributions in the ChM and two-color diagrams, as found in several studies based on UV photometry (e.g., Milone et al., 2012b; Piotto et al., 2015; Milone et al., 2017a).

To further highlight this feature, (Marino et al., 2019a) introduced the so-called universal ChM, a normalized diagram built by removing the [Fe/H] effect on the ChM extension, thus allowing for a direct comparison between different GCs. By combining the information from all the normalized ChMs, the 1G and 2G sequences exhibit a net separation between their distributions, thus indicating that the stellar formation did not proceed continuously.

- **Variety.** A peculiarity of this phenomenon is that it manifests quite differently among GCs. Indeed, their 1G-2G patterns display dramatic variations in their distribution within spectroscopic and photometric diagrams. An example is given by the collection of ChMs presented by Milone et al. (2017a). Figure 1.3 illustrates the cases of NGC 6838, NGC 6205, and NGC 2808 (upper-left and -right, and lower, respectively) as an example. NGC 6838 exhibits a relatively simple ChM, with 2G forming a single well-separated blob from the 1G stars. NGC 6205 is a more complex case, showing a 2G sequence elongated along the y-axis, thus indicating internal light-element variations, and with a less clear-cut separation from the bulk of 1G stars. Finally, NGC 2808 represents the most complex GC of the three, with its 2G population forming three separated clumps of stars - at ($\Delta_{\rm F275W,F814W}$, $\Delta_{\rm CF275W,F336W,F438W}$) $\sim$(-0.15,0.20), $\sim$(-0.35,0.35), and $\sim$(-0.55,0.45)- hence hosting at least three different 2G populations. Furthermore, the elongation of the 1G sequence changes, with NGC 6838 and NGC 2808 exhibiting an extended 1G stars distribution in the $\Delta_{\rm F275W,F814W}$ direction, while this phenomenon is not present in NGC 6205 (see the '1G spread' point below).

- **Incidence of multiple populations.** From a visual inspection of Figure 1.3, one can notice that the fraction of 1G and 2G stars massively changes among different GCs, with NGC 6838 displaying a higher contribution of 1G stars than NGC 6205 and NGC 2808, where this population constitutes a minority of cluster stars. As found by Milone et al. (2017a), the fraction of 1G stars among Galactic GCs ranges from $\sim$0.1 to $\sim$0.7, with 2G stars dominating in most of them.

  Figure 1.4 shows the fraction of 1G stars to the mass of the host cluster. This comparison tells us that the more massive a GC is, the higher the 2G stars' incidence, with only a minor part belonging to the 1G population. On the contrary, the Galactic GCs where 1G stars dominate are all less massive than $\sim 2\times10^5 M_\odot$.

- **Radial distribution.** Particularly interesting is the radial distribution of the different populations because it can be a tool to test the multiple-populations formation scenarios. Indeed, many theories predict that 2G stars form in a more centrally-concentrated environment, originating in the innermost area embedded in a more extended 1G stars distribution (see Section 1.2). This prediction is fulfilled in some clusters, whereas in others 1G and 2G stars share the same radial distribution (e.g., Milone et al., 2012b; Lee, 2017; Cordero et al., 2014; Simioni et al., 2016; Dalessandro et al., 2018; Milone et al., 2019; Dondoglio et al., 2021; Leitinger et al., 2023). In a scenario where radial differences were present in the first epochs of a GC life,

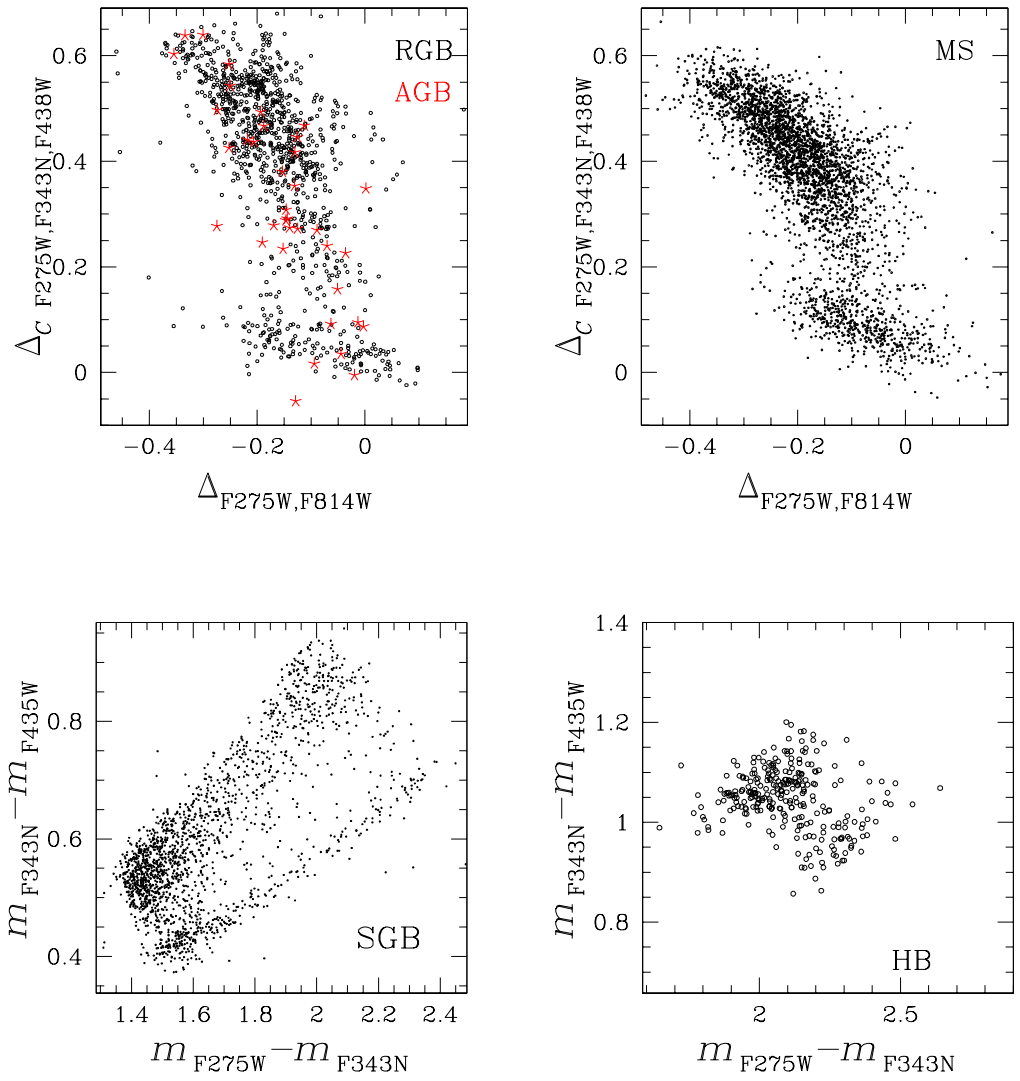

Figure 1.2: *Upper-left Panel:* superimposed $\Delta_{\mathrm{CF275W,F336W,F438W}}$ vs. $\Delta_{\mathrm{F275W,F814W}}$ ChMs for the RGB stars (black dots) and AGB stars (red starred symbols) of 47 Tuc. *Upper-right Panel:* ChM of the bright MS stars. *Lower-left and -right Panels:* $m_{\mathrm{F343N}} - m_{\mathrm{F435W}}$ vs. $m_{\mathrm{F275W}} - m_{\mathrm{F343N}}$ two-color diagrams of SGB and HB stars, respectively. (Image taken from Milone & Marino (2022)).

clusters with well-mixed populations would have seen their initial spacial differences erased by internal dynamical evolution and/or tidal effects. Peculiar cases, where 1G stars unexpectedly appear more centrally concentrated than 2G stars, have been detected by Leitinger et al. (2023).

- **1G spread.** Not only the 2G stars host internal chemical spreads and subpopula-

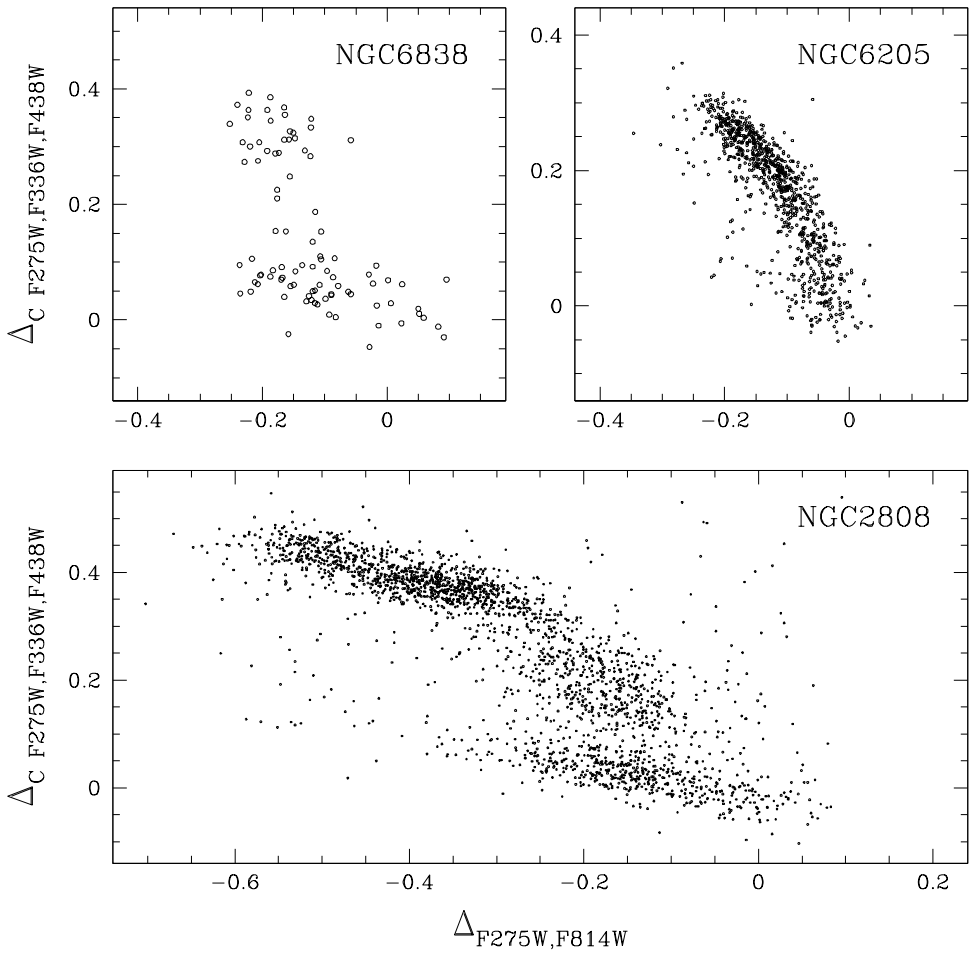

Figure 1.3: ChMs of NGC 6838 (upper-left), NGC 6205 (upper-right), and NGC 2808 (lower panel).

tions, but also the 1G stars can exhibit chemical homogeneity. This feature was firstly noted by Milone et al. (2017a), who found that the 1G sequence of many GCs in their sample is more elongated along the x-axis of the ChM than what was expected by observational errors only (see the ChMs of NGC 6838 and NGC 2808 in Figure 1.3). The phenomenon was also detected among red HB and MS stars (Dondoglio et al., 2021; Legnardi et al., 2023). In particular, the finding of this feature among unevolved MS stars suggests that this is due to chemical inhomogeneity in the primordial cloud from which GCs formed. Works based on high-resolution spectroscopy of 1G stars found that iron variations may be the main responsible for this phenomenon, as detected in NGC 3201 and 47 Tuc (Marino et al., 2019b, 2023), who measured a [Fe/H] spread of ∼0.1 dex.

- **Dependence on stellar mass.** The incidence of the multiple stellar populations phenomenon does not appear to be related to the stellar mass. Indeed, the fraction of 1G and 2G stars among GCs does not vary when considering different stellar mass

regimes. Milone et al. (2019) and Dondoglio et al. (2022) found no differences between their fractions in NGC 6752, NGC 2808 and M4 along a $\sim$0.2-0.8 $\mathcal{M}_{\odot}$ mass interval, and the fractions inferred by Milone et al. (2020b) in NGC 288, M4, NGC 6352, NGC 6362, and NGC 6838 among MS stars are consistent within error bars with what found among giant stars (Milone et al., 2017a; Dondoglio et al., 2021).

- **Kinematics.** Investigating the internal motion of the distinct stellar populations that inhabit GCs can provide insights into the proto GCs and their initial properties (e.g. Vesperini et al., 2013; Mastrobuono-Battisti & Perets, 2013, 2016). The high-precision Gaia proper motions and radial velocities (Gaia Collaboration et al., 2018, 2021), combined with the proper motions measurable from multi-epoch *H*ST images, ensure precise measurements of kinematical properties of stellar populations such as their velocity and velocity dispersion. 2G stars of some GCs have more radially anisotropic velocity distributions than the 1G, which is consistent with a scenario where 2G stars formed in a more centrally-concentrated environment and are diffusing towards the outer regions as a result of the GCs' dynamical evolution. On the other hand, other clusters do not exhibit any kinematic differences between 1G and 2G stars, which suggests that any initial differences, if present, have been erased as a result of dynamical evolution (Richer et al., 2013; Bellini et al., 2015; Cordoni et al., 2020).

- **Multiple populations outside the Milky Way.** The increasing quality of telescopes and data analysis techniques allowed us to move beyond our galaxy and explore the neighboring galaxies. Magellanic Clouds clusters are the closest extragalactic GCs and, therefore, the most extensively explored. The detection of multiple populations among the RGB and HB stars of several massive Large and Small Magellanic Clouds (SMC and LMC) GCs was instrumental in extending the study of the phenomenon down to younger ages, which is not possible in the 10-12 Gyr old Galactic GCs, and to detect the presence of multiple populations in clusters down to $\sim$2 Gyr old (e.g., Mucciarelli et al., 2009; Dalessandro et al., 2016; Niederhofer et al., 2017; Martocchia et al., 2018a; Lagioia et al., 2019a; Milone et al., 2020a). Below this threshold, no light-element chemical variation has been detected (with the possible exception of NGC 1783, see Cadelano et al. 2022), thus hinting the presence of an age threshold for the multiple populations phenomenon (e.g., Martocchia et al., 2018b, 2019). Intriguingly, these GCs (displayed as red dots in Figure 1.4) exhibit a higher 1G fraction than the Milky Way ones with similar masses, and this population, on the contrary of Galactic GCs, constitute the majority of their stars (e.g., Milone et al., 2020a; Dondoglio et al., 2021).

  Signs of the presence of multiple populations were also found among GCs in the Fornax Galaxy and M31 (e.g., Larsen et al., 2014; Nardiello et al., 2019), even though their further distances make particularly challenging and expensive in terms of observational efforts to analyze their multiple populations with such accuracy as

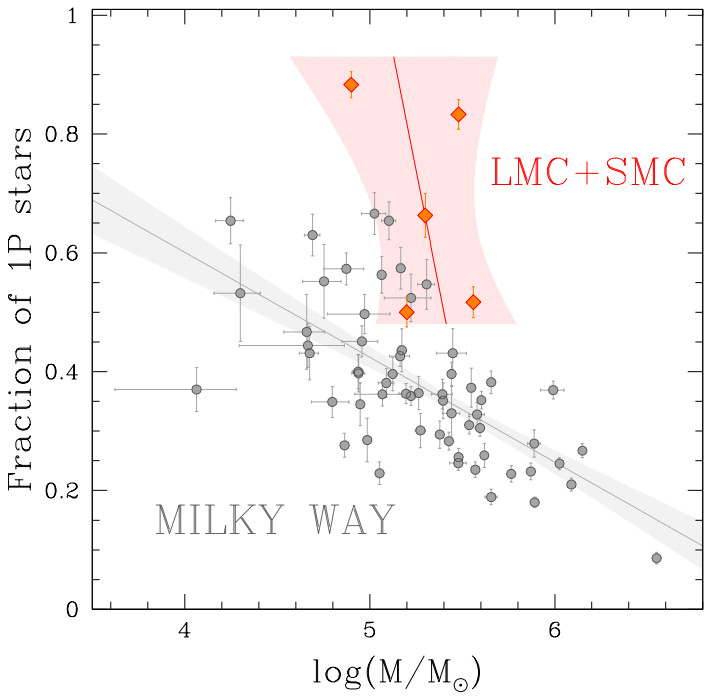

Figure 1.4: Fraction of 1G stars with respect to the mass of the host GC. Gray dots represent the Galactic ones, while in red are displayed the LMC and SMC clusters. The two lines are the linear interpolations of the two groups of clusters, while the relative shaded areas represent the slope uncertainties. (Image taken from Milone & Marino (2022))

in our galaxy and in the Magellanic Clouds.

1.2 Scenarios for the Formation of Multiple Populations

Why do we observe multiple populations in GCs?

This question encapsulates all this research field, and it is currently unanswered. To address the issue, many different theories have been formulated since the early eighties up to the present day. A satisfactory formation scenario should be able to justify all the observational shreds of evidence summarized in the previous Section.

The idea that the chemical anomalies had an evolutionary origin was appealing during the first years of exploration since it would keep the classical paradigm of GCs formed as a single stellar population. However, multiple discoveries from the past ∼20 years proved that the phenomenon occurs also among unevolved MS stars (discussed in the previous Section) led astronomers to abandon this idea in favor of formation scenarios where 1G and 2G stars constitutes separated populations originated in the early phases of a cluster's life.

The observed chemical anomalies involve sodium, aluminum, and magnesium, which

are typically produced by the nuclear reaction in intermediate-to-high-mass stars since low-mass stars cannot synthesize such heavy elements, thus leading to the idea, shared by all the proposed models, that 1G stars more massive than the ones that we currently observe in GCs eject processed material in the surroundings, polluting the intracluster medium (that at this early epochs was still permeating the GCs) in which the 2G stars would form. The detected lack of variation in elements typically ejected by supernovae (SNe), like iron, between 1G and 2G stars constitutes a further challenge in justifying the phenomenon. Indeed, a polluting mechanism that produces the 2G population must somewhat not involve the SNe ejecta.

Different models predict different polluters to produce the chemical anomalies. Particularly interesting are the implications that they would have on several research fields of astrophysics, impacting studies on SNe and AGB stars physics, as well as predicting that GCs were several times more massive at their birth and therefore that could strongly affect galaxy formation and the re-ionization of the Universe.

So far, no formation scenario is free of issues when compared to all the observational features of multiple populations (see Renzini et al., 2015; Bastian & Lardo, 2018, for critical reviews on the formation scenarios), and further complementary work on both the theoretical and observational sides is mandatory. In this Section, I summarize some of the most appealing models proposed throughout the years and some of their possible implications.

1.2.1 AGB Scenario

This formation scenario is the first ever conceived, dating back to nearly four decades ago (Cottrell & Da Costa, 1981), and it predicts, in its modern version (detailed in D'Ercole et al., 2008, 2010; D'Antona et al., 2016; D'Ercole et al., 2016), that the different populations observed in GCs originated in separate starbursts, with 1G stars forming before the 2G population(s). After the 1G formation, their stars more massive than 8 $\mathcal{M}_{\odot}$ explode as SNe, sweeping out all the remaining intracluster medium that did not collapse into stars yet, characterized by a chemical composition analogous to 1G stars (hereafter, the pristine gas).

At the end of the SNe explosions, stars with $\leq 8\ \mathcal{M}_{\odot}$ start to eject material processes by the CNO cycle via hot bottom burning when reaching the AGB evolutionary phase. These winds are slower than the ones from SNe and can be retained by the cluster potential well. This gas, made by pure AGB ejecta, flows towards the central areas, where it starts collapsing into stars, forming the 2G population(s). In this way, 2G stars can have He, C, N, O, Na, Mg, and Al abundances consistent with what is observed, without the contribution of SN ejecta. Since 2G stars form in the central areas, they would be initially more centrally concentrated than the 1G.

A very important role is played by the dilution mechanism. After the formation of 2G stars from pure AGB ejecta, if the pristine gas previously expelled can be reaccreted it would flow through the innermost regions, mixing with the AGB ejecta that did not

collapse in stars yet. This mixed material can give birth to subsequent generation(s) of stars, which have intermediate chemical composition between the 1G and the pure-ejecta 2G stars. Later, the explosion of the SN I stops the star formation, removing the intracluster gas still present within a GC.

To produce, starting from AGB ejecta, GCs with a predominance of 2G stars as we observe today, their initial mass must have been about ten times more than the present one. This implication is the so-called mass-budget problem, and to account for that, the authors proposed that the strong winds caused by these frequent SN explosions led to the dynamical heating of the cluster and, therefore, a rapid expansion. As a consequence, a large amount of stars move beyond the tidal radius and escape from the cluster. Since this phenomenon would involve only stars in the outskirts and 2G stars are initially formed in the inner areas only, 1G stars would preferentially be lost in this case, thus explaining why the majority of Galactic GCs are nowadays dominated by 2G stars.

1.2.2 Fast-Rotating Massive Stars

Massive stars, during their period in the MS, experience hot hydrogen burning in their cores, thus being able, in principle, to synthesize the material that produces the observed 2G stars abundances. In order to be ejected and pollute the intracluster medium, this material needs to reach the stellar surface. A way to do that was proposed by Decressin et al. (2007, but see also Krause et al. 2013), involving Fast-Rotating Massive Stars (FRMS), which are massive stars that rotate close to their breakup speed. These stars can contaminate the GC with material processed by hot hydrogen burning lost via equatorial winds.

In this scenario, 1G stars form before the 2G, similarly to the AGB model, and their population of FRMS starts polluting the cluster environment very early in its lifetime ($<$10-20 Myr), which then mixes with the pristine material for mixing 2G stars. As in the previous model, dilution is crucial to match the observed chemical patterns, such as the Na-O anticorrelation.

As in the AGB scenario, the mass budget problem is also present (even though a possible alleviation of this problem was proposed by Charbonnel et al. 2014).

1.2.3 Massive Interacting Binaries

In alternative to the FRMS, even binary interaction can bring the results of nucleosynthesis in the stellar core of massive MS stars up to the surface and eject them in the surroundings. Indeed, binary systems composed of massive stars can experience a severe mass loss that ejects CNO-processed material with low velocity, therefore being able to be retained within the GC. de Mink et al. (2009) exploit binary evolution codes to simulate the yields of a $20 + 15\ \mathcal{M}_{\odot}$ binary system with a 12-days orbital period. After burning all the hydrogen in its core, the primary star expands and transfers mass to its companion, which accretes this material until it reaches a critical rotation velocity. At

this point, no accretion is possible anymore and the transferred matter is ejected into the surroundings. This material comes from the core of the donor star and experienced CNO processing, thus showing common chemical characteristics with 2G stars, from which would form. During the mass transfer, the donor loses nearly all its envelope in the intracluster medium. The chemical composition of the emitted material can change if the parameters of the binary systems change (like the mass of the stars, their distance, period, etc.).

Under the assumption that the majority of massive stars were in binary systems in the first phases of a GC's life, this scenario would alleviate the mass-budget problem, providing more material to form 2G stars than the AGB stars and FRMS.

Since these systems would pollute the surroundings very early during the cluster's life, there is the possibility that at the time low-mass stars are still encircled by their circumstellar disks. Bastian et al. (2013) proposed that the circumstellar disk of pre-MS low-mass stars survives for $\sim$10 Myr and that they can sweep up the processed material when passing through the cluster's innermost areas. This material is eventually accreted by the host star, forming the 2G population. Along with the massive interacting binaries, also the FRMS could contribute to this model since they eject their material soon enough to be already present in the intracluster medium when low-mass stars still had their circumstellar disks. A peculiarity of this version is that it requires only a one-star formation episode.

1.2.4 Super Massive Stars

Denissenkov & Hartwick (2014) proposed the presence of Supermassive stars (SMSs) as the possible polluters that produced multiple populations. The SMSs would have a mass around 10^4 $\mathcal{M}_\odot$ and form in the GC center via runaway collisions of massive stars, which sink through dynamical friction. Their formation would be possible only in dense and compact environments, like the GCs.

During their MS evolution, hydrogen burning in their core produces the abundance patterns that characterize 2G stars. These fully convective stars would then lose a significant fraction of their mass by stellar winds, thus ejecting a large amount of polluted gas that can account for the high fraction of 2G stars observed among Galactic GCs, which would be spread in the innermost area of the cluster, forming an initially more centrally-concentrated 2G population. The remnant of the star, not ejected via winds, would eventually collapse to form an Intermediate-Mass Black Hole (IMBH).

Later, Gieles et al. (2018) hypothesized a different version of this scenario. Here, the proto-GC forms by monolithic collapse, accreting gas from the surroundings. Protostars that are populating the cluster at this epoch would accrete the material. This process causes a contraction of the proto-GC, triggering star collisions and forming the SMSs. Even after the formation of the SMSs, stellar collisions are still happening and will stop when the two-body relaxation of the cluster finally decreases the stellar density. These further stellar collisions would provide new fuel to the SMSs, which being fully convective

remain in the MS phase (where they are processing the material to produce the required elements anticorrelations) for longer, hence ejecting a large amount of polluted material (avoiding the mass-budget problem) that will mix with the pristine gas. Finally, low-mass protostars would accrete this gas to become the observed 2G stars. Similarly to the MIB scenario second version, in this case, only a single star formation episode is required.

1.2.5 Stellar Mergers

During the first Myr of a GC's life, the stellar density and the fraction of binaries were likely to be much higher than what we are observing today. Therefore, stellar mergers in binary systems or due to dynamical collisions were possibly common events in this environment. This phenomenon, among massive stars, could produce some of the polluters seen before, like the FRMS, the MIB, and the SMS, which may work together in giving birth to 2G stars.

This scenario was postulated by Wang et al. (2020) after performing N-body dynamical simulations of very young GCs to estimate the rate of stellar mergers and the amount of matter ejected by the polluters. In particular, they focused on the first 5 Myr of the cluster's life since after that epoch SNe start to explode, sweeping out the medium (which the cluster cannot retain due to the lack of iron differences among 1G and 2G stars).

They found that in this period, more than half of the massive stars ($> 30\ \mathcal{M}_{\odot}$) can merge and form FRMSs, MIBs, and SMSs. By assuming a Kroupa IMF (Kroupa, 2001), about 3.75% of the total cluster mass would be ejected as polluted material, which will then mix with the pristine gas that is still permeating the cluster, producing the significant observed fraction of 2G stars.

A unique characteristic of this idea is that it combines all the previous multiple formation scenarios. Indeed, beyond the FRMS, the MIB, and the SMS scenarios, the authors also proposed that, after the SNe explosions, further 2G stars could be formed by AGB winds, even though they would make up a small contribution to the total population.

1.2.6 Multiple Stellar Populations as a Case of Cooling

The last scenario presented in this Section was recently proposed by Renzini (2023) and sets the following three assumptions: (i) all GCs formed within dwarf galaxies, (ii) 2G stars form from material ejected by massive binaries, and (iii) stars more massive than a certain threshold do not explode as SNe, but they rather silently sink as black holes.

Dwarf galaxies would be the GCs' progenitors, such that not only the 1G massive binaries inside the GC produce the necessary processed gas, but also the stars in the dwarf galaxy would contribute. The deep potential well of the GC can accrete the part of the processed material produced by dwarf's binaries, which causes a cooling flow of this material towards the innermost areas of the cluster. Being dwarfs thousands of times more massive than GCs, this idea would not be affected by the mass-budget problem.

The cooling flow of matter may not be continuous but produce several bursts of star formation, justifying the discrete 2G populations observed in clusters like NGC 2808. The cooling flow of material ejected by GC's massive binaries could produce the first 2G stars, which would be highly mixed with pristine gas, thus obtaining the less-extreme 2G population. Then, different bursts from newly accreted material may happen when it reaches the cluster's center.

To avoid overlapping between the ejecta from massive binaries and from SNe, an upper mass limit over which no explosion happens is necessary. Renzini proposed that a delay in SNe explosion of ∼5-10 Myr, therefore an upper limit of about 20-40 $\mathcal{M}_{\odot}$, could give 2G stars the time to form before SNe explosions stop the star formation. The dwarf galaxies are then disrupted via tidal interaction with the Milky Way, leaving just the GCs as remnants.

This scenario, which assumes multiple generations of stars, is consistent with the observational evidence that in more massive GCs, there is a higher fraction of 2G stars since a more massive cluster would have a deeper potential well and, therefore, could accrete more processed material from the host dwarf galaxy.

Metal-rich bulge GCs, due to their high metallicity, cannot be formed in dwarf galaxies, but rather when the Milky Way was already a few 10^{10} massive. This implies that in the Milky Way bulge, similar conditions than in the dwarf galaxies were present, but these were rarer since there are about ten times fewer GCs in the bulge area than in the Galactic halo.

1.3 The Type II Globular Clusters

The clusters described so far, characterized by separate populations with different light-elements abundances, are the so-called Type I GCs. On top of that, another class of these objects, the Type II, has been observed. These GCs display, beyond the typical 1G-2G patterns, an additional group of stars, forming a further population visible from photometry and spectroscopy. Their presence introduces a second fainter SGB and a second redder RGB than the bulk of stars typically observed in all GCs (Milone et al., 2008; Han et al., 2009; Piotto et al., 2012; Milone et al., 2017a; Jang et al., 2022).

Spectroscopic analysis revealed that these stars exhibit differences in their abundances of elements heavier than the ones varying between 1G and 2G stars, being enhanced in s-process elements (such as barium, lanthanum, and strontium), and also in [Fe/H], being on average iron-richer. Another intriguing feature found by spectroscopy is the presence of a difference in the total C+N+O, with the Type II stars enhanced in this quantity (e.g., Carretta et al., 2010; Marino et al., 2011c, 2015; Yong et al., 2015; Tautvaišienė et al., 2022).

From now on, I will refer to as 'canonical' the stars that form the 1G-2G patterns typical of old, massive GCs, while as 'anomalous' the additional population that defines Type II GCs.

The higher panels of Figure 1.5 display the $m_{\rm F814W}$ vs. $m_{\rm F336W} - m_{\rm F814W}$ CMD

zoomed on the SGB and RGB (left and middle, respectively), and the ChM of RGB stars for the Type I GCs NGC 5904 (right panel). Here, the SGB and RGB form a single well-defined sequence, while the ChM exhibits the same 1G+2G populations also visible in the previous Figures. On the other hand, the lower panels portray the same diagrams but for the Type II NGC 1851. Here, the anomalous stars are colored in red and describe a further distinct sequence in the CMDs, which leads to the additional cloud of red stars in the ChM.

As in typical multiple-population fashion, Type II GCs, which constitute about one-fifth of the studied Galactic GCs, display a high variability. Indeed, while split SGB and RGB and chemical inhomogeneities are common features, the incidence of anomalous stars, as well as their distribution on the ChM, significantly changes from one cluster to the other. Their fraction span from constituting a minor contribution (smaller than 10% in NGC 362, NGC 1261, NGC 6934, and NGC 7089) to populating around 40-60% of the total amount of stars, like in NGC 5139, NGC 6656, and NGC 6715 (Milone et al., 2017a). Moreover, there is variety between how the chemical peculiarities manifest among Type II GCs: NGC 1261 and NGC 6934 do not show differences in s-process elements, while their anomalous stars are iron richer by about 0.1 and 0.2 dex, respectively (Marino et al., 2021). On the other hand, NGC 1851 exhibits differences in s-process elements, but the variations in [Fe/H] are small-to-nil, whereas the presence of a total C+N+O spread is still debated (e.g., Carretta et al., 2010; Yong et al., 2015; Tautvaišienė et al., 2022). Other clusters, like NGC 6656 and ωCen display all the three chemical features (Johnson & Pilachowski, 2010; Marino et al., 2011b,c,a, 2012).

Another intriguing characteristic of anomalous stars is that they are often not consistent with being chemically homogeneous but they exhibit star-to-star light-elements variations in some way similar to the ones between 1G and 2G stars, with sodium-oxygen anticorrelation detected among anomalous stars of, among the others, NGC 1851, ωCen, NGC 5286, and NGC 6656 (e.g., Carretta et al., 2010; Marino et al., 2011c,a, 2015).

The origin of this class of clusters is another mystery on top of the mystery of the multiple population phenomenon. Type II GCs are suspected to be remnants of larger structures, likely dwarf galaxies, that were accreted by the Milky Way to then lose their outer layers, leaving only their surviving naked nuclei. This hypothesis is supported by the discovery that the Type II GC NGC 6715 lies at the very center of the Sagittarius dwarf galaxy and by the observation of a halo extended up to several times the tidal radius of another Type II GC, NGC 1851, which in this context would be the remnant of a more extended stellar system (Brown et al., 1999; Bellazzini et al., 2008; Olszewski et al., 2009; Sollima et al., 2012; Marino et al., 2014a). These two clusters would be examples of originally larger structures, thus playing a pivotal role in shaping the Milky Way. Furthermore, the study of the behavior of Type II GCs in the Integral of Motion (IOM) space corroborates this idea since 7 (and possibly even 8) of them are clustered in a distinct region of this space to the other GCs, thus strongly suggesting that they are associated with a single accretion event (see the discussion in Milone & Marino, 2022, and reference therein). The fact that no Type II GCs have been discovered in

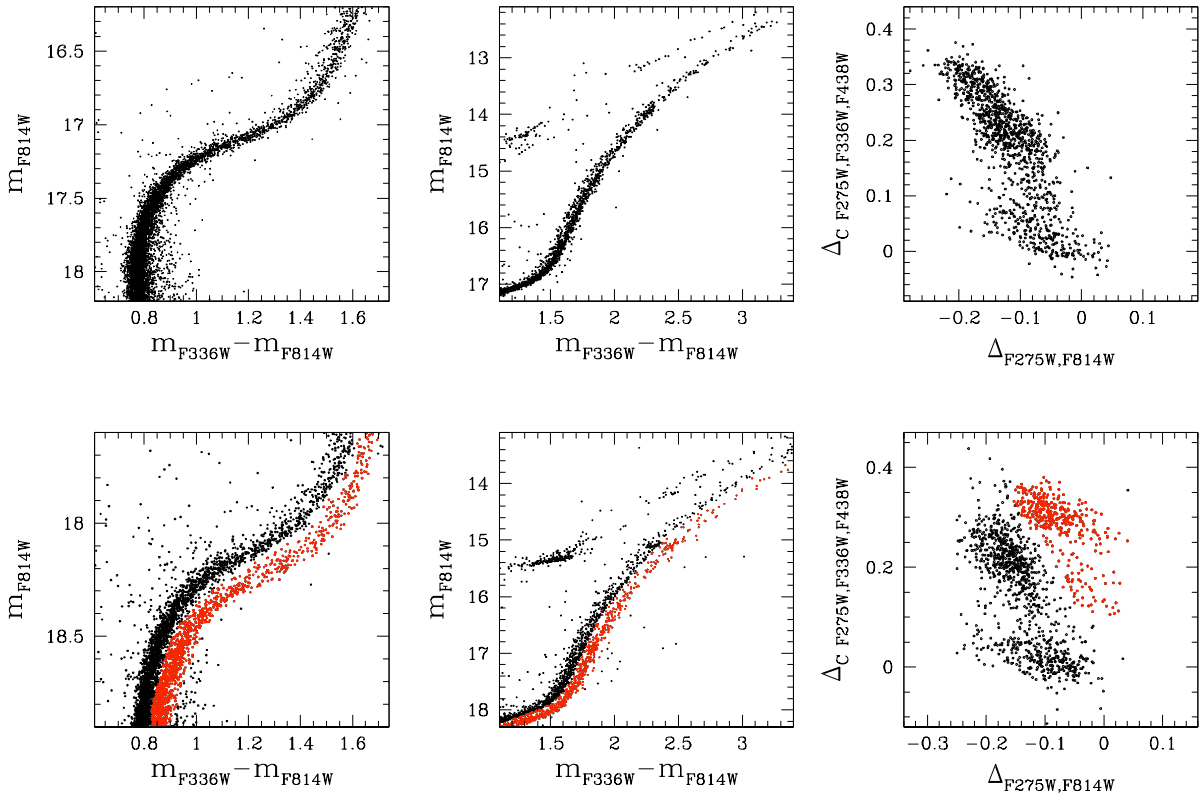

Figure 1.5: *Upper panels*: $m_{\rm F814W}$ vs. $m_{\rm F336W} - m_{\rm F814W}$ CMD zoomed on the SGB (left) and RGB (middle), and ChM of RGB stars (right) of NGC 6723. *Lower panels*: same but for NGC 1851. The anomalous stars are colored in red.

the MCs could be another clue in favor of the accretion scenario because these galaxies have masses order of magnitudes smaller than the Milky Way, hence being less efficient in accreting dwarf galaxies. On the other hand, in M31, which is even more massive than the Milky Way, a strong Type II candidate has been discovered by Nardiello et al. (2019), while other possible candidates characterized by a spread in [Fe/H] have also been detected (Fuentes-Carrera et al., 2008).

The origin of these stars, within dwarf galaxies or not, is currently unknown. Two main scenarios have been proposed to explain their existence:

- Merging scenario. Here, Type II would result from a merging between (at least) two GCs formed within the same dwarf galaxy which, after developing their light-elements anticorrelations, spiral in its nuclear region. Then, the host galaxy's outer population is stripped during the accretion by the Milky Way, leaving just its naked nucleus, which would be a Type II GC. If GCs are not massive enough, they are more likely to be tidally stripped from their host dwarf galaxies before merging, and they will remain Type I. Therefore, the fate of a GC is dependent on its initial mass.

  In this picture, the distinct GCs formed at different epochs during the life of the dwarf galaxy, hence when its chemical composition, due to its evolution, was differ-

ent. The chemical evolution of the host galaxy would be the driver of the observed s-process and [Fe/H] variations, and the amount of their difference would depend on the 'time lag' (i.e., the difference between the formation epochs of the different GCs) and the rapidity of the star formation in the host dwarf. Shorter time lags and slower star formation would lead to smaller Δ[Fe/H] and Δ[s-process/H]. This scenario requires that the chemical enrichment of the dwarf happens shorter than the merging timescale. Here, more massive dwarf galaxies, surviving for a longer time before disruption, have a longer chemical evolution and can, in principle, produce larger spread in s-process elements and iron and give birth to several massive GCs, which would then merge give birth to such complex structures like ωCen. The dwarf galaxy chemical evolution alone fails to explain simply the observed C+N+O differences between canonical and anomalous stars in GCs like M22 since it would require excessively long timescales to produce it. A way to obtain such C+N+O variations is to assume that the stars in the anomalous GC form from material ejected from AGB stars and SNe which did not mix well with the already-present interstellar medium in the dwarf galaxy.

This scenario, proposed by Bekki & Tsujimoto (2016, but see also Carretta et al. 2010; Bekki & Yong 2012), is based on results obtained through purely collisionless simulations aimed at reproducing the chemical patterns observed in Type II GCs, analyzing both the dynamical and the chemical evolution of dwarf galaxies.

- Self-enrichment scenario. This hypothesis, proposed by D'Antona et al. (2016) and D'Ercole et al. (2016), is an extension of the AGB scenario. It predicts a prolonged star formation in Type II GCs, where anomalous stars are produced by different polluters than the 2G population. To explain the iron enhancement, they assume that the cluster was able to retain a fraction of the SN ejecta, which could be possible in dwarf galaxies (especially if dark matter was present at the time) or in particularly massive GCs. Since the 1G-2G pattern does not show [Fe/H] differences, D'Antona and collaborators suggested that the explosions of delayed SN II in binary systems after the formation of 2G stars may be the source of the iron spread, destroying the cooling flow and stopping the formation of 2G stars. However, their frequency is not as high as in the initial SN II epoch, and consequentially the winds are not strong enough to definitively push the intra-cluster medium (formed by pristine material and AGB ejecta) out of the cluster proximity. Several Myr later, the delayed SN II events become rare, giving the possibility to the GCs to re-accrete the material, which would be contaminated by the SN II ejecta.

  In this period, stars with $\sim$3.5-4 $\mathcal{M}_{\odot}$ evolved into the AGB phase and started to pollute the medium with their ejecta, which is different than the one from more massive AGB winds that produced, according to this scenario, the 2G stars, being strongly affected by third dredge-up and injects in the intra-cluster medium material enhanced in total CNO and s-process elements. From this material, the anomalous

population(s) form, and will be enriched in total CNO, s-process elements, and/or [Fe/H] depending on the influence of the different polluters within a given GC (like the number of delayed SN II events). If the mixing between different ejecta is inhomogeneous, it is possible to develop a Na-O anticorrelation among anomalous stars (D'Ercole et al., 2016, see their Section 4.2), thus producing the observed light-elements inhomogeneities. The star formation finally ends when the frequency of SN Ia becomes high enough to push away all the intra-cluster medium (after about 10^8 yr).

Explaining the existence of Type II GCs constitutes one of the most challenging tasks of stellar astrophysics, and drawing a complete picture that includes these objects in the multiple populations phenomenon is a major issue in the GCs field of research. In particular, the study of anomalous stars lags far behind when compared to the study of canonical 1G and 2G stars, especially concerning photometry, with crucial pieces of information still missing, such as their spacial distribution, an extensive tagging of their subpopulations and a general framework that can be comparable with the results from spectroscopy.

1.4 Aims and Layout of the Thesis

This thesis focuses on exploring the multiple populations phenomenon in GCs by using as a principal tool of investigation resolved stellar photometry, combined with results from spectroscopy, kinematics, and theoretical models. Several aspects of this mysterious phenomenon, which were previously lacking in an extensive study, will be faced in the following Chapters. These results are going to give new insights into the multiple populations and provide novel observational constraints to formation theories.

The final goal of the thesis is to solidify our knowledge on many key aspects of the multiple populations and, at the same time, lay the foundation for the exploration of the most recent, raising hot topics that are going to polarize this field of research in the future years, as a part to the long-term challenge to build a comprehensive and self-consistent picture of GC formation and evolution. The work is structured as follows:

- Chapter 2. Here, I present a study on the multiple populations along the HB, published by Dondoglio et al. (2021). This work represents the first homogeneous analysis of the phenomenon over a large sample of GCs for stars in this evolutionary phase. This work gives insights into, among others, the incidence of multiple populations, the relation of the phenomenon with the host galaxy, and the presence of chemical inhomogeneity among 1G stars.
- Chapter 3. This Chapter focuses on the least massive stars in which we can detect multiple populations, i.e., the ones at the bottom of the MS. Here, I show that most of the characteristics of the phenomenon are still valid among these stars, thus confirming its primordial origin. Moreover, this study, whose results are published in Dondoglio et al. (2022), provides the first measurement of the Mass Function (MF)

of chemically different populations over the whole MS, covering an unprecedented wide stellar mass range, giving new constraints for the formation scenarios.

- Chapter 4. This Chapter investigates the mystery of Type II GCs, using one of them -NGC 1851- as a template to provide the first photometric in-depth exploration of the anomalous stars and, in particular, their subpopulations, comparing some of their fundamental characteristics, such as their fraction, chemical composition, and radial and spacial distributions, to the canonical stars that we observe in typical Type I GCs. These results have recently been accepted for publication and are also present in Dondoglio et al. (2023).
- Chapter 5. This Chapter summarizes the thesis and some final remarks and considerations on all the results displayed and their impact on this field of research, as well as addressing future studies these results will heavily influence.

CHAPTER 2

Multiple Populations among red Horizontal Branch and Red Clump stars

Abstract

In the following Chapter, I present the study published in Dondoglio et al. (2021) focused on the multiple populations phenomenon among red HB and red clump stars. In this work, we exploit multi-band *HST* photometry to investigate multiple populations along the red HB and red clump of 14 metal-rich GCs, including twelve located in the Milky Way and the Magellanic Clouds GCs NGC 1978 and NGC 416.

Based on appropriate two-color diagrams we find that the fraction of 1G stars in Galactic GCs correlates with cluster mass, confirming previous results based on RGB hptometry. Magellanic-Cloud GCs exhibit higher fractions of 1G stars than the Galactic ones with similar masses, thus suggesting that the environment affects the multiple populations phenomenon. We compare and combine our population fractions based on HB with previous estimates from MS and RGB, and we used ground-based UBVI photometry (available for NGC 104, NGC 5927, NGC 6366, NGC 6838) to extend the investigation over a wide Field of View. All studied GCs are consistent with flat distributions of 1G and 2G stars within $\sim$1 arcmin from the cluster center except NGC 416, where the 2G is more centrally concentrated. For the clusters with available ground-based photometry, we detect that 2G stars of NGC 104 and NGC 5927 are more centrally-concentrated than the 1G, whereas no difference is detected in NGC 6366 and NGC 6838.

We discover that most of the analyzed GCs exhibit extended sequences of 1G stars along the red HB, not consistent with a simple population. The comparison between

appropriate synthetic and observed CMDs reveals that these extended distributions are consistent with either star-to-star variation in helium or with an internal metallicity spread.

2.1 Introduction

The study of multiple populations in GCs with photometry has mainly focused on RGB stars. This evolutionary phase represents the most fertile ground for investigating this phenomenon since it is composed of a relatively high number of cluster stars, therefore ensuring good statistics, which have a high signal-to-noise ratio, i.e., they have low observational errors. RGB stars photometry served in studies that were instrumental in shaping our current knowledge of the multiple populations phenomenon (e.g., Carretta et al., 2009b; Milone et al., 2017a; Marino et al., 2019a) among Galactic and extragalactic GCs, allowing the investigation of its relationship with the host galaxy. MS stars have also represented an intriguing target for exploring the phenomenon since they compose the most populated evolutionary phase of a GC. However, their relatively low signal-to-noise ratio limits their study with the available archive data to a subsample of all the known clusters that host multiple stellar populations.

In this Chapter, we extend the study of the multiple-populations phenomenon to the red HB and red clump phases, populated by bright and easily identifiable stars. Early signs of chemical differences among red HB stars come from Norris & Freeman (1982), who analyzed 14 stars of 47 Tuc with both photometry and spectroscopy, finding a bimodality in the CN molecule distribution and carbon-nitrogen anticorrelation. Later, Smith & Penny (1989) detected similar chemical anomalies in NGC 6838. Recent high-resolution spectroscopy studies have revealed that in intermediate metallicity GCs (from about [Fe/H]~ -1.0 to -1.4), Na-poor and O-rich stars (thus belonging to the 2G) populate the reddest part of the HB while Na-rich and O-poor stars mostly lie on the blue HB (Marino et al., 2011b, 2014a). In others, the red HB can host multiple populations with different light-element abundances that are merely mixed in the photometric diagrams (e.g., Gratton et al., 2011; Marino et al., 2014a). On the contrary, appropriate photometric diagrams can detect separated sequences of 1G and 2G stars along the red HB of metal-rich GCs with [Fe/H]> -1.0. Milone et al. (2012b) have shown that in 47 Tuc the two-color diagram $m_{\rm F275W} - m_{\rm F336W}$ vs. $m_{\rm F336W} - m_{\rm F435W}$ is an efficient tool in separating 1G and 2G stars among red HB stars. They compared observations with synthetic spectra, finding that 1G red HB stars have redder F275W-F336W colors than 2G red HB stars with the same F336W-F435W colors.

Photometric diagrams obtained from the appropriate combination of U, B, I magnitudes (e.g., Marino et al., 2008; Sbordone et al., 2011) or from the so-called JWL indices (Lee, 2017; Lee, 2018; Lee, 2019) are exquisite tools to identify multiple populations among giant stars by using ground-based telescopes and have allowed split red HBs in some GCs, including 47 Tuc and NGC 6838 (e.g., Milone et al., 2012b; Monelli

et al., 2013; Lee & Sneden, 2020; Cordoni et al., 2020), to be detected.

In this Chapter, we exploit multi-band *HST* observations to explore the multiple populations in this evolutionary stage, applying for the first time a homogeneous approach over an extended sample metal-rich Galactic GCs, namely 47 Tuc, NGC 5927, NGC 6304, NGC 6352, NGC 6366, NGC 6388, NGC 6441, NGC 6496, NGC 6624, NGC 6637, NGC 6652, and NGC 6838. Furthermore, we include the LMC GC NGC 1978, and the GC NGC 416 in the SMC, hunting for multiple populations in red HB and red clump for the first time in extragalactic GCs.

2.2 Dataset and Data Reduction

To carry on this work, we use the photometric catalogs by Anderson et al. (2008), Milone et al. (2012b), Milone et al. (2017a), and Milone et al. (2018b), which provide astrometry and differential-reddening corrected multiband photometry for the Galactic GCs in the F275W, F336W, and F438W filters of the Ultraviolet and Visual Channel of the Wide Field Camera 3 (UVIS/WFC3) and the F606W and F814W bands of the Wide Field Channel of the Advanced Camera for Survey (ACS/WFC) on board *HST*.

To investigate the red HB and the red clump of NGC 416 and NGC 1978, we derive stellar positions and magnitudes by performing Point Spread Function (PSF) photometry on the archive images summarized in Table 2.1. To do that, we use the computer program KS2, which was developed by Jay Anderson and is an evolution of the program kitchen_sync (Anderson et al., 2008). KS2 adopts distinct methods to measure stars. Method I provides the optimal photometry and astrometry for bright stars, fitting each one by using the PSF model corresponding to its location and derives stellar fluxes and positions independently. Then, it averages these values together to compute the best estimates of magnitudes and coordinates. Methods II and III combine information from all images and provide robust measurements for faint stars. After subtracting neighboring stars, by using the most accurate estimates of stellar positions and fluxes, these methods perform aperture photometry over a region of either 5×5 pixels (method II) or 0.75×0.75 pixels (method III). The aperture center corresponds to the best determination of the stellar position. Method III works better in crowded environments (see Sabbi et al., 2016; Bellini et al., 2017; Nardiello et al., 2018, for detailed discussions).

To pursue our scientific goals, we select well-measured stars, i.e., that are well-fitted by our PSF model, by exploiting the various diagnostics of photometric and astrometric quality provided by the KS2. Specifically, we adopt the root mean scatter of the photometric measurements, the $Q_{\rm Fit}$ parameter, which indicates how much a star is well fitted by a PSF model, (e.g. Anderson et al., 2008; Nardiello et al., 2018) and the $RADXS$ parameter (Bedin et al., 2008), a shape parameter that quantifies the amount of flux exceeding the predicted flux of the PSF model, which can disentangle stellar sources from sources with broader (e.g., galaxies) or narrower (e.g., cosmic rays and artifacts) profiles. We emphasize that we derive these parameters from comparing the observed sources with the PSF model, and we repeat those calculations for all methods sepa-

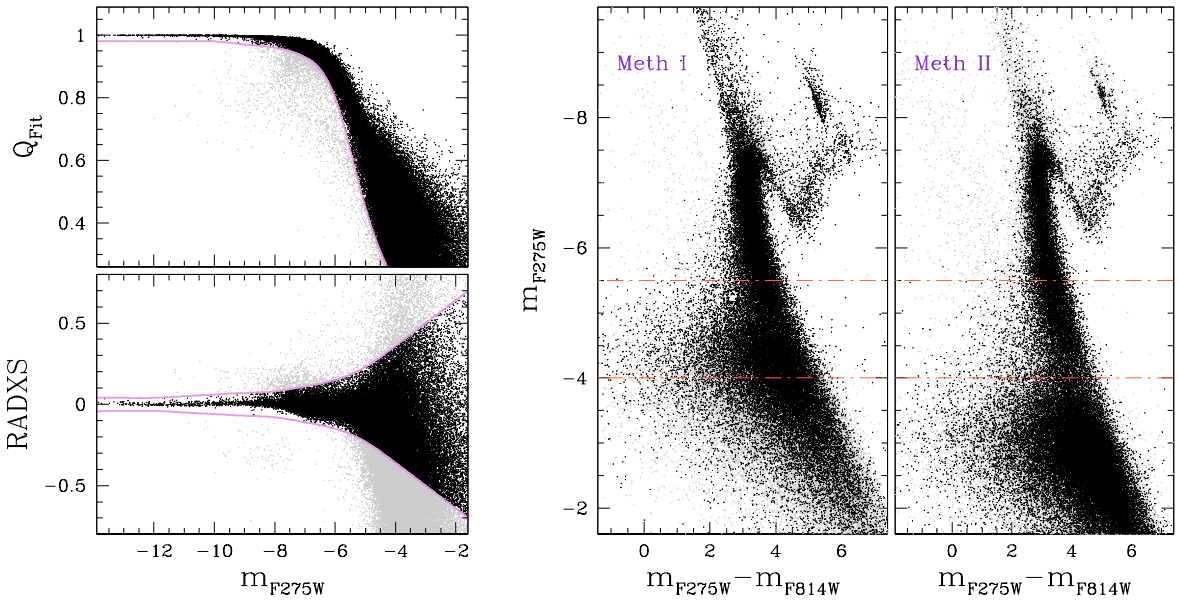

Figure 2.1: *Left panels:* $Q_{\rm Fit}$ (upper) and $RADXS$ (lower) parameters obtained by performing method I photometry against the instrumental $m_{\rm F275W}$ magnitude of NGC 416. Pink lines separate the region populated by the well-measured stars from the sources excluded from our catalog, colored in black and grey, respectively. *Central panel:* instrumental $m_{\rm F275W}$ vs. $m_{\rm F275W} - m_{\rm F814W}$ CMD obtained from the KS2 method I. The orange horizontal lines delimit the magnitude interval in which the differences between photometry from method I and II are more evident. *Left panel:* same as the central panel but for method I.

rately. In method I, we use the stellar fluxes derived from PSF fitting, while in methods II and III, where stellar fluxes are measured utilizing aperture photometry, we adopted for the PSF model the magnitudes inferred with these methods. We refer to the paper by Nardiello et al. (2018, see their Section 2 and references therein) for details. We illustrate an example of the procedure in Figure 2.1, where we show in the left panels the $Q_{\rm Fit}$ and the $RADXS$ parameters derived from F275W photometry obtained through the method I. Pink lines separate the regions populated by well-measured stars (black points) from the excluded sources. Central and left panels represent the instrumental $m_{\rm F275W}$ vs. $m_{\rm F275W}-m_{\rm F814W}$ CMDs obtained with method I and II, respectively. Method II provides better photometry at fainter magnitudes, especially in the -5.5 $< m_{\rm F275W} <$ -4 range, highlighted by the two orange lines.

We then calibrate the magnitudes into the Vega system as in Bedin et al. (2005), by using the zero points available in the Space Telescope Science Institute webpage[2] for UVIS/WFC3 and WFC/ACS. Stellar positions are corrected for geometric distortion by using the solutions provided by Bellini & Bedin (2009); Bellini et al. (2011).

[2] http://www.stsci.edu/hst/instrumentation/wfc3/calibration and http://www.stsci.edu/hst/acs/analysis/zeropoints for WFC3/UVIS and ACS/WFC photometry, respectively.

Table 2.1: Summary of the data of NGC 416 and NGC 1978 used in this work.

DATE	N× EXPTIME	FILTER	INSTRUMENT	PROGRAM	PI
		NGC 416			
2019 Jun 18	1500s+1512s+2×1529s+2×1525s	F275W	UVIS/WFC3	15630	N. Bastian
2019 Jul 31	1530s+1500s+2×1533s+2×1534s	F275W	UVIS/WFC3	15630	N. Bastian
2019 Aug 05	2×1500s+1512s+2×1515s+1523s	F275W	UVIS/WFC3	15630	N. Bastian
2016 Jun 16	700s+1160s+1200s	F336W	UVIS/WFC3	14069	N. Bastian
2016 Jun 16	500s+800s+1650s+1655s	F343N	UVIS/WFC3	14069	N. Bastian
2016 Jun 16	75s+150s+440s+460s	F438W	UVIS/WFC3	14069	N. Bastian
2005 Nov 22	2×20s	F555W	ACS/WFC	10396	J. Gallagher
2006 Mar 08	2×20s+4×496s	F555W	ACS/WFC	10396	J. Gallagher
2005 Nov 22	2×10s+4×474s	F814W	ACS/WFC	10396	J. Gallagher
2006 Mar 08	2×10s+4×474s	F814W	ACS/WFC	10396	J. Gallagher
		NGC 1978			
2019 Sep 17	2×1493s+2×1498s+2×1500s+2×1499s 1501s+1502s+1495s+1492s	F275W	UVIS/WFC3	15630	N. Bastian
2011 Aug 15	380s+460s	F336W	UVIS/WFC3	12257	L. Girardi
2016 Sep 25	660s+740s	F336W	UVIS/WFC3	14069	N. Bastian
2016 Sep 25	425s+450s+500s+2×800s+1000s	F343N	UVIS/WFC3	14069	N. Bastian
2016 Sep 25	75s+120s+420s+460s+650s+750s	F438W	UVIS/WFC3	14069	N. Bastian
2003 Oct 07	300s	F555W	ACS/WFC	9891	G. Gilmore
2011 Aug 15	60s+300s+680s	F555W	ACS/WFC	12257	L. Girardi
2003 Oct 07	200s	F814W	ACS/WFC	9891	G. Gilmore

In addition to *H*ST data, we also exploit ground-based astrometric and photometric catalogs published by Stetson et al. (2019, see also Stetson 2005 for details on the photometry), which are available for four of the GCs in our sample, namely 47 Tuc, NGC 5927, NGC 6366, and NGC 6838. This catalog includes stellar magnitudes in the U, B, V, R, and I bands and reaches distances from the cluster's center up to ∼20 arcmin. It was built by performing PSF photometry on images from multiple ground-based facilities taken at different epochs. To this catalog, we apply a cleaning procedure to isolate the cluster's stars through the diagnostics defined by Stetson and collaborators (see their Section 4.1).

To investigate multiple populations with these catalogs, we combine the photometry by Stetson and collaborators with stellar proper motions from Gaia Data Release 2 (DR2; Gaia Collaboration et al. 2018). First, we select a sample of stars with accurate mea-

surements in the Gaia catalog by following the recipe of Cordoni et al. (2018, 2020). In a nutshell, we first identify stars with accurate proper motion measurements, by using both the `astrometric_gof_al` (`As_gof_al`) and the `Renormalized Unit Weight Error` (`RUWE`) parameters (Lindegren et al., 2018). We then select cluster members from the proper motion vector-point diagram (see Cordoni et al., 2018, for details).

Both the *H*ST and ground-based photometry have been corrected for differential reddening and zero-point variations effects using the recipe and the software presented by Milone et al. (2012c, see their Section 3.1 and 3.2).

To provide an example of the photometry derived after our data reduction, we present in Figure 2.2 the $m_{\rm F275W}$ vs. $m_{\rm F275W} - m_{\rm F814W}$ CMDs of NGC 416 and NGC 1978 (bottom panels). These two Magellanic Clouds' GCs show the presence of multiple populations, as proved by the ChMs of their RGB stars portrayed in the upper panels, where we illustrate the $\Delta_{\rm CF275W,F343N,F438W}$ vs. $\Delta_{\rm F275W,F814W}$ and the $\Delta_{\rm CF275W,F336W,F438W}$ vs. $\Delta_{\rm F275W,F814W}$ ChMs. The fact that the distribution of stars is wider than what is expected by observational errors only (orange points) corroborates previous evidences that these two GCs host multiple stellar populations (Niederhofer et al., 2017; Martocchia et al., 2018b,a; Lagioia et al., 2019b; Milone et al., 2020a).

2.3 Identifying multiple populations among red HB stars of Galactic GCs

To separate 1G and 2G stars in our sample of Galactic metal-rich GCs, we exploit the $m_{\rm F275W} - m_{\rm F336W}$ vs. $m_{\rm F336W} - m_{\rm F438W}$ two-color diagram, which is, as discussed in Section 2.1, an efficient tool to identify stars with different light-elements abundances in the red HB, as well as among MS, SGB, and RGB stars. The reason lies in the sensitivity of the F275W, F336W, and F438W *H*ST bandpasses to the strengths of the OH, NH, and CN molecules, whose absorption bands fall in their wavelength ranges. As a consequence, 2G red HB stars, which are enriched in nitrogen and depleted in carbon and oxygen with respect to the 1G stars, are dimmer in the F336W filter and brighter in the F275W and F438W filters (Milone et al., 2012b; Milone et al., 2013). The red-HB split is more evident in metal-rich GCs with [Fe/H] > -1.0. Indeed, similarly to RGB, SGB, and MS stars, the fluxes of their relatively cold red-HB stars are strongly affected by the abundances of carbon, nitrogen, and oxygen.

Table 2.2 lists relevant quantities for all studied clusters. These include the average reddening in the analyzed Field of View (FoV), E(B-V), the random mean scatter of reddening, the core radius ($r_{\rm c}$), the half-light radius ($r_{\rm hl}$), and concentration (c). We also indicate the maximum radius covered by *H*ST and, when available, ground-based observations, $r_{\rm FoV}$.

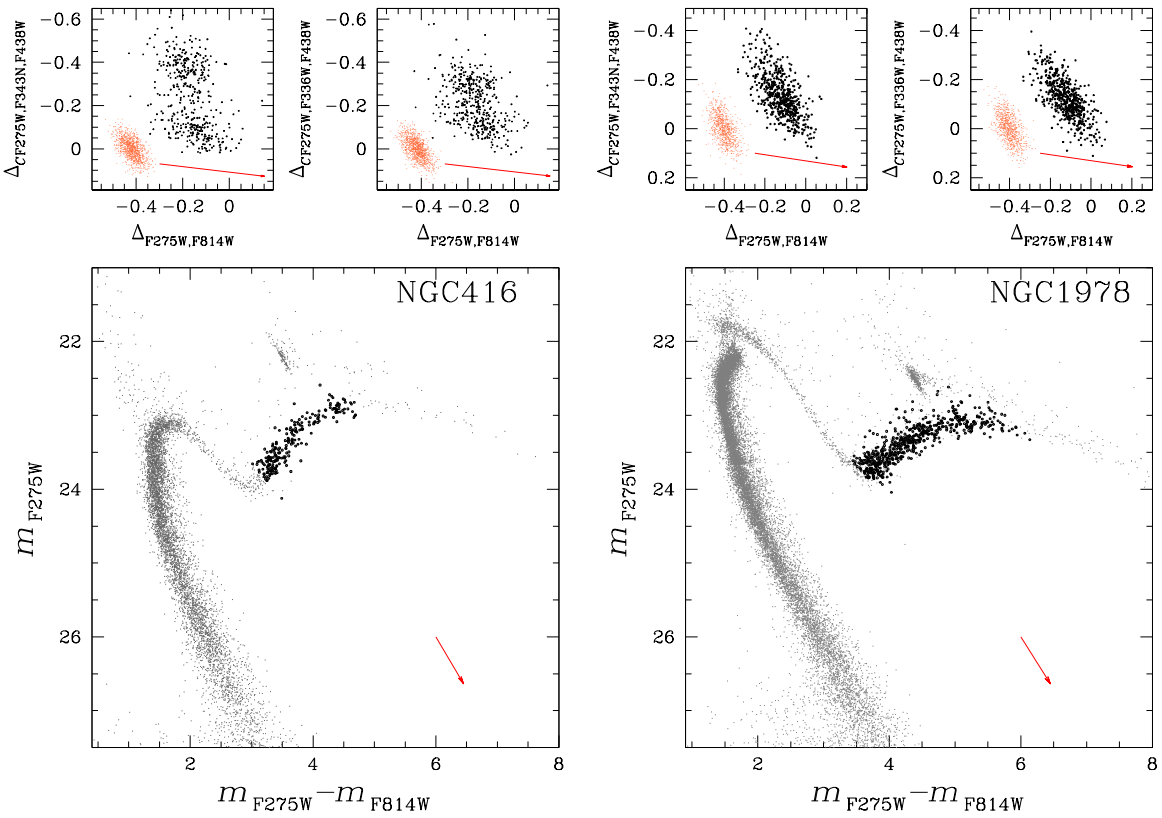

Figure 2.2: *Bottom panels.* $m_{\rm F275W}$ vs. $m_{\rm F275W} - m_{\rm F814W}$ CMD of stars in NGC 416 (left) and NGC 1978 (right). *Upper panels.* $\Delta_{\rm CF275W,F343N,F438W}$ vs. $\Delta_{\rm F275W,F814W}$ and $\Delta_{\rm CF275W,F336W,F438W}$ vs. $\Delta_{\rm F275W,F814W}$ ChMs of RGB stars marked with black dots in the bottom panels. Orange points mark the distribution of observational errors, including errors on differential reddening. Red arrows indicate the reddening vectors and correspond to a reddening variation $\Delta E(B-V) = 0.1$.

2.3.1 Disentangling First- and Second-generation Stars along the HB of Galactic GCs

All the considered Galactic GCs have [Fe/H] $\gtrsim -0.8$ dex and exhibit the red HB alone, with the remarkable exceptions of NGC 6388 and NGC 6441, which also show a blue HB (e.g., Rich et al., 1997).

To illustrate our procedure to identify 1G and 2G stars, we use NGC 6637, which exhibits the red HB alone, and NGC 6388, whose HB is populated on both sides of the RR-Lyrae instability strip, as template cases. We first exploit the differential-reddening-corrected $m_{\rm F438W}$ vs. $m_{\rm F438W} - m_{\rm F814W}$ CMDs displayed in Figure 2.3 to select by eye the HB stars. Black dots highlight red HB members and, for NGC 6388, blue crosses indicate the blue HB stars.

Table 2.2: This table lists the average reddening $E(B-V)$ of each cluster and the random mean scatter of reddening in the field of view, the core radius, the half light radius, the concentration and maximum radial distance of our HST observations. We also list the maximum radius of the FoV of ground-based photometry of 47 Tuc, NGC 5927, NGC 6366 and NGC 6838.

CLUSTER	$E(B-V)$ [mag]	r.m.s. [mag]	$r_{\rm c}$ [arcmin]	$r_{\rm hl}$ [arcmin]	c	$r_{\rm FoV}$ [arcmin]
NGC 0104	0.04[a]	0.004[f]	0.36[a]	3.17[a]	2.07[a]	1.66-24.57
NGC 5927	0.45[a]	0.017[f]	0.42[a]	1.10[a]	1.60[a]	0.95-5.96
NGC 6304	0.54[a]	0.012[f]	0.21[a]	1.42[a]	1.80[a]	0.93
NGC 6352	0.22[a]	0.017[f]	0.83[a]	2.05[a]	1.10[a]	0.91
NGC 6366	0.71[a]	0.019[f]	2.17[a]	2.92[a]	0.74[a]	0.90-7.99
NGC 6388	0.37[a]	0.012[f]	0.12[a]	0.52[a]	1.75[a]	1.00
NGC 6441	0.47[a]	0.020[f]	0.13[a]	0.57[a]	1.75[a]	0.92
NGC 6496	0.15[a]	0.014[f]	0.95[a]	1.02[a]	0.70[a]	0.89
NGC 6624	0.28[a]	0.008[f]	0.06[a]	0.82[a]	2.50[a]	0.89
NGC 6637	0.18[a]	0.007[f]	0.33[a]	0.84[a]	1.38[a]	0.94
NGC 6652	0.09[a]	0.005[f]	0.10[a]	0.48[a]	1.80[a]	0.91
NGC 6838	0.25[a]	0.012[f]	0.63[a]	1.67[a]	1.15[a]	0.97-8.94
NGC 1978	0.08[b]	0.003[g]	0.30[c]	0.67[c]	1.26[e]	0.55
NGC 0416	0.05[b]	0.020[g]	0.17[d]	0.25[d]	1.02[h]	0.55

References: [a]Harris (1996, 2010 edition); [b]Chantereau et al. (2019); [c]McLaughlin & van der Marel (2005); [d]Fischer et al. (1992); [e]Mateo (1987); [f]Milone et al. (2012a, 2017a); [g]Milone et al. (2020a); [h]Glatt et al. (2009).

We plot the $m_{\rm F275W}-m_{\rm F336W}$ vs. $m_{\rm F336W}-m_{\rm F438W}$ two-color diagrams of these stars in Figure 2.4 for all our sample of Galactic GCs. Previous works, based on the synergy between photometry, spectroscopy, and theoretical models, have provided empirical evidence that red HB 1G stars form in this diagram a sequence with bluer $m_{\rm F336W}-m_{\rm F438W}$ and redder $m_{\rm F275W}-m_{\rm F336W}$ color than 1G stars (e.g., Milone et al., 2012b). The physical interpretation, as stated in Section 2.1, lies in the fact that 2G stars are enhanced in nitrogen and depleted in oxygen and carbon with respect to 1G stars. Since the F336W filter includes strong NH molecular bands, 2G stars exhibit fainter $m_{\rm F336W}$ than 1G stars with a similar structure. In an analogous way, the F275W passband is affected by the OH absorption band, hence 2G will be brighter than 1G stars in this filter. Finally, the magnitude in the F438W filter is influenced by the CH G band, which makes 2G brighter than 1G stars, and by the CN band at $\sim$4200Å, which reduces the flux in this passband. Their combined effect makes 2G red HB stars slightly brighter in the F438W filter than 1G stars.

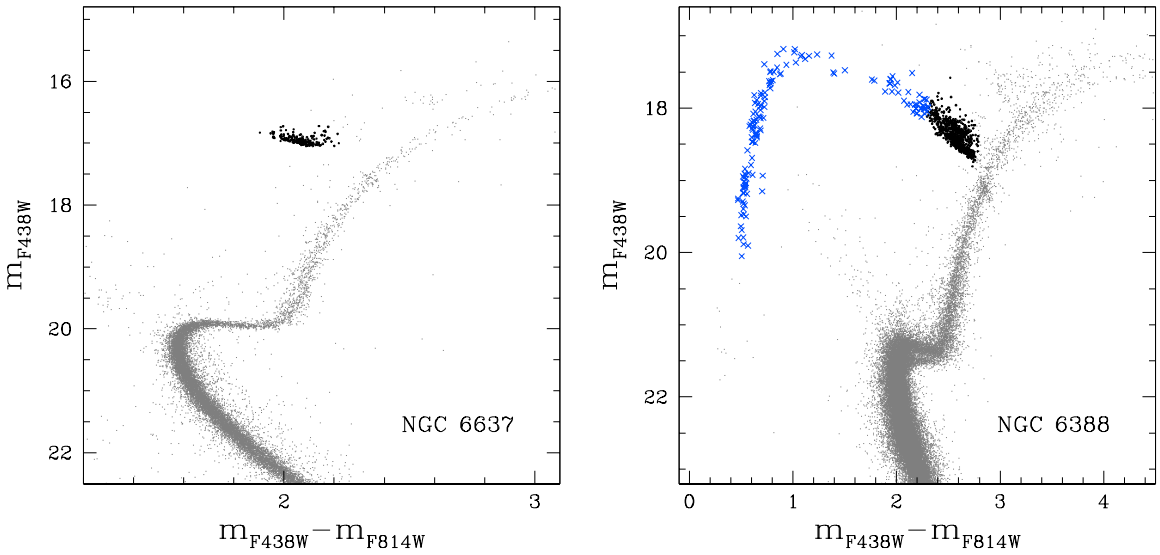

Figure 2.3: $m_{\rm F438W}$ vs. $m_{\rm F438W} - m_{\rm F814W}$ CMDs corrected for differential reddening of NGC 6388 (left) and NGC 6637 (right). Red-HB stars are colored in black, while blue-HB stars of NGC 6388 are represented with blue crosses.

In Figure 2.4, the dashed gray lines qualitatively separate the bulk of 1G from the 2G stars. To obtain them, we derive lines by eye for each cluster with the criterion of following the 2G sequence fiducial line, and then we shift them on the two-color diagram to separate the two populations.

This collection of diagrams clearly highlights that the multiple populations phenomenon is a common feature among red HB stars of Galactic GCs. Notably, the morphology of 1G and 2G stars changes dramatically from one cluster to another. For example, in GCs like NGC 6838 and NGC 6352, the 1G and 2G sequences span a similar, small interval of less than ∼0.2 mag in the $m_{\rm F275W} - m_{\rm F336W}$ color, while in NGC 6388 their extension is wider than ∼0.6 mag. Intriguingly, the 1G and 2G stars extension in NGC 6441 are very different than in NGC 6388, which is historically considered its twin cluster, with the 2G being more than two times wider than the 1G population. Finally, the complexity of multiple populations is variegated. NGC 6637 and NGC 6352 exhibit a relatively simple pattern, with two distinct groups of 1G and 2G stars alone, whereas NGC 6388 and NGC 6441, in addition to the bulk of 1G and 2G stars, show a subpopulation of 2G stars with intermediate $m_{\rm F336W} - m_{\rm F438W}$ and $m_{\rm F275W} - m_{\rm F336W}$ colors.

2.3.2 The fraction of first-generation stars

We now derive the fraction of 1G and 2G HB stars for the Galactic GCs in our sample by applying the procedure illustrated in Figure 2.5 for NGC 6637 (top panels) and NGC 6388 (bottom panels), which is similar to the method adopted by Milone et al. (2012b) for the red HB of 47 Tuc.

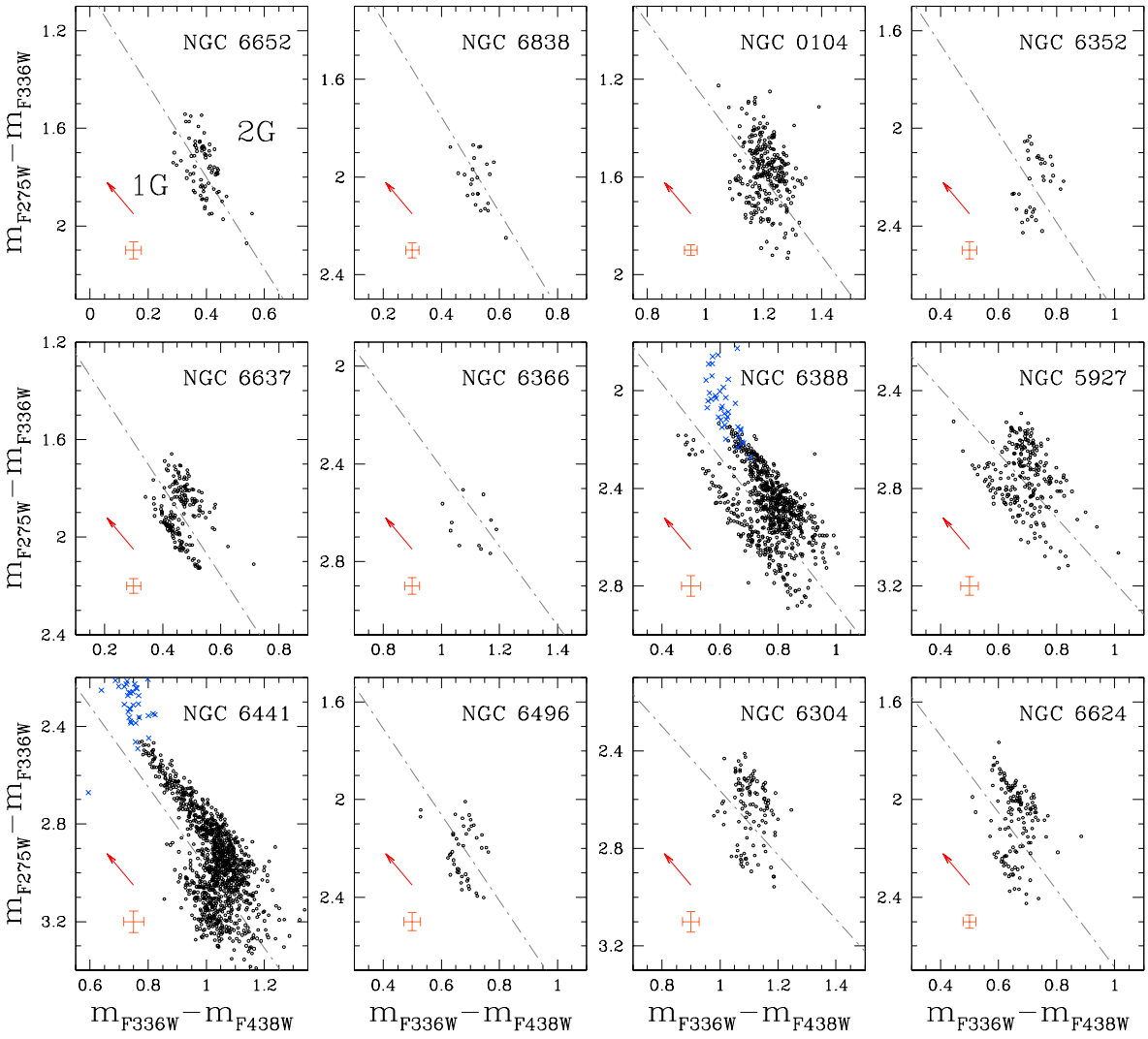

Figure 2.4: Collection of $m_{\rm F275W} - m_{\rm F336W}$ vs. $m_{\rm F336W} - m_{\rm F438W}$ differential-reddening corrected two-color diagram diagrams for the red-HB stars (black dots) of the studied Galactic GCs sorted by metallicity, from the most metal poor, to the most metal rich. Blue HB stars are represented with blue crosses. Grey dot-dashed lines separate the bulk of 1G stars from the 2G. For the sake of comparison, all the panels span the same interval of $m_{\rm F275W} - m_{\rm F336W}$ and $m_{\rm F336W} - m_{\rm F438W}$. Observational error is represented with orange bars. The reddening vectors corresponding to a reddening variation $\Delta E(B-V) = 0.1$ are represented with red arrows.

The left panels show the $m_{\rm F275W} - m_{\rm F336W}$ vs. $m_{\rm F336W} - m_{\rm F438W}$ two-color diagrams of the cluster HB stars. The gray dot-dashed lines are used to derive the verticalized $m_{\rm F275W} - m_{\rm F336W}$ vs. $\Delta(m_{\rm F336W} - m_{\rm F438W})$ diagrams, which are plotted in the middle panels and are obtained by subtracting from the $m_{\rm F336W} - m_{\rm F438W}$ color of each star the color of the fiducial line with the same $m_{\rm F275W} - m_{\rm F336W}$. Right panels portray

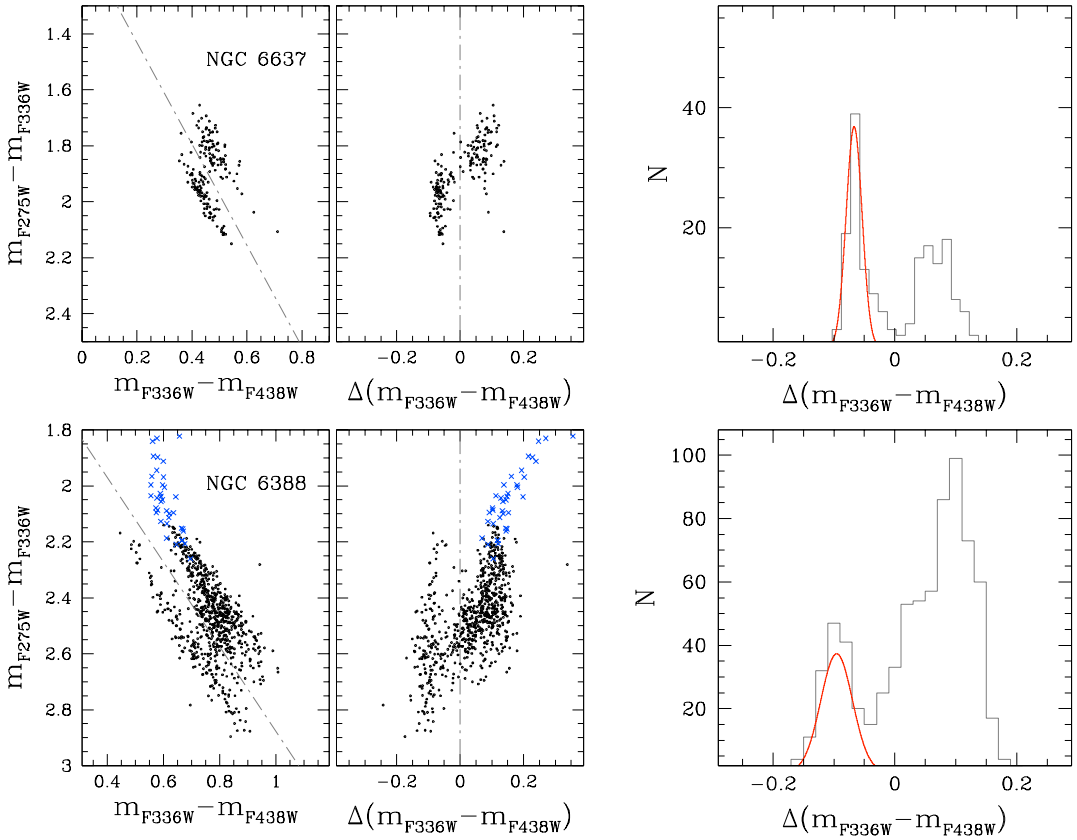

Figure 2.5: This figure summarizes the main steps to identify 1G stars along the red HBs of NGC 6637 (top panels) and NGC 6388 (bottom panels). Left panels show the $m_{\rm F275W} - m_{\rm F336W}$ vs. $m_{\rm F336W} - m_{\rm F438W}$ two-color diagram of HB stars, blue crosses in the NGC 6388 diagram are the blue HB stars. The gray dashed-dot lines separate the bulk of 1G stars from the remaining HB stars. The verticalized $m_{\rm F275W} - m_{\rm F336W}$ vs. $\Delta(m_{\rm F336W} - m_{\rm F438W})$ diagrams of HB stars are plotted in middle panels, whereas right panels show the $\Delta(m_{\rm F336W} - m_{\rm F438W})$ histogram distributions. The Gaussian function that provides the least-squares best fit with the 1G stars observed distribution is represented with the red solid line. See text for details.

the $\Delta(m_{\rm F336W} - m_{\rm F438W})$ histogram distribution, which from a visual inspection reveals two peaks, corresponding to the 1G and 2G stars. To demonstrate that the bimodality is statistically significant, we use the criterion of the bimodality coefficient[3] (BC; SAS Institute Inc. Staff, 1988), according to which a distribution of points (in our case

[3] The Bimodality coefficient is defined as

$$BC = \frac{m_3^2+1}{m_4+3\frac{(n-1)^2}{(n-2)(n-3)}} ,$$

where m_3 and m_4 are the skewness of the distribution and its excess of kurtosis and n is the number of points of a given distribution, respectively. Bimodal distributions are characterized by values of BC that exceed the critical value $BC_{\rm crit} = 0.555$.

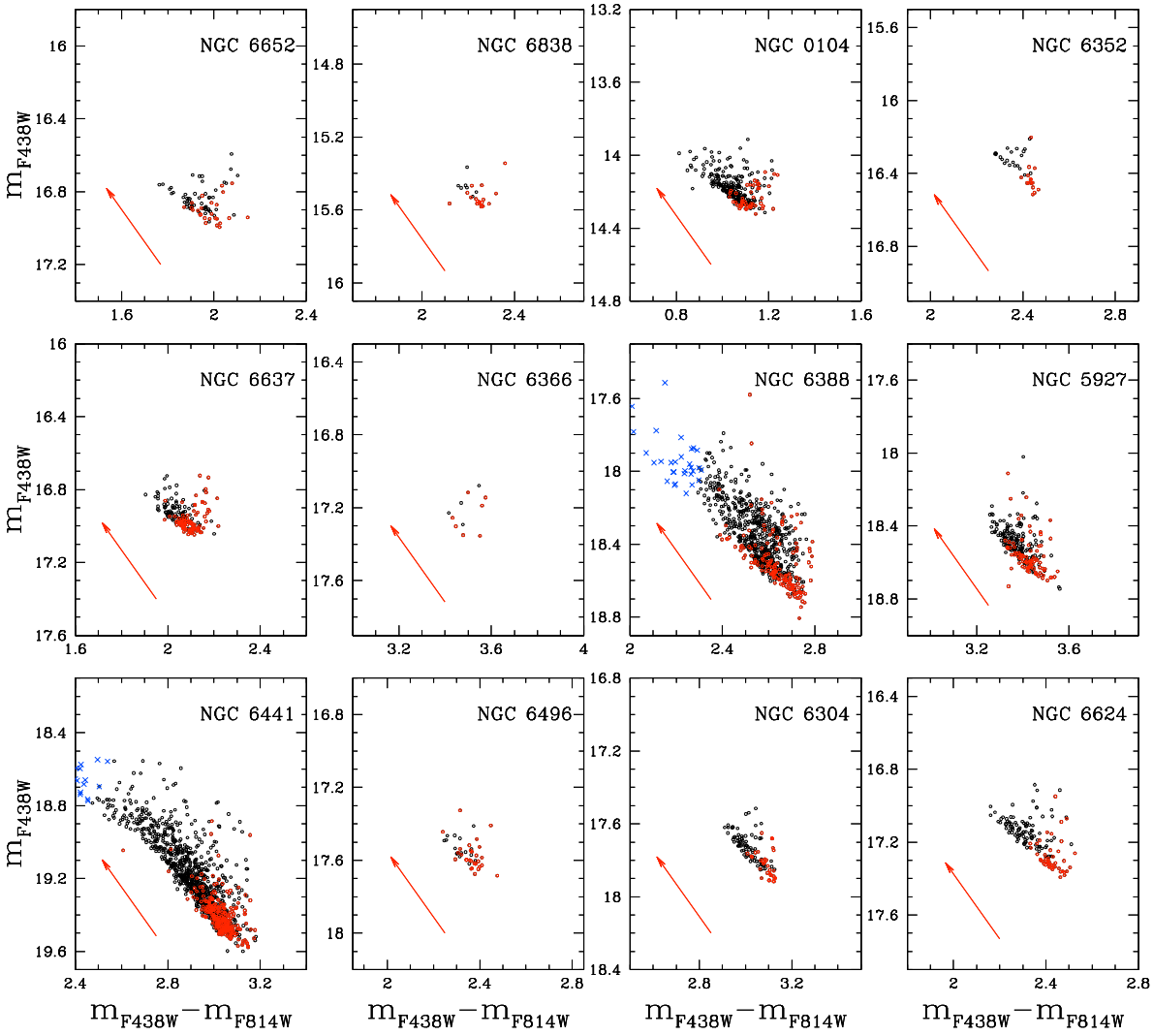

Figure 2.6: $m_{\rm F438W}$ vs. $m_{\rm F438W} - m_{\rm F814W}$ CMDs for the red-HB stars of the Galactic GCs studied in this paper. 1G and 2G stars are colored red and black, respectively. Blue crosses represent the blue HB stars.

$\Delta(m_{\rm F336W} - m_{\rm F438W})$) is bimodal if BC>0.555. The observed distributions have all BC larger than ∼0.73, thus proving the bimodal nature of the red HB stars.

To measure the fraction of 1G stars, we first select as initial-guess 1G stars the ones with $\Delta(m_{\rm F336W} - m_{\rm F438W})$ smaller than the minimum of the histogram distribution between the two peaks. We fit these stars with a Gaussian function (in red) through least squares and derived their fraction as the ratio between the area subtended by the best-fit Gaussian function and the area of the whole histogram. We verified that the results are not significantly affected by small changes in the slope of the gray lines. To ensure a proper estimate of the fraction of 1G stars in NGC 6388 and NGC 6441, blue HB stars have been included in the total number of 2G stars.

We extend this method for all the Galactic GCs of our sample. The resulting fractions of 1G stars are listed in Table 2.3 and range from ∼15% in NGC 6388 to ∼68% in NGC 6838. For 9 out of 12 Galactic GCs, namely 47 Tuc, NGC 6352, NGC 6366, NGC 6388, NGC 6496, NGC 6652, NGC 6624, NGC 6637, and NGC 6838, the fraction of 1G stars along the RGB has been derived by Milone et al. (2017a), and in NGC 6352 and NGC 6838, the fraction of 1G stars along the MS was estimated by Milone et al. (2020b), by using the same dataset. The fraction of 1G stars measured along the red HB is consistent within 1σ with the results obtained with RGB and MS stars, except NGC 6388, for which the estimate inferred in this work, namely 0.183 ± 0.012, is lower than the one derived by Milone et al. (2017a), with a difference significant at a 3σ level. Notably, our measurements provide the first measurements of population ratios in NGC 5927, NGC 6304, and NGC 6441.

We emphasize that the fractions of 1G stars provided in this Section are derived from *HST* photometry and are representative of the central cluster regions alone. Although the FoV of the majority of studied clusters encloses the half-light radius (see Table 2.2 of this paper and Table 2 by Milone et al. 2017a), the global fraction of 1G stars may differ from that observed in the central regions. Indeed, the 2G of some massive GCs is significantly more centrally concentrated than the 1G stars (e.g., Sollima et al., 2007; Bellini & Bedin, 2009; Milone et al., 2012b; Lee, 2019; Lee & Sneden, 2020).

Figure 2.6 shows the $m_{\rm F438W}$ vs. $m_{\rm F438W}-m_{\rm F814W}$ CMDs for our sample of Galactic GCs, where 1G stars are plotted with red dots. Colors made with optical magnitudes are strongly affected by $T_{\rm eff}$ variations and therefore are sensitive to helium differences between stellar populations. Furthermore, the F438W filter, as explained before, is affected by carbon and nitrogen variations. As a consequence of these effects, the 1G stars exhibit, on average, redder $m_{\rm F438W}-m_{\rm F814W}$ colors and fainter $m_{\rm F438W}$ magnitudes than the bulk of 2G stars. This fact is consistent with the previous findings that 2G stars are typically enhanced in helium and depleted in carbon with respect to the 1G (see Lagioia et al., 2018; Milone et al., 2018a; Tailo et al., 2020, for determinations of the chemical composition of 1G and 2G stars along the RGB and the HB).

2.3.3 Multiple Populations in Magellanic Cloud Clusters

In this Section, we exploit multiband photometry of 47 Tuc, which red HB has been extensively studied, to introduce new tools to disentangle multiple populations that will then be used to spot, for the first time, 1G and 2G stars along the red HB of the SMC cluster NGC 416 and the red clump of the LMC cluster NGC 1978.

In addition to F275W, F336W, and F438W observations, also F343N images are available for 47 Tuc, NGC 1978, and NGC 416. This filter is narrow and comprises the spectral region that includes the NH molecular bands, and it is particularly sensitive to nitrogen abundances. Thanks to its characteristics, we use the F343N passband to build the $m_{\rm F275W}-m_{\rm F343N}$ vs. $m_{\rm F343N}-m_{\rm F438W}$ two-color and $C_{\rm F336W,F343N,F438}$[4] vs.

[4] $C_{\rm F336W,F343N,F438}=(m_{\rm F336W}-m_{\rm F343N})-(m_{\rm F343N}-m_{\rm F438W})$

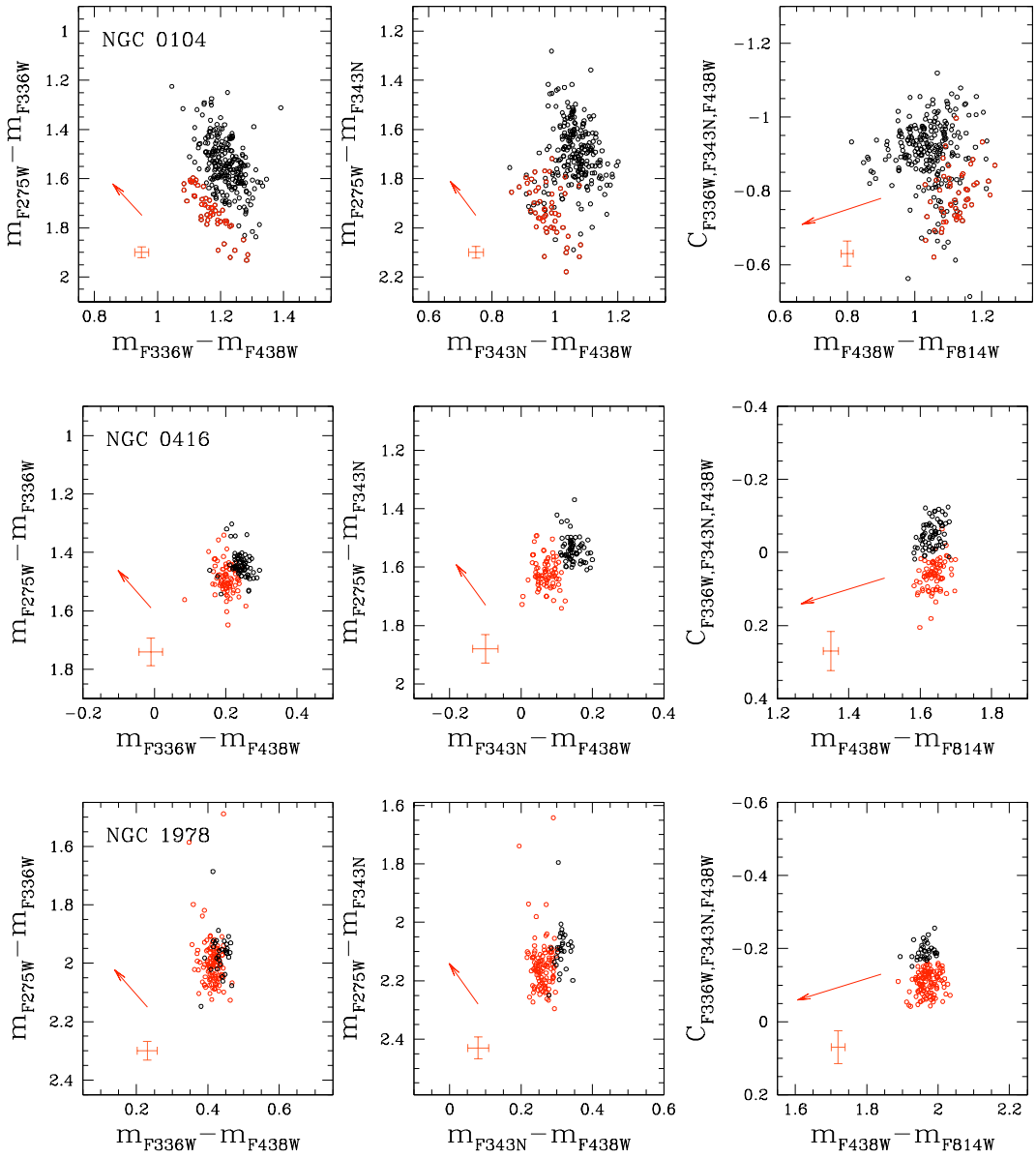

Figure 2.7: $m_{\rm F275W} - m_{\rm F336W}$ vs. $m_{\rm F336W} - m_{\rm F438W}$ (left panels), $m_{\rm F275W} - m_{\rm F343N}$ vs. $m_{\rm F343N} - m_{\rm F438W}$ (central panels) and $C_{\rm F336W,F343N,F438W}$ vs. $m_{\rm F438W} - m_{\rm F814W}$ (right panels) two-colour diagrams for 47 Tuc (upper), NGC 416 (middle) and NGC 1978 (lower). Selected 1G and 2G stars are colored red and black, respectively. Red arrows indicate the reddening vectors for $\Delta E(B-V) = 0.1$.

$m_{\rm F438W} - m_{\rm F814W}$ pseudo-two-color diagrams for the red HB and red clump stars. In the top panels of Figure 2.7, we show the effectiveness of these diagrams for 47 Tuc, where we compare the 1G-2G separation visible in the $m_{\rm F275W} - m_{\rm F336W}$ vs. $m_{\rm F336W} - m_{\rm F438W}$ (left) with the diagrams introduced in this Section (middle and right panels). The bulk of 1G and 2G stars identified in Section 2.3 (red points) still populate different regions in the $m_{\rm F275W} - m_{\rm F343N}$ vs. $m_{\rm F343N} - m_{\rm F438W}$ two-color and $C_{\rm F336W,F343N,F438}$ vs. $m_{\rm F438W} - m_{\rm F814W}$ pseudo-two-color diagrams, thus proving that they are powerful tools

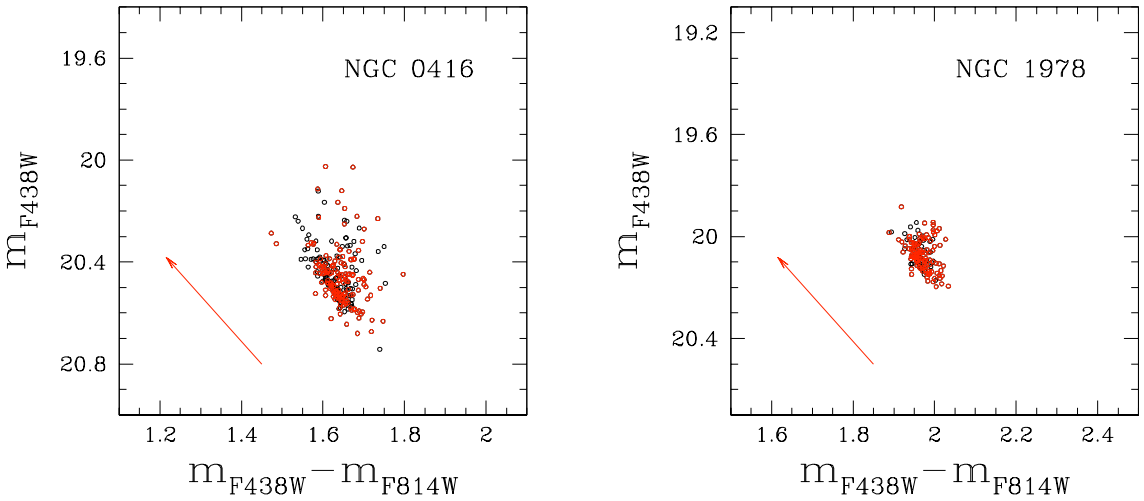

Figure 2.8: Comparison of the NGC 416 red HB (left panel) and the NGC 1978 red clump (right panel) in optical CMDs. 1G stars are colored in red.

to detect multiple populations along the red HB and the red clump.

The middle and lower rows of Figure 2.7 represent the same diagrams for NGC 416, and NGC 1978, respectively, and reveal that both clusters harbor multiple populations. For NGC 416, we use the $m_{\rm F275W} - m_{\rm F343N}$ vs. $m_{\rm F343N} - m_{\rm F438W}$ two-color diagram to identify 1G and 2G stars, while for NGC 1978 the $C_{\rm F336W,F343N,F438}$ vs. $m_{\rm F438W} - m_{\rm F814W}$ pseudo-two-color diagram is the most effective of the three in separating the different stellar populations. To these diagrams, we apply the procedure described in Section 2.3 to identify and measure the fraction of the 1G stars, finding that in contrast with what observed in most of the Galactic GCs, in which 2G constitute the majority (Milone et al., 2017a), 1G stars dominate the red HB and red clump in both NGC 416 and NGC 1978 (54.2±4.4% and 84.6±2.9%). Figure 2.8 illustrates the $m_{\rm F438W}$ vs. $m_{\rm F438W} - m_{\rm F814W}$ optical CMDs of these two clusters, where, similarly to Figure 2.6, 1G and 2G stars are represented with red and black points, respectively. While 2G stars are significantly brighter and bluer than the 1G in the optical CMDs of Galactic GCs, stars of both populations in NGC 416 and NGC 1978 are distributed along the whole red HB and red clump.

2.3.4 Comparison with simulated multiple populations

The behavior of a simple population along the red HB and red clump phases is well constrained from theory. Briefly, when a low-mass star reaches the RGB tip, the temperature in its core becomes sufficiently high, reaching $\sim 10^8$ K to ignite helium and start the HB phase, during which stars burn helium via 3α reaction, producing carbon and oxygen. At the beginning of this phase, the core mass is almost the same for all stars ($\sim 0.45\ \mathcal{M}_{\odot}$). Since the luminosity in this phase depends mainly on the core mass, these stars share about the same luminosity, resulting in a horizontal sequence in the CMDs. During this evolutionary phase, the envelope mass can vary from star to star

Table 2.3: Fractions of 1G stars of GCs measured in this paper along the HB and derived in our previous works based on the RGB (Milone et al., 2017a, 2018b; Zennaro et al., 2019; Milone et al., 2020a) and the MS (Milone et al., 2020b). $<N_{\rm 1G}/N_{\rm TOT}>$ provides the best estimates of the fractions of 1G stars, derived by combining all results. The last coloumn indicates the ratio between the maximum radius reached by the FoV and the half light radius.

ID	N_{1G}/N_{TOT} (this work)	$<N_{\rm 1G}/N_{\rm TOT}>$	$r_{\rm FoV}/r_{\rm hl}$	ID	N_{1G}/N_{TOT} (this work)	$<N_{\rm 1G}/N_{\rm TOT}>$	$r_{\rm FoV}/r_{\rm hl}$
NGC 0104	0.218 ± 0.025	0.180 ± 0.009	0.56	NGC 6397	–	0.345 ± 0.036	0.55
NGC 0288	–	0.558 ± 0.031	0.89	NGC 6441	0.210 ± 0.011	0.210 ± 0.011	2.90
NGC 0362	–	0.279 ± 0.015	2.01	NGC 6496	0.636 ± 0.068	0.666 ± 0.035	1.40
NGC 1261	–	0.359 ± 0.016	2.35	NGC 6535	–	0.536 ± 0.081	1.70
NGC 1851	–	0.264 ± 0.015	3.00	NGC 6541	–	0.396 ± 0.020	1.56
NGC 2298	–	0.370 ± 0.037	1.64	NGC 6584	–	0.451 ± 0.026	2.27
NGC 2419	–	0.370 ± 0.010	2.18	NGC 6624	0.268 ± 0.035	0.276 ± 0.020	1.87
NGC 2808	–	0.232 ± 0.014	2.32	NGC 6637	0.450 ± 0.039	0.426 ± 0.017	2.05
NGC 3201	–	0.436 ± 0.036	0.52	NGC 6652	0.380 ± 0.063	0.349 ± 0.026	3.09
NGC 4590	–	0.381 ± 0.024	1.13	NGC 6656	–	0.274 ± 0.020	0.51
NGC 4833	–	0.362 ± 0.025	0.73	NGC 6681	–	0.234 ± 0.019	2.31
NGC 5024	–	0.328 ± 0.020	1.35	NGC 6715	–	0.267 ± 0.012	2.08
NGC 5053	–	0.544 ± 0.062	0.53	NGC 6717	–	0.637 ± 0.039	2.01
NGC 5139	–	0.086 ± 0.010	0.50	NGC 6723	–	0.363 ± 0.017	1.05
NGC 5272	–	0.305 ± 0.014	0.83	NGC 6752	–	0.294 ± 0.023	0.91
NGC 5286	–	0.342 ± 0.015	2.25	NGC 6779	–	0.469 ± 0.041	1.29
NGC 5466	–	0.467 ± 0.063	0.67	NGC 6809	–	0.311 ± 0.029	0.55
NGC 5897	–	0.547 ± 0.042	0.79	NGC 6838	0.640 ± 0.083	0.630 ± 0.035	0.88
NGC 5904	–	0.235 ± 0.013	0.90	NGC 6934	–	0.326 ± 0.020	2.30
NGC 5927	0.373 ± 0.033	0.373 ± 0.033	1.52	NGC 6981	–	0.542 ± 0.027	1.67
NGC 5986	–	0.246 ± 0.012	1.81	NGC 7078	–	0.399 ± 0.019	1.79
NGC 6093	–	0.351 ± 0.029	2.52	NGC 7089	–	0.224 ± 0.014	1.47
NGC 6101	–	0.654 ± 0.032	1.48	NGC 7099	–	0.380 ± 0.028	1.55
NGC 6121	–	0.290 ± 0.037	0.39	IC 4499	–	0.510 ± 0.050	1.18
NGC 6144	–	0.444 ± 0.037	0.45	Lindsay 1	–	0.663 ± 0.037	0.65
NGC 6171	–	0.397 ± 0.031	0.90	Lindsay 38	–	1.000	1.02
NGC 6205	–	0.184 ± 0.013	1.05	Lindsay 113	–	1.000	–
NGC 6218	–	0.400 ± 0.029	0.93	NGC 0121	–	0.517 ± 0.026	2.12
NGC 6254	–	0.364 ± 0.028	0.86	NGC 0339	–	0.883 ± 0.022	0.64
NGC 6304	0.330 ± 0.046	0.330 ± 0.046	1.13	NGC 0416	0.542 ± 0.044	0.500 ± 0.025	2.20
NGC 6341	–	0.304 ± 0.015	1.63	NGC 0419	–	1.000	1.44
NGC 6352	0.417 ± 0.083	0.497 ± 0.033	0.76	NGC 1783	–	1.000	0.98
NGC 6362	–	0.574 ± 0.035	0.81	NGC 1806	–	1.000	0.14
NGC 6366	0.636 ± 0.182	0.431 ± 0.045	0.51	NGC 1846	–	1.000	1.75
NGC 6388	0.183 ± 0.0120	–	2.45	NGC 1978	0.846 ± 0.029	0.833 ± 0.025	0.82

Note. No estimate of the half light radius of Lindsay 113 is currently available in literature.

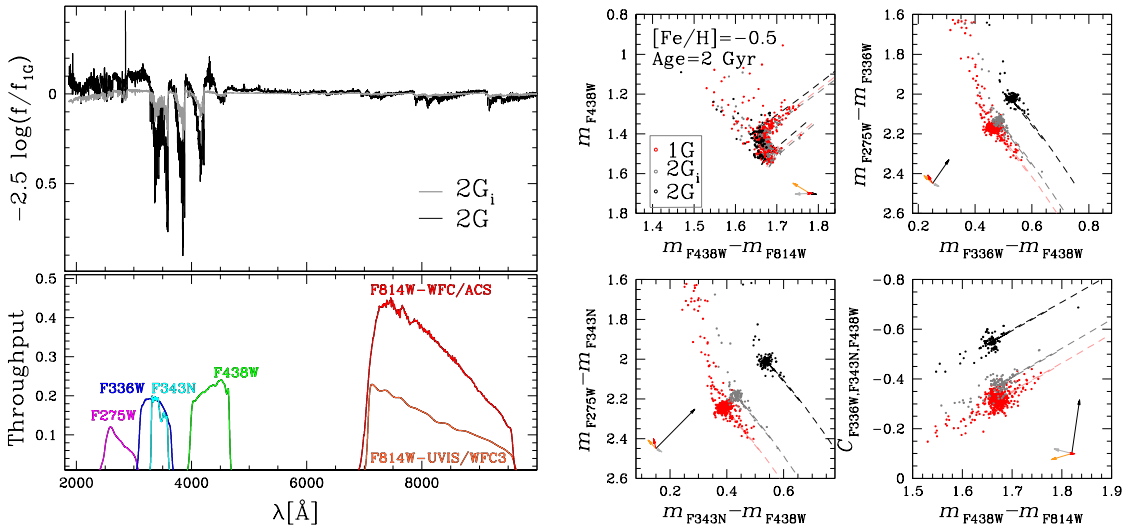

Figure 2.9: *Left panels.* Flux ratio between the spectrum of 2G (black) or $2G_i$ star (gray) and the spectrum of 1G star with $T_{\rm eff}$ = 4,898 K and $\log g$=2.46 (upper panel). The throughputs of the filters used in this paper are plotted in the bottom panel. *Right panels.* Simulated diagrams of 2-Gyr old HB stars with the same iron abundance, [Fe/H]=-0.5. Red and black dots correspond to 1G and 2G stars, respectively, while gray dots have similar chemical composition as 2G stars of NGC 1978, which are enhanced in nitrogen by 0.1 dex with respect to the 1G. The corresponding isochrones are represented with dashed lines. The gray, black, red and orange vectors indicate the effect of changing C, N, O and Fe, respectively, one at time, on the colors and magnitudes See text for details.

(e.g. Iben & Rood, 1970; Dorman, 1992). Stars with lower initial mass (or that have experienced a larger mass loss during the RGB phase) have smaller envelope masses and, therefore, redder colors. Indeed, $T_{\rm eff}$ depends on the envelope mass, becoming smaller, hence redder, towards smaller envelope masses. In a GC with multiple populations, the position of a star in this phase may also be affected by the chemical differences among GC stars (e.g. D'Antona et al., 2002; Salaris et al., 2008).

To further investigate the impact of light-element abundance variations on the colors and magnitudes of red HB and red clump stars, we perform a qualitative comparison between our observations and simulated diagrams. To do this, we start by extending to the red clump the method used for HB stars in previous works from our group, which is based on synthetic spectra with different chemical compositions (see Milone et al., 2012b; Milone et al., 2018b, for details). First, we simulate the colors and magnitudes of red-clump stars with age 2 Gyr and [Fe/H]=-0.5 by exploiting MESA isochrones (Dotter, 2016; Choi et al., 2016; Paxton et al., 2011, 2013, 2015). For this purpose, we identify six points along the isochrones retrieving their $T_{\rm eff}$ and gravities. For each point, we compute a spectrum with solar-scaled light-element abundances typical of 1G stars and compared

it with two other spectra corresponding to two populations with different realistic 2G star abundances. Specifically, we simulate a spectrum of a 2G star enhanced in nitrogen by 0.6 dex and depleted in both carbon and oxygen by 0.3 dex, and a spectrum of a stellar population (hereafter 2G$_{\rm i}$) with [C/Fe]=0.0, [N/Fe]=+0.1 and [O/Fe]=0.0 as derived by Milone et al. (2020a) for NGC 1978. We assume a microturbulence velocity of 2 km s^{-1} for all stars, which is higher than the values inferred for red-HB stars (e.g. Afşar et al., 2018). We verified that adopting microturbulence velocity of 2 km s^{-1} has negligible impact on the relative colors of 1G and 2G stars and does not change our results, thus confirming the previous conclusion by Sbordone et al. (2011). We compute atmosphere models by using the computer program ATLAS12 (Kurucz, 1970, 1993; Sbordone et al., 2004), which is based on the opacity-sampling method and assumes local thermodynamic equilibrium. We derive synthetic spectra in the wavelength interval between 1,800 and 10,000 Å by using SYNTHE (Kurucz & Avrett, 1981; Castelli, 2005; Kurucz, 2005; Sbordone et al., 2007). As an example, in the upper-left panel of Figure 2.9, we plot the wavelength against the fluxes of a 2G star and a 2G$_{\rm i}$ star with $T_{\rm eff} = 4,898$K and $\log g$=2.46, relative to the 1G star with the same atmosphere parameters. For completeness, we show in the lower-left panel the throughputs of the F275W, F336W, F343N, F438W, and F814W UVIS/WFC3 filters and the F814W ACS/WFC filter used in this paper.

We then calculate stellar magnitudes by integrating the synthetic spectra over the *HST* filter bandpasses, and we use them to derive the magnitude difference between the comparison and the reference spectrum ($\delta m_{\rm X}$). Hence, we derive the magnitudes of simulated 2G and 2G$_{\rm i}$ stars by adding to the 1G isochrones the corresponding values of $\delta m_{\rm X}$. The isochrones of 2G and 2G$_{\rm i}$ stars are finally used to derive the simulated diagrams illustrated in the right panels of Figure 2.9, where we adopt the mass function by Salpeter (1955) and assumed that the 35% of sources in the CMD are binary systems, which is the typical binary fraction inferred in intermediate-age MC star clusters (Milone et al., 2009b). We add to simulated photometry typical uncertainties of our observations as inferred from NGC 1978 by using artificial-star tests (see Anderson et al., 2008, for details).

Our simulated diagrams reveal that the 2G and 2G$_{\rm i}$ stars are almost indistinguishable from the 1G in the $m_{\rm F438W}$ vs. $m_{\rm F438W} - m_{\rm F814W}$ CMD, whereas they have higher $m_{\rm F336W} - m_{\rm F438W}$ and $m_{\rm F343N} - m_{\rm F438W}$ colors than the 1G. Moreover, 2G and 2G$_{\rm i}$ stars exhibit lower values of $m_{\rm F275W} - m_{\rm F336W}$, $m_{\rm F275W} - m_{\rm F343N}$ and $C_{\rm F336W,F343N,F438W}$ than the 1G. These color differences result from variations in carbon, nitrogen, and oxygen between the stellar populations. Indeed, the F336W and F343N filters are affected by the NH molecular bands, while the strengths of the OH and CN molecules affect F275W and F438W fluxes, respectively. As a consequence, the nitrogen-rich, carbon-poor, and oxygen-poor 2G stars display fainter F336W and F343N and brighter F275W and F438W magnitudes concerning the 1G stars.

Although a quantitative comparison between the observed and the simulated diagrams is beyond the purposes of our work, we note that the observed behavior of the selected

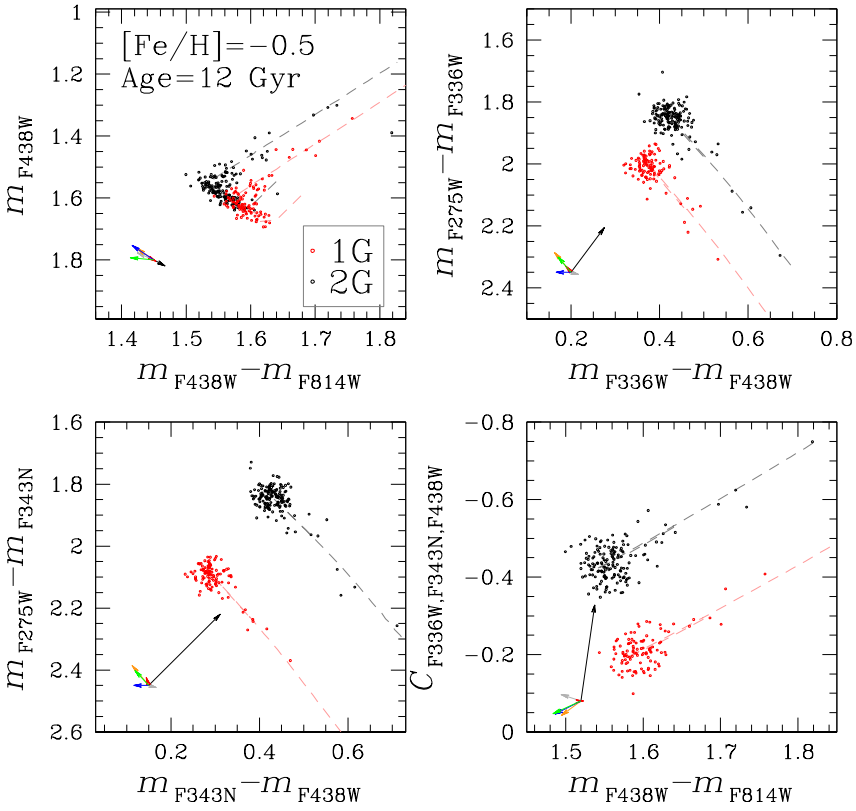

Figure 2.10: Simulated diagrams of 12-Gyr old stellar populations with [Fe/H]=-0.5. The blue, gray, black, red, orange and green vectors indicate the effect of changing helium, carbon, nitrogen, oxygen, iron, and mass loss, respectively, one at time, on the colors and magnitudes. See text for details.

stellar populations of NGC 1978 qualitatively matches the simulated 1G and $2G_i$. This fact further demonstrates that the red clump of NGC 1978 is not consistent with a simple isochrone but hosts two stellar populations with different chemical compositions.

For completeness, we investigate the effect of carbon, nitrogen, oxygen, and iron abundance variations on the diagrams Figure 2.9. The gray, black, red, and orange vectors plotted on the bottom-left corner of each panel show the average effect of changing [C/Fe], [N/Fe], [O/Fe], and [Fe/H] by -0.3, $+0.6$, -0.3 and -0.1 dex, respectively.

Finally, we repeat this approach to a population of 12-Gyr HB stars with [Fe/H]$=-0.5$. Here, we exploit α-enhanced isochrones from the Roma database (e.g. Tailo et al., 2019a, and references therein). We assume that 1G stars have solar-scaled carbon and nitrogen abundances and [O/Fe]=0.4, while 2G stars are enhanced in nitrogen by 0.6 dex and depleted in both carbon and oxygen by 0.3 dex, with respect to the 1G. We adopt helium content Y=0.25 for 1G stars and assumed that the 2G is enhanced by 1% in helium mass fraction, which is the typical helium difference between 2G and 1G stars in GCs (e.g. Lagioia et al., 2018; Milone et al., 2018b). We adopt a fraction of binaries of 0.10, which

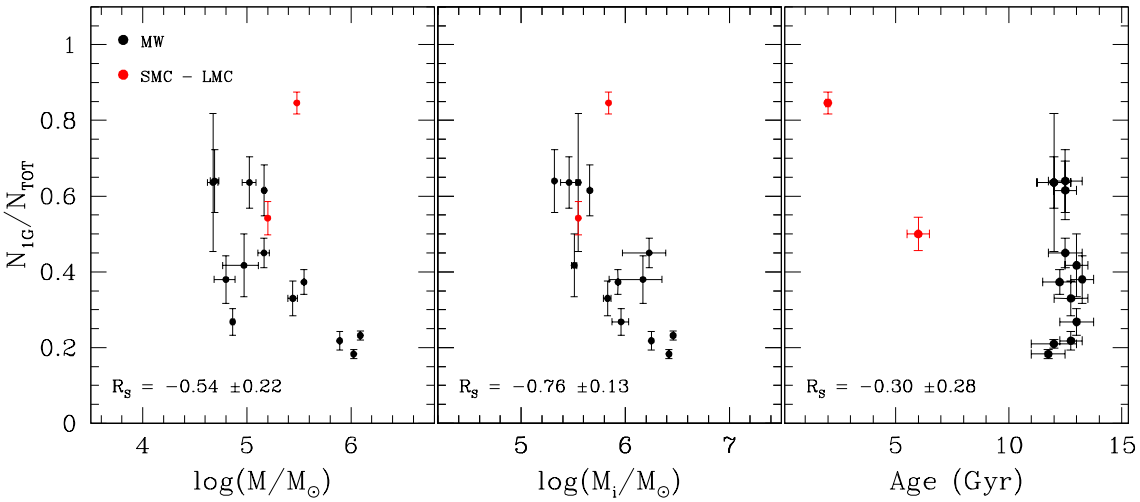

Figure 2.11: The fractions of 1G stars calculated in this work from the HB are plotted against the present-day mass (left) and the initial mass (middle) and cluster ages. Galactic GCs are shown in black, while red dots indicate the extragalactic clusters.

is consistent with results based on MS stars of GCs (e.g. Milone et al., 2016). Results are illustrated in Figure 2.10 and are qualitatively consistent with observations of Galactic GCs. Indeed, 2G stars exhibit bluer $m_{\rm F438W} - m_{\rm F814W}$ colors (upper-left panel) than the 1G, which is mostly due to the hotter temperature of helium-rich 2G HB stars. Similarly respect to the red-clump simulations, 2G stars display larger $m_{\rm F336W} - m_{\rm F438W}$ and $m_{\rm F343N} - m_{\rm F438W}$ colors and smaller values of $m_{\rm F275W} - m_{\rm F336W}$, $m_{\rm F275W} - m_{\rm F343N}$ and $C_{\rm F336W,F343N,F438W}$ (lower-left, upper-right, and lower-right panels, respectively) than the 1G. This, as before, is caused by carbon, nitrogen, and oxygen variations that impact the flux in the F275W, F336W, F343N, and F438W bands mostly through CN, CH, OH, and NH molecules. The gray, black, red, and orange arrows plotted in each panel illustrate the effect of changing [C/Fe], [N/Fe], [O/Fe], and [Fe/H], one at a time, by -0.3, $+0.6$, -0.3 and -0.1 dex, respectively. Blue and green arrows correspond to helium mass fraction and RGB mass loss increase of ΔY=0.03 and Δ $\mathcal{M}$=0.02 $\mathcal{M}_\odot$, respectively.

2.4 Relations with the Parameters of the Host Globular Clusters

We dedicate this Section to investigate the relation between the fraction of 1G stars and the cluster mass, which represents the GC parameter with the strongest link with the multiple populations (e.g., Milone et al., 2017a, 2020a), and with the cluster age, which is also possibly associated with the phenomenon (e.g., Martocchia et al., 2018b). In the left and middle panels of Figure 2.11 we represent the relation between the 1G fraction and the present-day (M) and initial ($M_{\rm i}$) cluster mass[5], respectively. Galactic

[5] Values taken from Glatt et al. (2011); Goudfrooij et al. (2014); Baumgardt & Hilker (2018); Milone et al. (2020a).

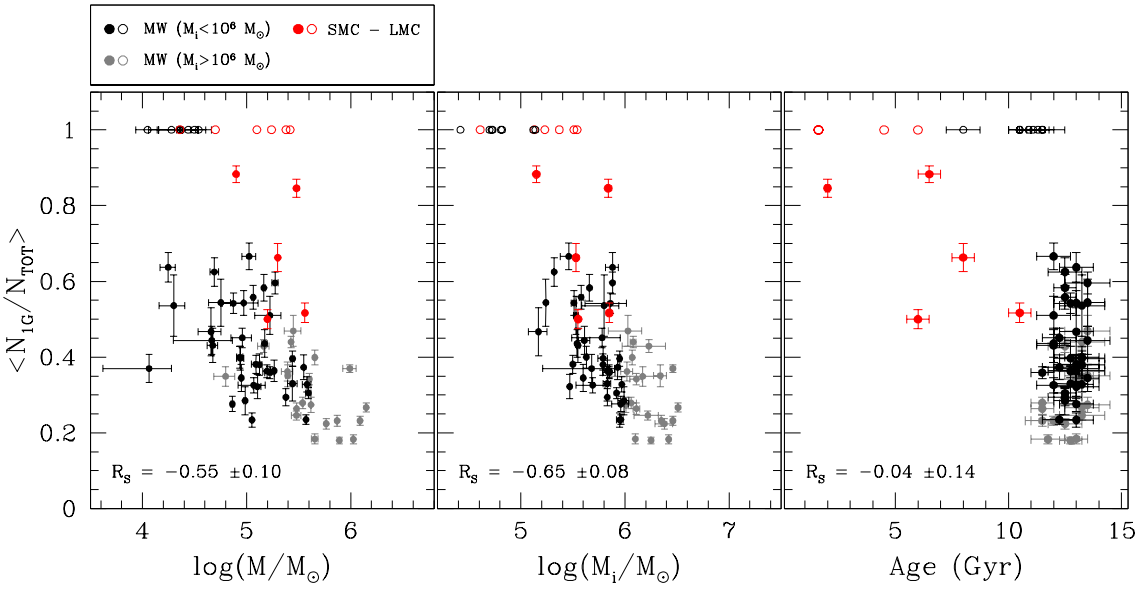

Figure 2.12: Weighted mean of the fraction of 1G stars versus the present-day mass (left) initial mass (middle) and the age of the host GC (right). Black and gray dots represent respectively Galactic GCs with M_i <10^6 $M_\odot$ and M_i <10^6 $M_\odot$, red dots represent extragalactic GCs. The cluster without MPs are represented with open circles.

and extragalactic GCs are colored in black and red. Both quantities anticorrelate with the fraction of 1G stars, as indicated by the Spearman's rank correlation coefficients, which value $R_s = -0.54 \pm 0.22$ and $R_s = -0.76 \pm 0.13$ for M and M_i, respectively. Regarding the cluster age (taken from Milone et al., 2009a; Dotter et al., 2010; Milone et al., 2014; Lagioia et al., 2019a), we do not find a significant correlation ($R_s = -0.30 \pm 0.28$), as illustrated in the right panel.

To explore these relations for a larger number of GCs, we combine our results with literature works based on RGB and MS stars (Milone et al., 2017a; Tailo et al., 2019a; Zennaro et al., 2019; Milone et al., 2020a). For the GCs with more than one independent measurement, the fractions are consistent within 1σ, with the only exception of NGC 6388 (consistent within 3σ). For them we use, as a 1G fraction value, the weighted average of the available estimates $< N_{1G}/N_{TOT} >$, which are listed in Table 2.3. In Figure 2.12, we show the same diagram of Figure 2.11 but for the extended GC sample, confirming the anticorrelation with present-day and initial masses ($R_s = -0.55 \pm 0.10$ and $R_s = -0.65 \pm 0.08$, respectively). Such anticorrelations become stronger when we also include the clusters without multiple populations (therefore populated by 1G stars only), highlighted with open symbols, providing $R_s = -0.65 \pm 0.08$ and $R_s = -0.80 \pm 0.05$ for the anticorrelation with M and M_i, respectively.

When considering GCs with multiple populations alone, we find no evidence for a correlation ($R_s = 0.04 \pm 0.14$), independently whether we consider cluster with initial mass smaller and bigger than $10^6 M_\odot$ (black and grey points, respectively). The result

changes when including the simple populations' star clusters, showing that the 1G star fraction anticorrelates with the age ($R_s = -0.60 \pm 0.07$). This finding is a consequence of the fact that all analyzed old GCs (age ∼12 Gyr) host multiple populations, while the clusters with simple stellar populations are all younger than the bulk of Galactic GCs.

2.5 The Color and Magnitude Extensions of 1G Stars

One intriguing feature highlighted by Figure 2.4 is that the extension of the 1G sequence in the two-color diagram significantly changes from one cluster to another. The comparison between NGC 6388 and NGC 6441, which are traditionally considered twin clusters[6] provides the most striking example. Indeed, while the first shows a notably extended 1G star distribution, the latter span a relatively small $m_{\rm F275W} - m_{\rm F336W}$ and $m_{\rm F336W} - m_{\rm F438W}$ color intervals.

To explore in more detail the difference in the red HB morphology of these two clusters, we plot in the left and middle panels of Figure 2.13 the $m_{\rm X}$ vs. $C_{\rm F275W,F336W,F438W}$ diagram, where X = F275W, F336W, F438W, F606W, and F814W. In each panel, the two brown horizontal dot-dashed lines indicate the 10th (upper) and 90th (lower) percentiles of the magnitude distribution. We define as the magnitude width of the 1G red HB stars, $W_{\rm X}^{1G,rHB}$, the difference between the two lines. We plot this quantity as a function of the considered filter in the upper- and lower-right panels for 1G stars in NGC 6441 and NGC 6388, respectively. The magnitude extension of the NGC 6388 1G stars is slightly larger (of about 0.1 mag) in the F438W, F606W, and F814W filters whereas at lower wavelengths the difference dramatically increases, reaching its maximum in the F275W band, where $W_{\rm F275W}^{1G,rHB}$ of NGC 6388 is ∼0.45 mag larger than that of NGC 6441.

We now use NGC 6441 as a template case to investigate the physical mechanism that produces the extended 1G sequence. In Figure 2.14, we compare its observed $W_{\rm X}^{1G,rHB}$ with those derived from simulated HBs that account for observational errors and correspond to a simple population with pristine helium abundance and with age of 12 Gyr and [Fe/H] = -0.5, which are realistic values for this GC (Harris, 1996; Dotter et al., 2010). The resulting extensions are represented with the open gray squares and do not match the observed behavior, thus demonstrating that the 1G of NGC 6441 is composed of chemically different stars.

Literature works based on MS and RGB stars revealed that 1G stars of most studied clusters exhibit extended sequences in the ChM (Milone et al., 2015, 2017a). By analyzing this phenomenon using multiband photometry, the spread appears to be consistent with either star-to-star helium variations (e.g., Milone et al., 2015, 2018b), or with intrinsic metallicity spread (e.g., D'Antona et al., 2016; Tailo et al., 2019b). The latter hypothesis is supported by the spectroscopic observation of iron abundances among 1G

[6] NGC 6388 and NGC 6441 share very similar masses, metallicities ([Fe/ H]∼-0.50), and they are both located close to the Galactic bulge. The existence of bHB stars in these clusters was an unexpected feature given their relatively high metallicity (e.g., Rich et al., 1997) and was considered one of the earliest signatures of stellar populations with extreme helium abundances in GCs (D'Antona & Caloi, 2008; Tailo et al., 2017, and references therein).

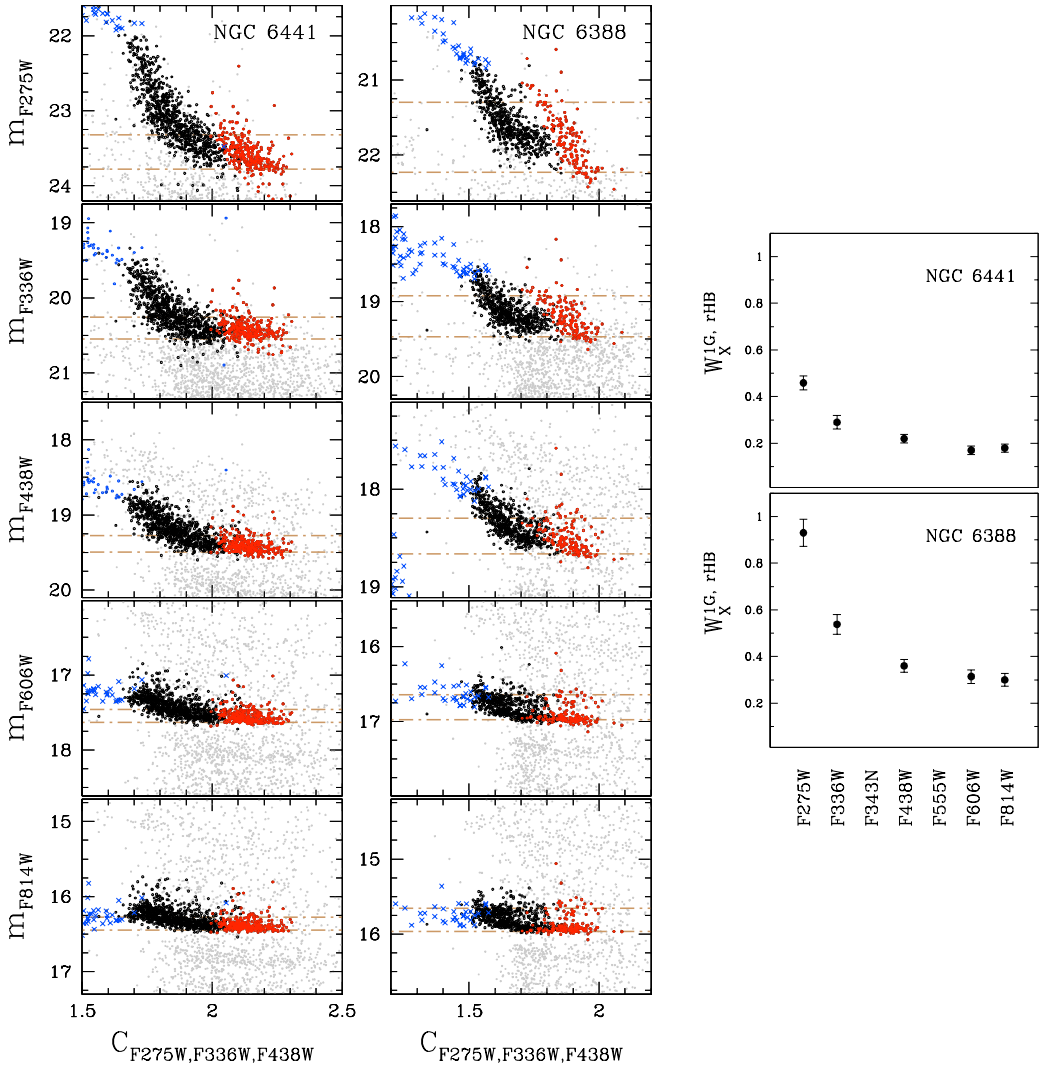

Figure 2.13: Comparison between the red HBs of NGC 6441 (left panels) and NGC 6388 (middle panels) in the $m_{\rm X}$ vs. $C_{\rm F275W,F336W,F438W}$ planes, where X=F275W, F336W, F438W, F606W and F814W. 1G stars, 2G red-HB, and 2G blue-HB stars are colored red, black and blue, respectively, while the remaining clusters stars are represented with gray points. The two brown horizontal dot-dashed lines mark the $10^{\rm th}$ and $90^{\rm th}$ percentile for the magnitude distribution of 1G stars. Right panels show the magnitude extension of 1G stars, $W_{\rm X}^{\rm 1G,rHB}$, for the available filters.

stars of NGC 3201 (Marino et al., 2019a).

Driven by these findings, we simulate the red HB of a stellar system composed of two stellar populations with pristine helium and different iron ([Fe/H] -0.5 and -0.6, so with a Δ[Fe/H]=-0.1), and repeated the procedure introduced in Figure 2.13 to measure their $W_{\rm X}^{1G,rHB}$ (red triangles in Figure 2.14). We then simulate the red HB of a stellar system with two populations with the same [Fe/H] and different helium abundances

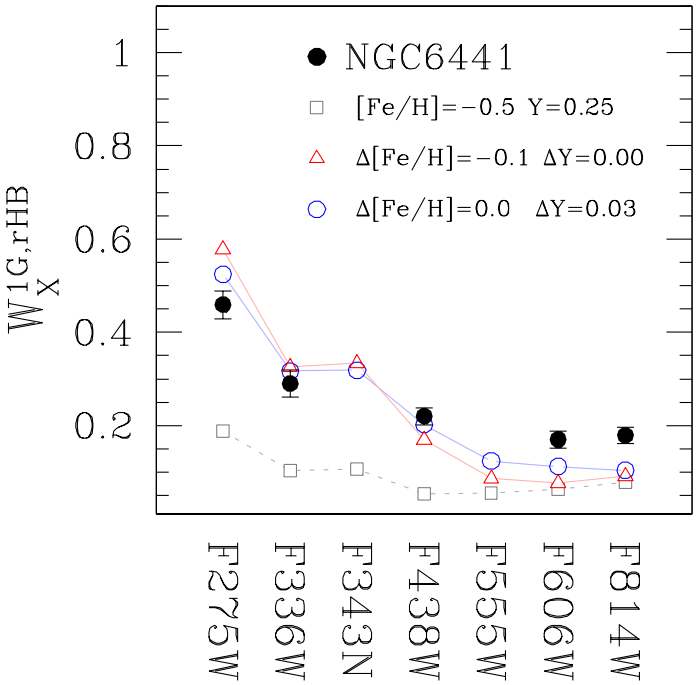

Figure 2.14: Comparison between the observed magnitude extension of 1G stars along the red HB of NGC 6441 (black circles) and simulated HBs with different helium contents and metallicities. Gray squares correspond to a simple stellar population with [Fe/H]=−0.5 and pristine helium abundance (Y=0.25), red triangles represent a stellar system composed of two stellar populations with pristine helium content and [Fe/H]=−0.5 and [Fe/H]=−0.6, whereas blue circles correspond to a stellar system composed of two stellar populations with the same [Fe/H] and helium abundances Y=0.25 and Y=0.28.

of $Y = 0.25$ and $Y = 0.28$ (blue circles). The simulated HBs are derived from the stellar models by Tailo et al. (2016, 2020). We determine the mass of each HB star as $\mathrm{M^{HB}} = \mathrm{M^{Tip}} - \Delta\mathrm{M}(\mu, \delta)$, where $\mathrm{M^{Tip}}$ is the mass at the RGB tip derived from the best-fit isochrone and $\Delta\mathrm{M}$ is the mass lost by the star during the RGB. Specifically, we adopt a Gaussian profile for $\Delta\mathrm{M}$, with an average mass loss of 0.25 $M_\odot$ and mass loss dispersion of $0.006 M_\odot$, which is the average value inferred by Tailo et al. (2020) for the studied GCs.

A visual inspection of Figure 2.14 shows that variation of either helium or [Fe/H] content of red HB stars can reproduce the observed $W_{\mathrm{X}}^{1G,rHB}$ distribution. In particular, the observed trend is consistent both with two populations with a Δ[Fe/H]= -0.1 or with a ΔY= 0.03. As a consequence, similarly to what was observed by Milone et al. (2017a), our dataset does not allow us to disentangle between the effects of iron and helium variations as the main driver of the 1G sequence extension in NGC 6441, since a spread in either quantities is consistent with the 1G stars extension also in all the other

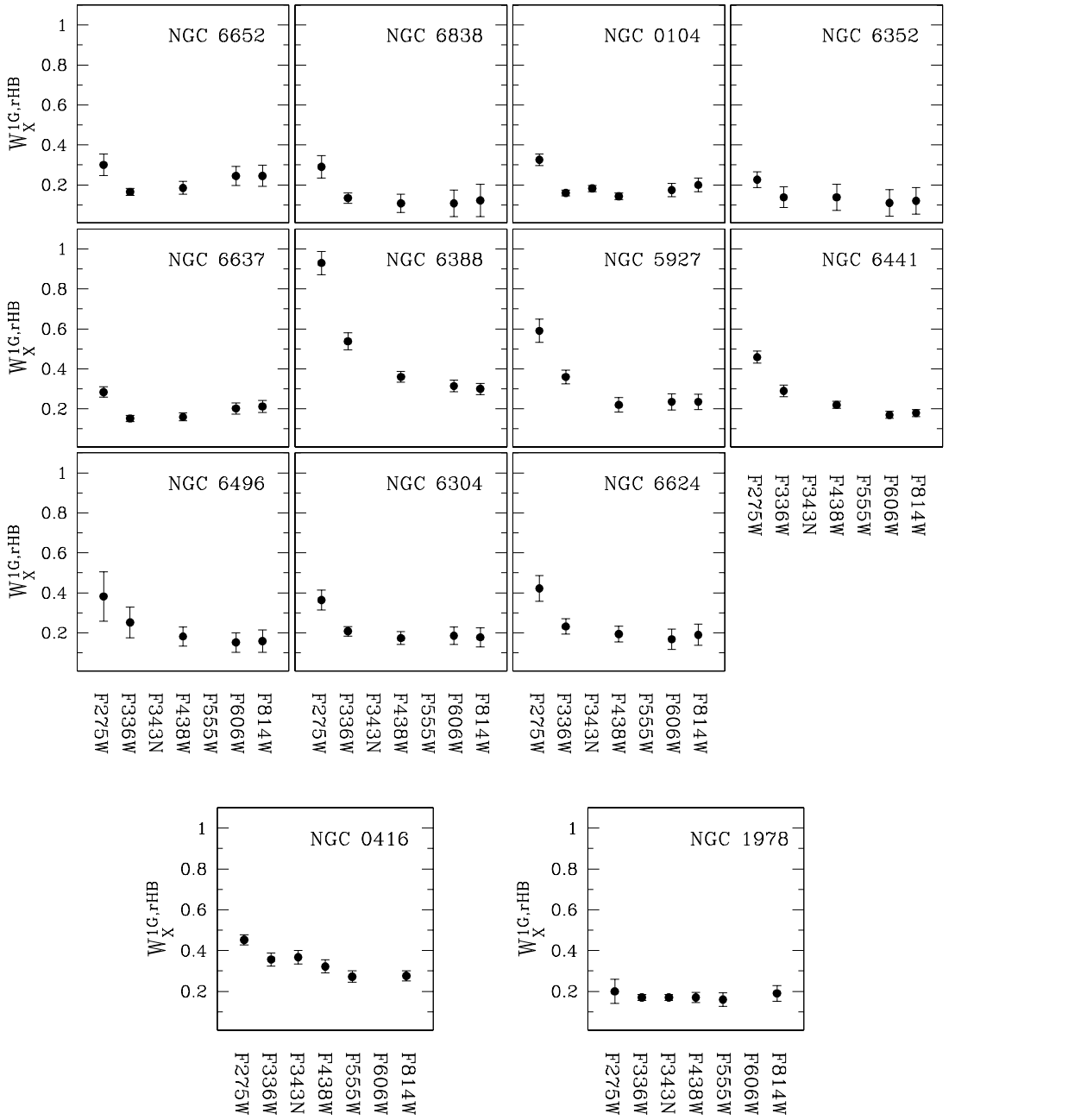

Figure 2.15: Width of 1G stars along the red HB in the X magnitude, $W_X^{1G,rHB}$, for Galactic and extragalactic GCs, as a function of the various filters used in this work.

GCs.

In Figure 2.15, we show the $W_X^{1G,rHB}$ distribution of all the clusters in our sample. The larger extension in the F275W filter is a common feature among the studied GCs, except NGC 1978, where it is nearly constant in every band. In the F336W filter, the extension is significantly wider than in optical bands for NGC 416, NGC 5927, NGC 6388, and NGC 6441, whereas in other clusters no large difference is present. In NGC 6637 and NGC 6652, the F336W and F438W magnitude extensions are slightly narrower than

Table 2.4: Extension of the F336W-F438W color of 1G red HB stars and whole red HB stars of Galactic and extragalactic clusters of our sample.

CLUSTER	$W^{\rm 1G,rHB}_{\rm F336W,F438W}$	$W^{\rm rHB}_{\rm F336W,F438W}$	CLUSTER	$W^{\rm 1G,rHB}_{\rm F336W,F438W}$	$W^{\rm rHB}_{\rm F336W,F438W}$
NGC 0104	0.120 ± 0.018	0.138 ± 0.009	NGC 6624	0.102 ± 0.021	0.120 ± 0.011
NGC 5927	0.200 ± 0.018	0.180 ± 0.013	NGC 6637	0.104 ± 0.014	0.110 ± 0.006
NGC 6304	0.123 ± 0.020	0.100 ± 0.012	NGC 6652	0.125 ± 0.028	0.100 ± 0.014
NGC 6352	0.060 ± 0.008	0.095 ± 0.016	NGC 6838	0.090 ± 0.028	0.094 ± 0.023
NGC 6388	0.250 ± 0.018	0.210 ± 0.008	NGC 1978	0.050 ± 0.006	0.051 ± 0.007
NGC 6441	0.140 ± 0.012	0.200 ± 0.008	NGC 0416	0.060 ± 0.007	0.080 ± 0.006
NGC 6496	0.095 ± 0.034	0.107 ± 0.023			

those in F606W and F814W.

We now explore the relation between the color extension of the 1G sequence among the red HB and the RGB stars. To do that, we exploit the $W^{1G,rHB}_{\rm F336W,F438W}$ width derived as the difference between the 90th and the 10th percentile of the $m_{\rm F336W} - m_{\rm F438W}$ color distribution of 1G red HB stars, which we list in Table 2.4. The upper-left panel Figure 2.16 compares this quantity with the RGB width of the x-axis of the ChM (Milone et al., 2017a), showing a correlation between them. In the upper-middle panel, we illustrate the relationship with the GC mass, finding a mild correlation. Finally, as portrayed in the upper-right panel, no correlation with the cluster age is detectable from our dataset. For completeness, we extend the analysis to the whole red HB and derive the corresponding color width $W^{rHB}_{\rm F336W,F438W}$, listed in Table 2.4. In analogy with what was observed for the 1G stars only, $W^{rHB}_{\rm F336W,F438W}$ correlates with the RGB width and the cluster mass, while there is no correlation with the age, as represented in the lower panels of Figure 2.16.

2.6 Radial Distribution of Multiple Populations

To investigate the radial distribution of multiple populations, we combine our photometry, which covers the central $\sim$2.7$\times$2.7 arcmin^2, with the ground-based catalogs published by Stetson et al. (2019), able to reach the clusters outskirts thanks to its wide FoV. This was possible for four GCs, namely 47 Tuc, NGC5927, NGC 6366, and NGC 6838.

Previous works show that the U and B magnitudes are useful tools to build photometric diagrams to disentangle 1G and 2G stars (e.g., Marino et al., 2008; Milone et al., 2012b; Monelli et al., 2013). To further prove that we can observe the counterpart of the 1G and 2G red HB stars spotted with the *H*ST-based catalog even with UBVI photometry, we exploit both observations and simulated photometry. The upper panels

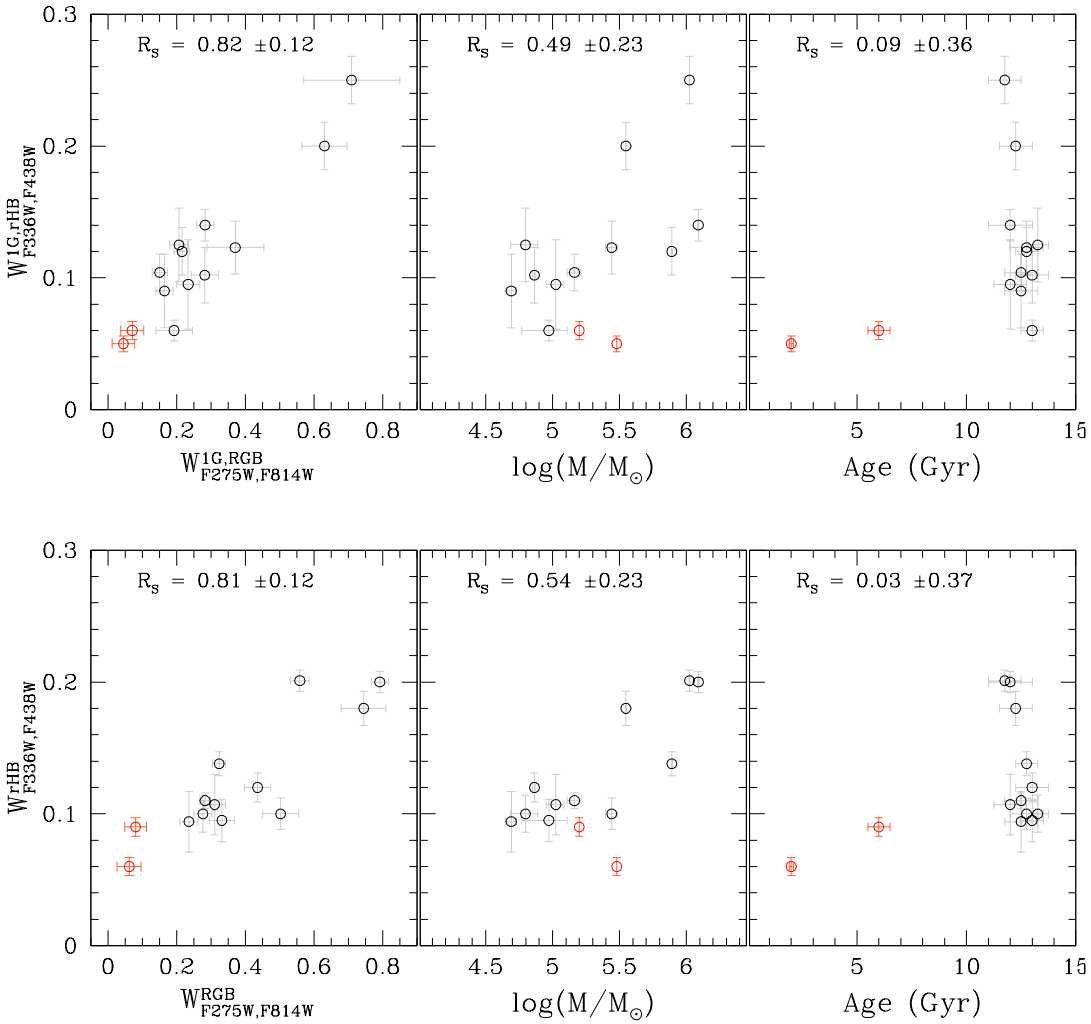

Figure 2.16: *Upper panels:* $m_{\rm F336W} - m_{\rm F438W}$ color extension of 1G stars along the HB against the width of 1G RGB stars along the ChM $W^{\rm 1G,RGB}_{\rm F275W,F814W}$ (from Milone et al., 2017a, left panel), the mass of the host GC (from Baumgardt & Hilker, 2018, middle panel) and GC ages (from Dotter et al., 2010, right panel). The Spearman rank correlation coefficients are quoted on top of each panel. *Lower panels:* Same as the upper panels, but for the $m_{\rm F336W} - m_{\rm F438W}$ color extension of stars along the whole red HB.

of Figure 2.17 show the $m_{\rm F275W} - m_{\rm F336W}$ vs. $m_{\rm F336W} - m_{\rm F438W}$ two color diagram (left) and the V vs. $C_{\rm U,B,I} = B - 2V + I$ diagram (right) for NGC 6838. In the lower panels, we show simulations obtained as explained in Section 2.3.4 for two 12 Gyr old populations with [Fe/H] = -0.5 and helium, carbon, nitrogen, and oxygen abundances consistent with typical 1G and 2G stars values. In both diagrams, the two populations are well separated and describe patterns qualitatively similar to the observations. In both observed and simulated diagrams, we plot in red and black 1G and 2G stars, respectively.

To estimate the fraction of 1G and 2G red HB stars with the V vs. $C_{\rm U,B,I}$ diagram, we apply the procedure illustrated in Figure 2.18. The $C_{\rm U,B,I}$ histogram distribution shows

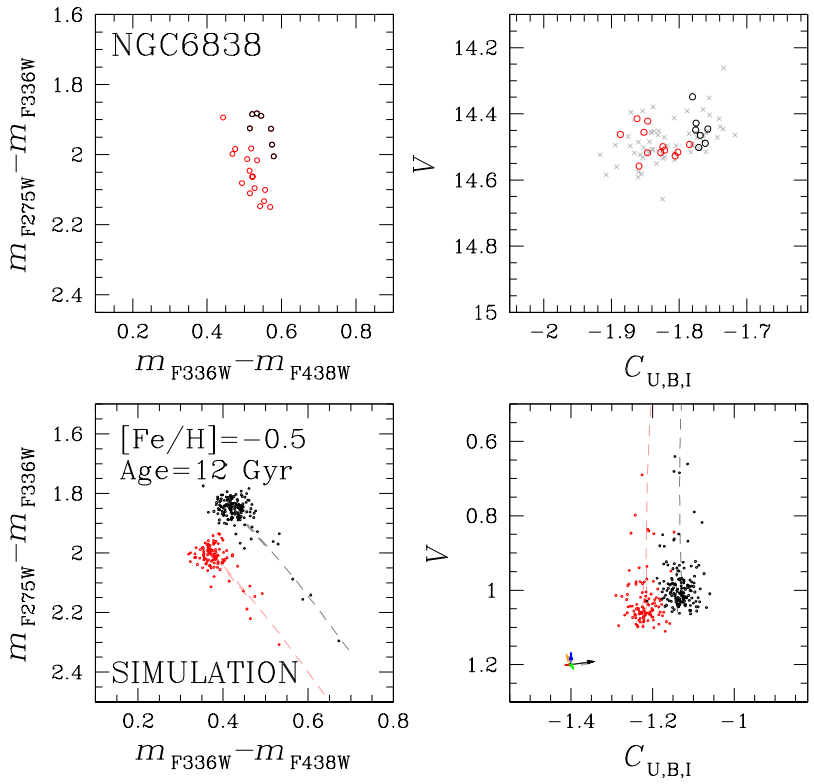

Figure 2.17: Comparison between $m_{\rm F275W}-m_{\rm F336W}$ vs. $m_{\rm F336W}-m_{\rm F438W}$ (left) and V vs. $C_{\rm U,B,I}$ (right) diagrams for red-HB stars. Upper panels show the observed diagrams of NGC 6838 from *H*ST and ground-based photometry. 1G and 2G stars are plotted red and black, respectively, in both panels. Lower panels illustrate results for simulated diagrams. The arrows displayed in the lower-right panel are defined as in Figure 2.10.

two clear peaks, which are fitted by a bi-Gaussian function by means of least squares, represented in black. The Gaussian components corresponding to 1G and 2G stars are drawn in red and blue, respectively, and their relative numbers are derived by comparing the area below the respective Gaussian functions.

We find that in 47 Tuc the fraction of 2G stars in the ground-based catalog (which covers a radial range between about 1.5 and 24 arcmin) values 0.67±0.02, and it is significantly smaller than what is inferred by considering the innermost area with *H*ST data (0.78±0.03). NGC 5927 shows a similar behavior, with the 2G stars fraction being 0.63±0.03 and 0.58±0.03 in the *H*ST and ground-based photometry, respectively (the latter covering a ∼0.5-6.0 arcmin interval). Hence, these results are consistent with the two clusters having the 2G stars more centrally concentrated than the 1G stars. On the contrary, in NGC 6366 and NGC 6838, where we explore up to about 8 and 9 arcmin, respectively, no significant differences are detected concerning *H*ST photometry in the central field.

To further investigate the radial distribution of multiple populations, we divide the

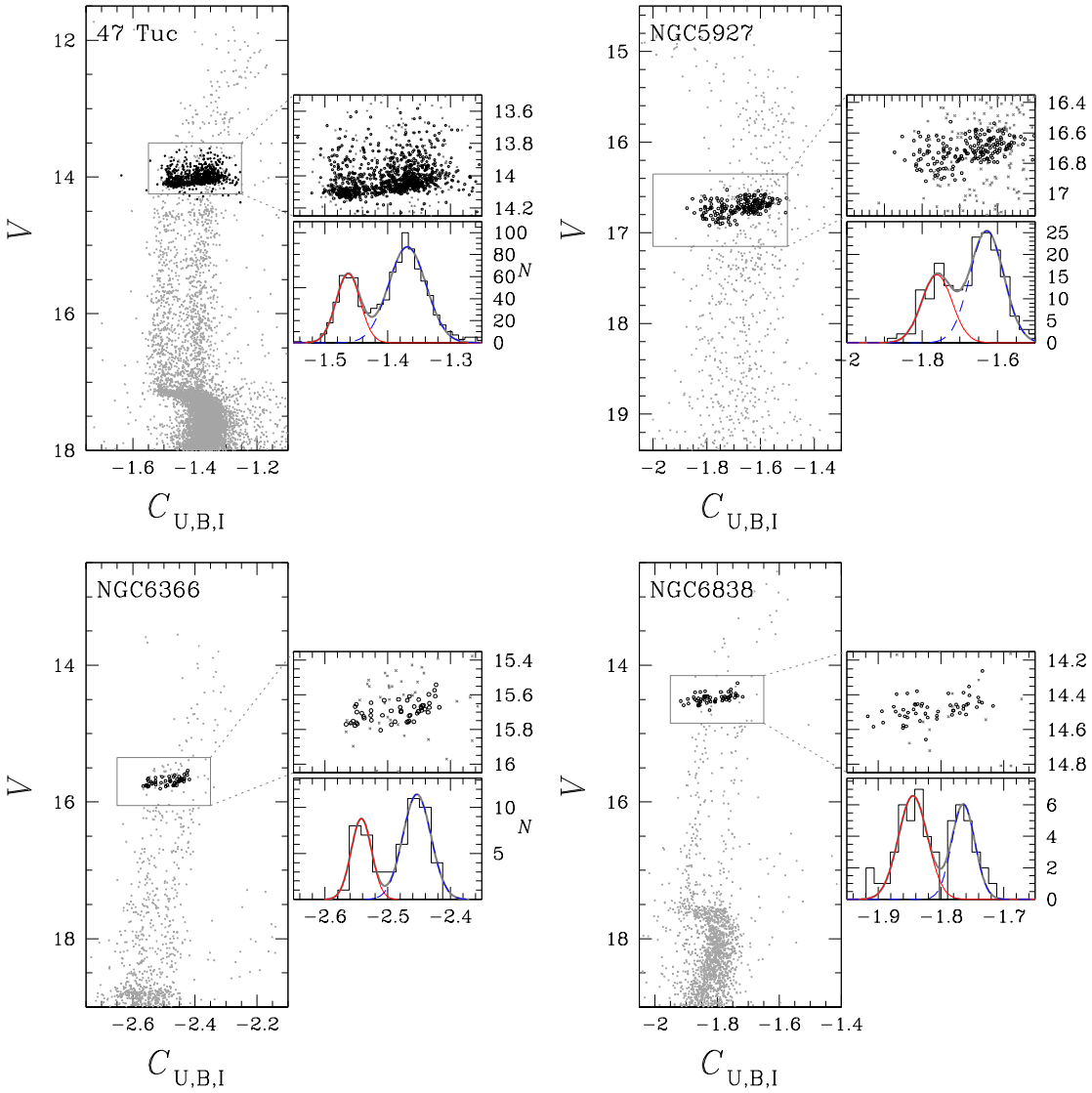

Figure 2.18: V vs. $C_{\mathrm{U,B,I}}$ pseudo two-color diagrams of selected cluster members of 47 Tuc, NGC 5927, NGC 6366 and NGC 6838 from ground-based photometry (Stetson et al., 2019). Red-HB stars are marked with black dots, while the remaining stars are plotted with gray dots. A zoom of the CMD region around the HB is provided in the small panels on the right together with the histogram distributions of $C_{\mathrm{U,B,I}}$ for red-HB stars. The red and blue curves superimposed on the histogram represent the Gaussian functions that provide the best fit of the two peaks.

ground-based FoV into equal-number radial bins, repeating the procedure introduced in Figure 2.18 to infer the 1G and 2G stars fraction in each bin. Figure 2.19 displays the radial distribution of 2G red HB stars fraction, where the dashed and dot-dashed gray lines represent the core and half-light radius, respectively (taken from Harris 1996 for Galactic GCs; McLaughlin & van der Marel 2005 for NGC 416; and from Fischer

et al. 1992 for NGC 1978). We confirm that both 47 Tuc and NGC 5927 have their 2G stars fraction drop when moving to the cluster outskirts. In 47 Tuc it is maximum in the center and consistent with a flat distribution up to ∼0.7 half-light radii, dropping around the half-light radius and decreasing slightly moving outwards, reaching its minimum of about 0.55. Similarly, in NGC 5927 the fraction of 2G stars is nearly constant up to ∼1.5 half-light radii, to then drop at higher distances, reaching its minimum of ∼0.4 around three half-ligh radii. We then confirm the absence of a significant gradient in NGC 6366 and NGC 6838.

For the rest of the clusters in our sample, where there is no available ground-based photometry, we explore the radial distribution of multiple populations by using *H*ST photometry alone, hence, we are limited in the innermost ∼1 arcmin. We repeat the procedure explained in Section 2.3.2 for different radial bins, which include a similar number of HB stars. Figure 2.20 displays their radial distributions. In this limited FoV, we find that the majority of GCs are consistent with having a flat 2G stars radial distribution. NGC 416 is a possible exception, with a drop in their 2G fraction of about 0.2 around its core radius.

To infer the statistical significance of the derived radial distribution gradients, we run 10,000 simulations where 1G and 2G follow a flat radial distribution, to test the null hypothesis that the observed profiles are produced by statistical fluctuations. For each simulation, the radial distribution is obtained starting from the observed $N_{\rm 2G}/N_{\rm TOT}$ weighted-average ratios across the covered radial interval and then adding up a random radial scatter based on the observed errors. By using a chi-square test, we then measure the deviation from flatness for each simulation, represented by $\chi^2_{\rm sim}$. Finally, we compare these values with $\chi^2_{\rm obs}$ and determine the number of simulations for which $\chi^2_{\rm sim} > \chi^2_{\rm obs}$. This number, divided by the total number of simulations, estimates the *p* value, i.e. the probability that the null hypothesis is true, hence that the observed radial distribution is produced by an intrinsically flat one. Typically, the null hypothesis is considered discarded when the *p* value is smaller than 0.05. This happens in 47 Tuc, NGC 5927, and NGC 416, so that for these three GCs the observed scatter can be truly associated with a non-flat radial distribution. *p* values of all the analyzed clusters are reported in Table 2.5.

Our findings for 47 Tuc are in agreement with similar measurements previously done in literature, which concluded that 2G stars are more centrally concentrated than 1G (e.g., Milone et al., 2012b; Cordero et al., 2014). For three GCs in our sample, namely NGC 1978, NGC 6624, and NGC 6637, Dalessandro et al. (2018) studied the radial distribution of multiple populations, quantifying the difference between their 1G and 2G stars by using the area enclosed between their cumulative radial distribution, A^+, within two half-light radii from the center. Although we cannot quantitatively compare our results with the ones by Dalessandro and collaborators, since we adopt different methods, we notice that both NGC 6624 and NGC 6637 exhibit A^+ close to zero, qualitatively consistent with our finding of similar radial distribution between their populations. On the contrary, their results for NGC 1978 disagree with this work, for which Dalessandro et al. (2018) found -0.081, thus a more centrally-concentrated 2G.

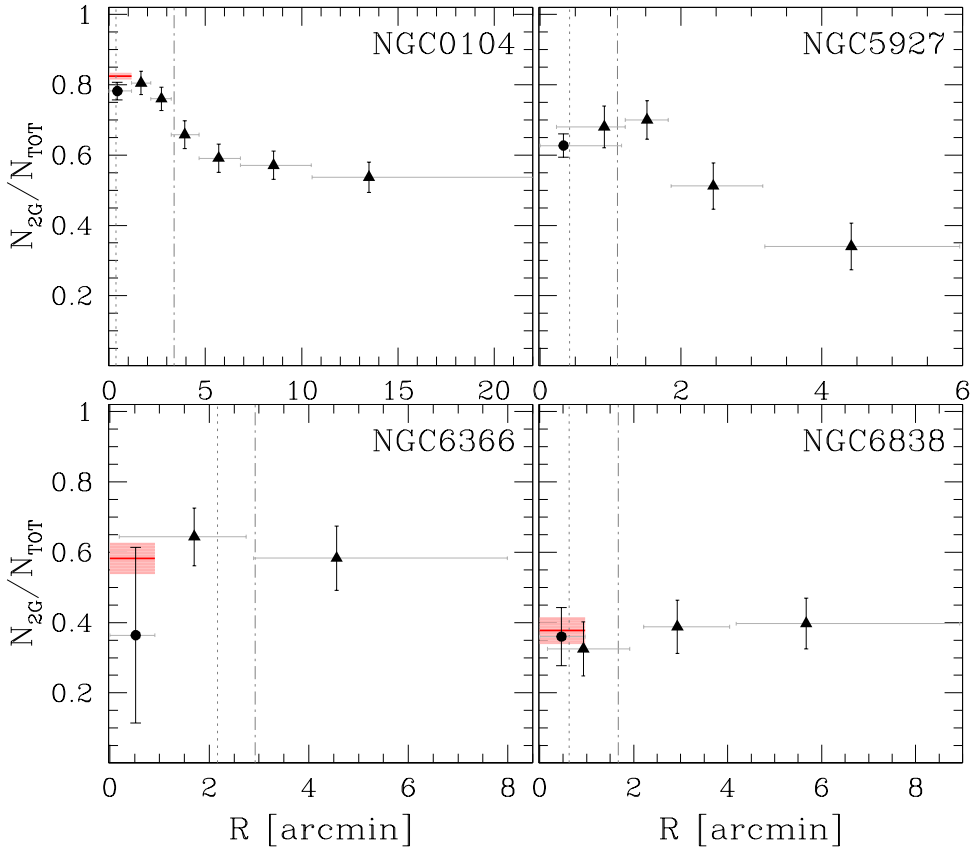

Figure 2.19: Fraction of 2G stars as a function of radial distance for 47 Tuc, NGC 5927, NGC 6366 and NGC 6838. Black circles and triangles mark the results derived from *H*ST and ground-based photometry, respectively. Gray horizontal lines highlight the extension of each radial intervals, while the red segments indicate results from Milone et al. (2017a) and Milone et al. (2020a) based on RGB stars. The vertical dotted and dashed-dotted lines indicate the core and the half-light radius.

The comparison with the results on multiple populations' radial distribution by Bellini et al. (2013) is particularly puzzling. Based on the $m_{\rm F390W}$ vs. $m_{\rm F390W} - m_{\rm F606W}$ CMD, they identified split MS and RGB in NGC 6441, finding that both the blue MS and RGB sequences are more centrally concentrated than the red ones. Specifically, the fraction of blue stars decreases from ∼0.40 at R∼ 0.9 arcmin to ∼0.35 at R∼2.5 arcmin in the MS. The fraction of the blue RGB changes from ∼0.6 around the cluster center to ∼0.5 at R∼2.5 arcmin. The fraction of blue MS and RGB stars is significantly smaller than the fraction of 2G stars inferred in this work, thus indicating that the blue sequences found by Bellini and collaborators enclose only part of the whole 2G population of NGC 6441. This, combined with the different radial range covered by the Bellini et al. (2013) dataset, is likely the reason for the discrepancy between the two works.

Table 2.5: Probability that the observed radial distribution of $N_{\rm 2G}/N_{\rm TOT}$ is produced by a flat distribution.

CLUSTER	p-value	CLUSTER	p-value
NGC 0104	< 0.01	NGC 6496	0.29
NGC 5927	< 0.01	NGC 6624	0.71
NGC 6304	0.99	NGC 6637	0.60
NGC 6352	0.60	NGC 6652	0.96
NGC 6366	0.75	NGC 6838	0.97
NGC 6388	0.87	NGC 1978	0.89
NGC 6441	0.59	NGC 0416	0.02

2.7 Summary and Conclusions

In the work presented in this Chapter, we investigate the phenomenon of multiple populations in the red HB and red clump of 14 GCs thanks to multiband *H*ST and ground-based photometry. This approach allowed us to identify the 1G and 2G stars and characterize the phenomenon, for the first time, homogeneously among an extended sample of clusters in this evolutionary sequence. Notably, our sample includes both Galactic and extragalactic GCs, allowing us to explore the phenomenon in the old Milky Way clusters ($>$11 Gyr) and among younger ones ($\sim$2 and 6 Gyr) in the Magellanic Clouds. For the latter two, we derive high-precision photometry and astrometry by analyzing images taken with the ACS/WFC and WFC3/UVIS cameras onboard *H*ST. We summarize our findings in the following:

- We disentangle 1G and 2G stars in the HB of 12 Milky Way GCs, NGC 416 in the SMC, and NGC 1878 in the LMC. This finding confirms the presence of multiple populations among both Galactic and extragalactic GCs.
- The variety of multiple populations morphology, as detected in the RGB and MS, is still present among red HB stars. In particular, we find differences in the extension of the 1G and 2G sequences, the number of subpopulations, and the relative number of stars in each population.
- We measure the fraction of red HB and red clump 1G stars in all the GCs of our sample. In the Galactic ones, it ranges from $\sim$18% in the massive NGC 6388 ($\sim$1.1$\times$10^6 $\mathcal{M}_\odot$) to $\sim$64% in the least massive GC NGC 6388 ($\sim$4.9$\times$10^4 $\mathcal{M}_\odot$). Noticeably, thanks to the HB stars it was possible to infer for the first time the population ratios in NGC 5927, NGC 6304, and NGC 6441, where the photometry of RGB stars do not provide a clear-cut separation between the 1G and 2G sequences.

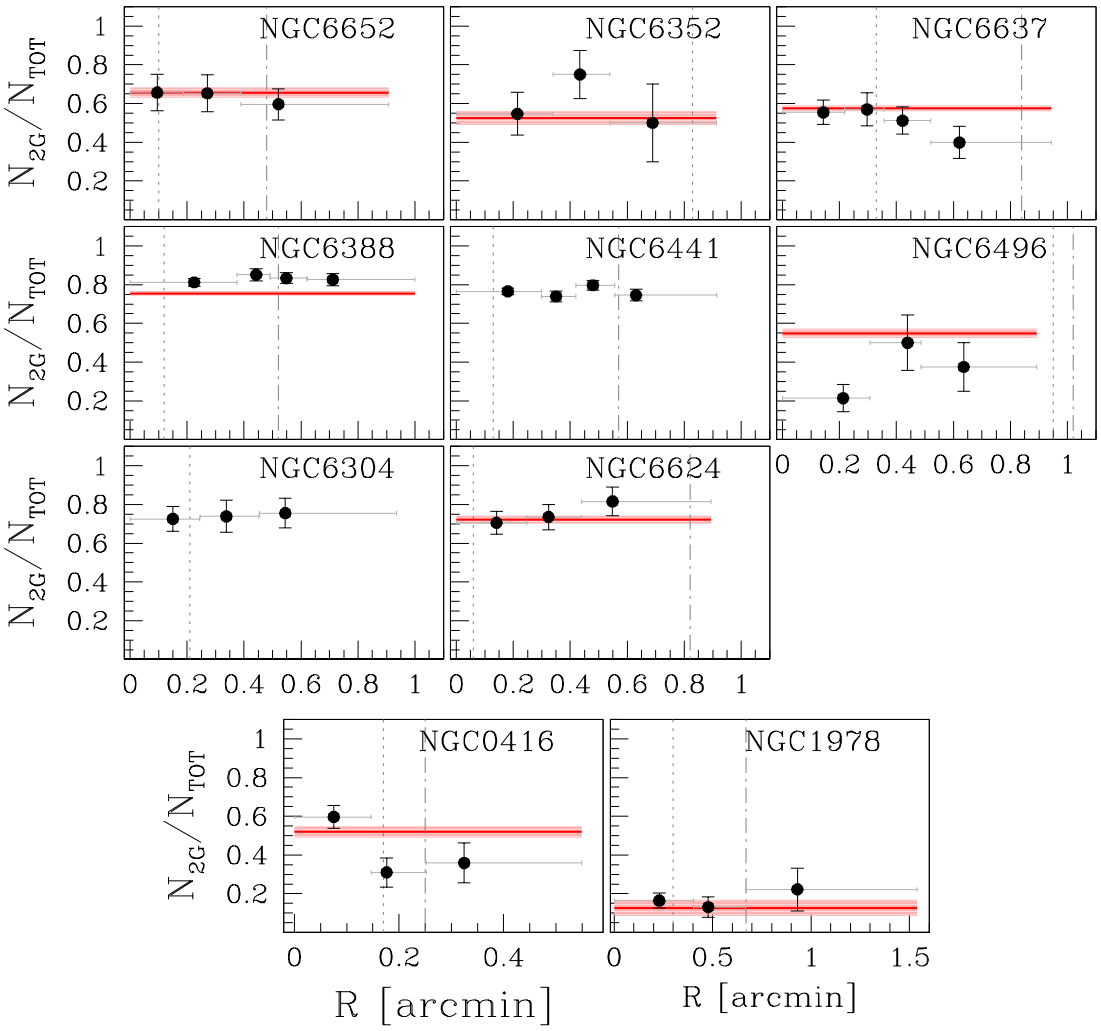

Figure 2.20: Same as Figure 2.19, but for the Galactic GCs NGC 6652, NGC 6352, NGC 6637, NGC 6388, NGC 6441, NGC 6496, NGC 6304, and NGC 6624 and for the MC clusters NGC 416 and NGC 1978.

We combine our findings based on HB stars with previous results from RGB and MS stars -when available- to derive improved population ratio estimates.

- The derived 1G star fraction anticorrelates with the present-day and initial mass of the host cluster, with the most massive GCs having the largest contribution of 2G stars. We confirm this result when combining our measurements from previous studies on RGB and MS stars to extend our sample of GC. Similarly, the $m_{\rm F336W} - m_{\rm F438W}$ extension increases with the cluster mass. These two findings corroborate the idea that the incidence and complexity of multiple populations increase with cluster mass, as also found by Milone et al. (2017a, 2020a). We detect no correlation between the 1G stars fraction and the age of the GCs.

- We combine the results from our *H*ST-based analysis with the catalogs published by Stetson et al. (2019), which cover a wider FoV, to investigate the radial distribution

of multiple populations in the HB up to the outskirts of four GCs in our sample, namely 47 Tuc, NGC 5927, NGC 6366, and NGC 6838. While in the first two, we find that 2G stars are significantly more centrally concentrated than the 1G stars, no radial differences have been detected for the latter two. For the remaining clusters, we limited our radial exploration to the innermost $\sim$2.7$\times$2.7 arcmin^2 covered by the *H*ST cameras, finding no radial differences between 1G and 2G stars distribution, with the only exception of NGC 416, where 2G stars are more centrally-concentrated than the 1G.

- We discover that GCs typically exhibit extended sequences of 1G stars along the red HB, not consistent with them being a single stellar population. NGC 6388 is the most extreme case and intriguingly presents a 1G stellar distribution in the $m_{\rm F275W} - m_{\rm F336W}$ vs. $m_{\rm F336W} - m_{\rm F438W}$ two-color diagram significantly wider that NGC 6441, which has historically considered as its twin cluster. By comparing the observed 1G stars spread with simulated HB photometry, we find that the 1G extension can be reproduced either with a spread in helium or metallicity, with our dataset making us unable to break this degeneracy. Furthermore, the color extension of 1G stars along the red HB and the RGB correlate with each other, thus suggesting that the extended 1G sequence spotted in the two-color diagram is produced by the same physical process that leads to the extended 1G sequence in the ChM of RGB stars (Milone et al., 2017a).

- The fraction of 1G stars inferred in the extragalactic clusters NGC 416 and NGC 1978 value $\sim$0.55 and $\sim$0.85, respectively, which are larger than what was found in Galactic GCs with similar masses. This finding supports the idea that the environment (i.e., the host galaxy) affects the multiple populations' phenomenon and is consistent with a scenario in which 1G stars dominate GCs at their formation. As a cluster evolves, they are stripped due to interaction with the host galaxy. Indeed, the Magellanic Clouds clusters, which are younger than the Milky Way ones, have a larger incidence of 1G stars. Moreover, due to their relatively small masses, the SMC and LMC galaxies would be less efficient than the Milky Way in stripping 1G stars from their GCs.

CHAPTER 3

Multiple Populations among M-dwarf stars with Near-Infrared Photometry

Abstract

In this Chapter, I illustrate the results published in Dondoglio et al. (2022) on multiple populations among very-low-mass (VLM) stars.

We exploit near-Infrared (NIR) *H*ST photometry to explore M-dwarf stars, deriving the CMDs of nine Galactic GCs and the open cluster NGC 6791 in the F110W and F160W bands of HST, showing that the MS stars below the knee are either broadened or split thus providing evidence of multiple populations among very stars. In contrast, the MS of NGC 6791 is consistent with a single population. The color distribution of M-dwarfs dramatically changes between different GCs, and the color width correlates with the cluster mass. We conclude that the multiple-populations ubiquity, variety, and dependence on GC mass are properties common to VLM and more massive stars.

We combine UV, optical, and NIR observations of NGC 2808 and M4 to identify multiple populations along a wide range of stellar masses ($\sim 0.2 - 0.8 \mathcal{M}_{\odot}$) from the MS turn-off to the VLM regime, and measured, for the first time, their mass functions (MFs). We find that the fraction of multiple populations does not vary in this mass range, and that their MFs share the same slopes within uncertainties. These findings indicate that the properties of the phenomenon do not depend on stellar mass. In a scenario where the second generations formed in higher-density environments than the first generations, the possibility that the multiple populations formed with the same initial MF would suggest that it does not depend on the environment.

3.1 Introduction

As explained in Section 1.2, many different scenarios to explain multiple populations have been proposed throughout the years. Agreement on which one of these mechanisms produced what we currently observe in GCs is still far from being reached in the community. To move towards the right direction in unveiling this mystery, gathering new observational information aimed at constraining the different formation scenarios is mandatory. On that note, the Very-Low Mass (VLM) stars can provide unique insights into the multiple populations phenomenon. VLM stars have masses smaller than $\sim$0.4 $\mathcal{M}_{\odot}$, with high density and small $T_{\rm eff}$, characterized by a spectral peak in the near-infrared (NIR), where various molecules including oxygen (e.g., CO, H_2O, OH, TiO, VO, ZrO) are primary source of opacity (e.g., Allard & Hauschildt, 1995). They are among the faintest stars that can be detected in GCs, making their observations particularly challenging. For this reason, while multiple populations have been widely studied among stars more massive than $\sim$0.4 $\mathcal{M}_{\odot}$, this regime, populated by M-dwarf stars, is almost unexplored. Before this study, multiple populations were identified and characterized with photometry in only four clusters, namely NGC 2808, M4, ωCen, and NGC 6752 (Milone et al., 2012d, 2014, 2017b, 2019; Dotter et al., 2015; Bellini et al., 2018) thanks to the NIR camera onboard the *HST*. In particular, the $m_{\rm F110W} - m_{\rm F160W}$ color is sensitive to absorption bands of oxygen-based molecules (mainly H_2O) and, therefore, is an effective tool to disentangle the oxygen-different multiple populations.

Separating chemically-different populations among VLM stars is also crucial to extend the study of their mass function (MFs) to this low mass regime, thus retrieving robust slope estimates based on a large range of stellar masses. The only observational study of the MF of multiple populations in literature has been carried out by Milone et al. (2012a) for three populations with different helium amounts in NGC 2808. No significant slope differences were found between them, although the stars with pristine helium abundance seemed to deviate, flattening below $\sim$0.6 $\mathcal{M}_{\odot}$. However, the dataset used in this pioneering work, based on optical *HST* observations, covered a relatively narrow stellar-mass range, $\sim$0.75-0.45 $\mathcal{M}_{\odot}$, preventing Milone and collaborators from drawing firm conclusions. The natural step further is to extend the sample down to lower stellar masses, such that we can infer the presence (or lack thereof) of a difference between the slope of the multiple populations' MFs.

Determining the MF slopes of multiple populations can provide insights into their formation and dynamic history. A careful interpretation of the present-day MF requires taking into account the possible presence of differences introduced by dynamical processes (like GC mass loss and mass segregation) on the global and local (i.e., measured at a given distance from the cluster center) MF along with those that intrinsic differences in the initial MF (IMF) might introduce. Vesperini et al. (2018), employing N-body simulations, have studied the evolution of the MF in clusters with multiple populations

and explored the extent of expected slope variations arising from the effects of dynamics in different stellar populations starting with the same IMF and those which, instead, formed with different IMFs.

Comparing the characteristics of multiple populations over a wide stellar mass range provides several key constraints of the formation scenarios mechanisms. Indeed, in the scenarios that foresee 2G stars forming from protostars accreting processed material, one may expect that the amount of accreted material, and therefore their chemical composition, would be proportional to the stellar mass. For example, by assuming a Bondi–Hoyle–Littleton accretion, the amount of material accreted goes with the square of the stellar mass, hence less massive stars would accrete a smaller amount of processed material and exhibit smaller internal light-elements variations than more massive ones. A stellar population formed with this mechanism is expected to follow an MF with a slope that values -2 (Ballesteros-Paredes et al., 2015), which, in the low-mass regime, significantly deviates from a Kroupa (2001) IMF.

Driven by these results, we investigate deep NIR *H*ST observations of nine Galactic GCs and one Galactic open cluster to explore their VLM and perform an early census of multiple populations in this mass regime. To our knowledge, these are the clusters for which either proprietary or public-appropriate NIR data are available in the *H*ST archive and are deep enough to reach our goals. In this work, we describe the dataset and present the first collection of homogeneously analyzed NIR CMDs that can highlight multiple populations. Moreover, for two GCs in this sample, namely NGC 2808 and M4, we combine NIR with UV and optical observations to spot multiple populations along the entire MS and derive their MF.

This Chapter is organized as follows: Section 3.2 describes the dataset and summarizes the procedure for data reduction. The NIR CMDs of all the clusters are presented in Section 3.3. In Section 3.4, we present the two GCs where we measure the multiple population MFs, NGC 2808 and M4, introducing the photometric tools that we exploit to separate multiple populations along the MS. Sections 3.5 and 3.6 describe how we derive the MFs of the stellar populations in NGC 2808 and M4, respectively. Section 3.7 explores the radial behavior of the multiple population patterns in both GCs and Section 3.8 discusses and summarizes the results.

3.2 Data and Data Reduction

To investigate the stellar populations among VLM stars, we exploit, for the ten clusters in our sample, exposures in the F110W and F160W filters of the Near Infrared Channel of the Wide Field Camera 3 (NIR/WFC3) onboard *HST*. We also use, when available, optical images collected through the Wide Field Channel of the Advance Camera for Survey (WFC/ACS) at different epochs to derive stellar proper motions, which allows us to separate the bulk of field stars from clusters stars. This was possible for 47 Tuc, NGC 288, NGC 1851, ωCen, NGC 5904, M4, NGC 6656, NGC 6752, and NGC 6791. In addition, we also exploit images taken with the ultraviolet and visual (UVIS) channel of

WFC3 to disentangle the multiple stellar populations among the most massive MS stars in NGC 2808 and M4.

To retrieve the best possible photometry of VLM stars, we analyze FoVs that are shifted from the cluster centers, where the stellar crowding is much less strong than the central regions making these faint stars detectable. The radial distances of these fields range from ∼0.6 arcmin for NGC 6791 to ∼16.7 arcmin in ωCen. For NGC 2808, we analyze three FoVs, namely A, B, and C, located southwest, south, and northeast, respectively. We summarize all the information about the analyzed exposures in Table 3.1.

To derive stellar positions and magnitudes, we perform PSF photometry by using the KS2 software, calibrating and correcting our magnitudes for differential reddening and zero-points variation, following the prescriptions described in Section 2.2.

Proper motions are measured with the procedure introduced by Piotto et al. (2012) and serve as a tool to separate probable field and cluster stars. Briefly, we average together the coordinates of all the exposures and compared the stellar position in different epochs to infer the relative displacement with respect to the bulk of cluster stars. Then, we transform the relative proper motions (in the *H*ST reference frame) to absolute ones thanks to Gaia DR3 (Gaia Collaboration et al., 2021) proper motions. We consider the common stars with the Gaia DR3 catalog and calculate the median difference between relative and absolute motions, adding these quantity to the relative proper motion of each star. Figure 3.1 illustrates an example of the effectiveness of this approach, where we provide the vector-point diagram of proper motions in the FoV of NGC 6656 (panel a)) and the $m_{\rm F160W}$ vs. $m_{\rm F110W} - m_{\rm F160W}$ of probable cluster and field members (panels b) and c), respectively). panel d) shows the differential-reddening map in the FoV of NGC 6656, which is the studied GC with the largest reddening variation. Panels e) and f) compare the CMDs of the upper MS, which is the region where the effects of differential reddening are more evident before and after the differential-reddening correction.

3.2.1 Artificial-star Tests

We exploit artificial star (AS) tests to estimate the photometric errors in all the studied clusters and the completeness level of the photometry of NGC 2808 and M4, which is fundamental in the MF computation.

In a nutshell, AS tests consist of adding into the images sources with known positions and magnitudes and measuring them by repeating the same procedure adopted to real stars. The output positions and magnitude produced are compared to the input ones to evaluate whether the procedure has found the stars and to estimate the accuracy of our photometry and astrometry. To perform AS tests, we generate a catalog of 50,000 stars with fixed positions and magnitudes, set in a way that qualitatively reproduces the distribution along the FoV and on the observed CMDs. We show the input catalog, colored in magenta, in the $m_{\rm F160W}$ vs. $m_{\rm F110W} - m_{\rm F160W}$ CMD (made with instrumental magnitudes) in Figure 3.2.

A star is considered recovered (i.e., passes the AS test) if the difference between the

Table 3.1: Summary of the data used in this work. The table lists, for each cluster, the average NIR FoV coordinate (J2000) and distance from cluster centre (in arcmin), the exposure times, filters and cameras used for each image, and the program.

CLUSTER (RA, Dec)	Distance [arcmin]	N× EXPTIME	FILTER	INSTRUMENT	PROGRAM
NGC 104	5.98	18×149s	F110W	IR/WFC3	11443
(00h:22m:29.60s, −72°:04':05.02")		499s	F110W	IR/WFC3	11926
		42×274s	F160W	IR/WFC3	11443-5
		24×92s+24×352s	F160W	IR/WFC3	11931
		14×92s+6×352s	F160W	IR/WFC3	12352
		14×92s+6×352s	F160W	IR/WFC3	12696
		4×92s+2×352s	F160W	IR/WFC3	13079
		4×92s+2×352s	F160W	IR/WFC3	13563
NGC 288	5.76	15s+3×200s	F606W	WFC/ACS	12193
(00h:52m:22.75s, −26°:36':52.78")		10s+3×150s	F814W	WFC/ACS	12193
		3×142s+5×1202s	F110W	IR/WFC3	16289
		4×142s+2×1202+7×1302s	F160W	IR/WFC3	16289
NGC 1851	3.11	2×357s	F606W	WFC/ACS	10458
(05h:13m:52.92s, −40°:04':27.61")		2×32s+3×899s	F110W	IR/WFC3	16177
		2×32s+99s+3×1599s	F160W	IR/WFC3	16177
NGC 2808 - Field A	5.31	4×50s+2×620s+2×655s	F390W	UVIS/WFC3	11665
(09h:11m:21.48s, −64°:54':48.01")		2×699s	F110W	IR/WFC3	11665
		799s+899s	F160W	IR/WFC3	11665
NGC 2808 - Field B	5.21	4×50s+2×620s+2×655s	F390W	UVIS/WFC3	11665
(09h:11m:56.67s, −64°:56':56.29")		2×699s	F110W	IR/WFC3	11665
		799s+899s	F160W	IR/WFC3	11665
NGC 2808 - Field C	5.48	4×50s+2×620s+2×655s	F390W	UVIS/WFC3	11665
(09h:12m:49.87s, −64°:49':36.02")		2×699s	F110W	IR/WFC3	11665
		799s+899s	F160W	IR/WFC3	11665
NGC 5139	16.72	2×1300s+2×1375s	F606W	WFC/ACS	9444
(13h:25m:36.61s, −47°:39':50.38")		2×1340s+2×1375s	F814W	WFC/ACS	9444
		2×1285s+2×1331s	F606W	WFC/ACS	10101
		4×1331s	F814W	WFC/ACS	10101
		7×142s+14×1302s	F110W	IR/WFC3	14118
		7×142s+14×1302s	F160W	IR/WFC3	14118
NGC 5904	5.70	621s	F475W	WFC/ACS	13297
(15h:18m:56.03s, 02°:03':49.42")		559s	F814W	WFC/ACS	13297
		2×122s+4×1202s	F110W	IR/WFC3	16289
		3×122s+6×1302s	F160W	IR/WFC3	16289
NGC 6121	1.94	4×680s	F275W	UVIS/WFC3	16289
(16h:23m:41.57s, −26°:30':29.43")		4×358s	F336W	UVIS/WFC3	16289
		4×105s	F438W	UVIS/WFC3	16289
		8×652s	F110W	IR/WFC3	12602
		8×652s	F110W	IR/WFC3	14752
		16×652s	F160W	IR/WFC3	12602
NGC 6656	6.19	2×656s	F475W	ACS/WFC	12311
(18h:36m:45.00s, −23°:58':10.02")		2×389s	F814W	ACS/WFC	12311
		32s+3×124s+149s+249s	F110W	IR/WFC3	16177
		2×149s+3×174s+199s+2×249s	F160W	IR/WFC3	16177
NGC 6752	4.89	28×142s+56×1302s	F110W	IR/WFC3	15096
(19h:11m:19.66s, −59°:55':37.45")		17×142s+34×1302s	F160W	IR/WFC3	15096
		28×142s+56×1302s	F110W	IR/WFC3	15491
		12×142s+24×1302s	F160W	IR/WFC3	15491
NGC 6791	0.59	3×39s+2×1142s+3×1185s	F606W	ACS/WFC	9815
(19h:20m:53.95s, 37°:48':09.60")		3×39s+2×1142s+3×1185s	F814W	ACS/WFC	9815
		3×49s+260s+2×399s	F110W	IR/WFC3	11664
		3×49s+260s+2×399s	F160W	IR/WFC3	11664

input and output position and magnitude is less than 0.5 pixel and 0.75 mag, respectively. To these sources, we then apply the selection criteria on the quality parameters provided by the KS2 as in Figure 2.1. Recovered stars that pass our quality criteria are represented

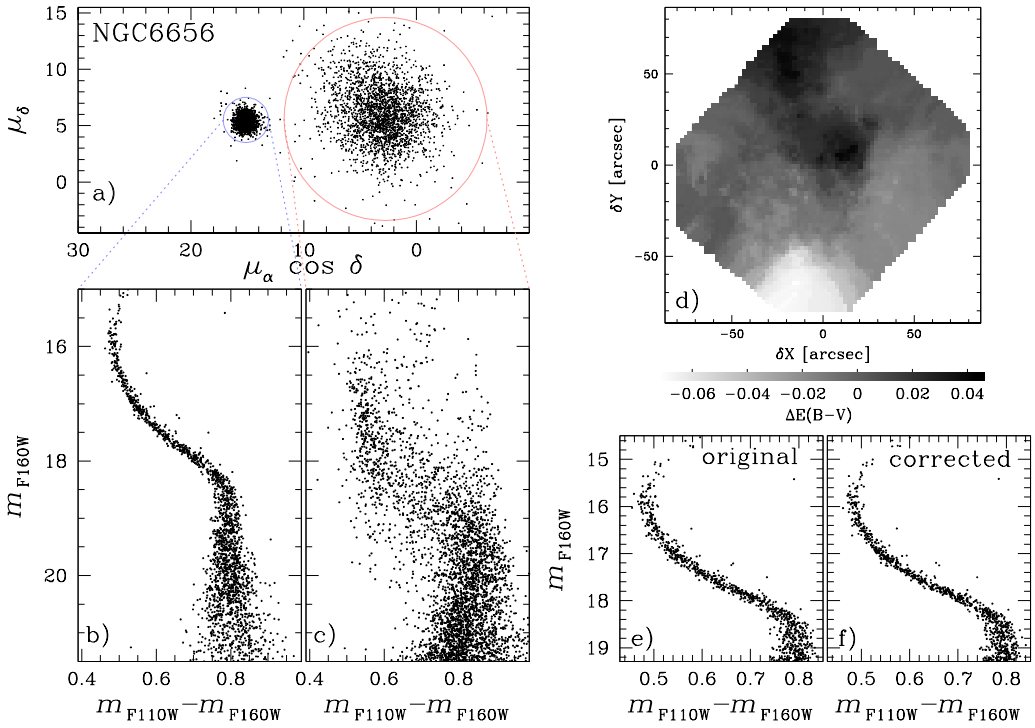

Figure 3.1: This figure illustrates various steps for the determination of differential-reddening corrected photometry of cluster members in NGC 6656. panel a) shows the vector-point diagram of proper motions (in mas/yr) for all stars in the FoV, while panels b) and c) show the $m_{\rm F160W}$ vs. $m_{\rm F110W} - m_{\rm F160W}$ CMDs for proper-motion selected cluster members and field stars, respectively. The map of differential reddening is plotted in panel d), where the levels of gray are proportional to the amount of E(B−V) variation as indicated on the bottom. The comparison between the original CMD and the CMD corrected for differential reddening is provided in panels e) and f), respectively.

as black dots in Figure 3.2. The completeness is given by the fraction of recovered stars over all the input stars in different F160W magnitude bins.

3.3 Near-infrared Color–Magnitude Diagrams

We present the $m_{\rm F160W}$ vs. $m_{\rm F110W} - m_{\rm F160W}$ NIR CMDs obtained after carrying out the data reduction in Figure 3.3 for all the clusters in our sample. At the right of each CMD, we show a zoom of the MS region below the knee (i.e., the saddle ∼2-3 mag fainter than the MS turnoff), which highlights the VLMs stars. Clearly, the color width of these stars in all the nine GCs is broader than what was expected from observational errors only (red error bars), thus proving that the presence of multiple populations is a widespread phenomenon in GCs also among the M-dwarf stars. In contrast, the open cluster NGC 6791 displays a narrow sequence of VLM stars, with a color spread consistent with observational errors, thus showing that, as expected, no multiple populations are

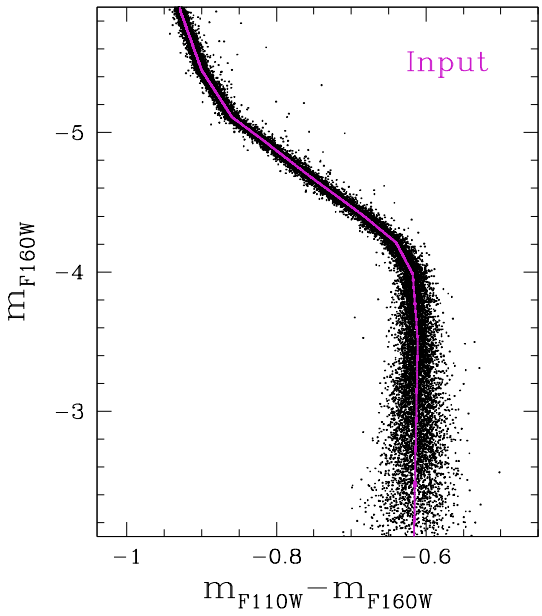

Figure 3.2: Instrumental $m_{\rm F160W}$ vs. $m_{\rm F110W}-m_{\rm F160W}$ CMD of the input catalog for the AS test (magenta line) and the relative output given by the KS2 (see text for details).

present in this cluster.

A visual inspection of our collection of CMDs reveals variability in how the M-dwarf color broadening manifests among different GCs. In NGC 288, NGC 2808, and M4 a bimodal distribution is visible, while NGC 6752 presents a triple MS. On the other hand, in the remaining GCs, we observe a more continuous color distribution. To quantify this visual impression, we select for each cluster the MS stars that lie within an F160W interval between 0.5 and 2.5 mag below the MS knee (measured by Lagioia et al. 2023, in preparation). The corresponding $m_{\rm F160W}$ vs. $m_{\rm F110W}-m_{\rm F160W}$ CMD is then verticalized as in Milone et al. (2017a, see their Section 3.2) to derive the $\Delta_{\rm F110W,F160W}$ pseudo-color. We show the kernel density distribution of this quantity as a solid black line in Figure 3.4, which highlights the diverse morphologies within our sample of clusters. The distribution expected by observational errors only is drawn in orange.

Moreover, the color width changes from one cluster to another. To quantify this impression, we consider M dwarfs in a $\pm$0.2 mag interval located 2 F160W magnitudes below the MS knee. First, we define the observed MS width $W^{\rm obs}_{\rm F110W,F160W}$ as the difference between the 96th and the 4th percentile of the F110W-F160W color distribution of the selected VLM stars. Then, we estimate the intrinsic width $W_{\rm F110W,F160W}$ by subtracting in quadrature the contribution of observational errors from $W^{\rm obs}_{\rm F110W,F160W}$. The error associated with this quantity is derived by bootstrapping with replacements 1,000 times over the sample of M dwarfs and is defined as the standard deviation of the whole bootstrapped measurements.

We find that $W_{\rm F110W,F160W}$ ranges from $\sim$0.06 to 0.15 mag in the nine GCs and is consistent with zero in NGC 6791. As shown in Figure 3.5, $W_{\rm F110W,F160W}$ does not

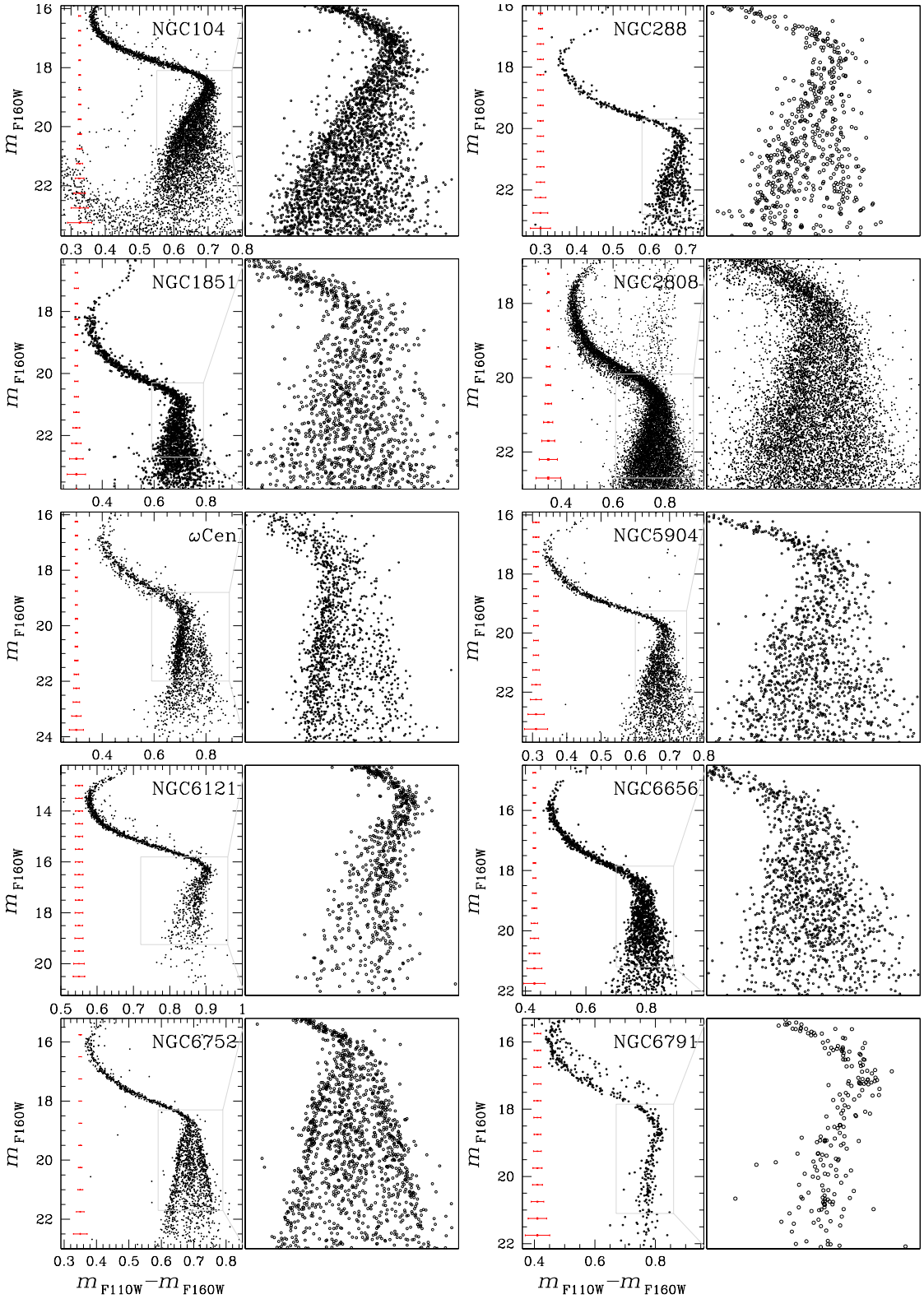

Figure 3.3: Collection of $m_{\rm F160W}$ vs. $m_{\rm F110W} - m_{\rm F160W}$ CMDs for the clusters studied in this paper. We show on the right of each CMD a zoom around the MS knee. Red bars represent the color uncertainties at different $m_{\rm F160W}$ levels.

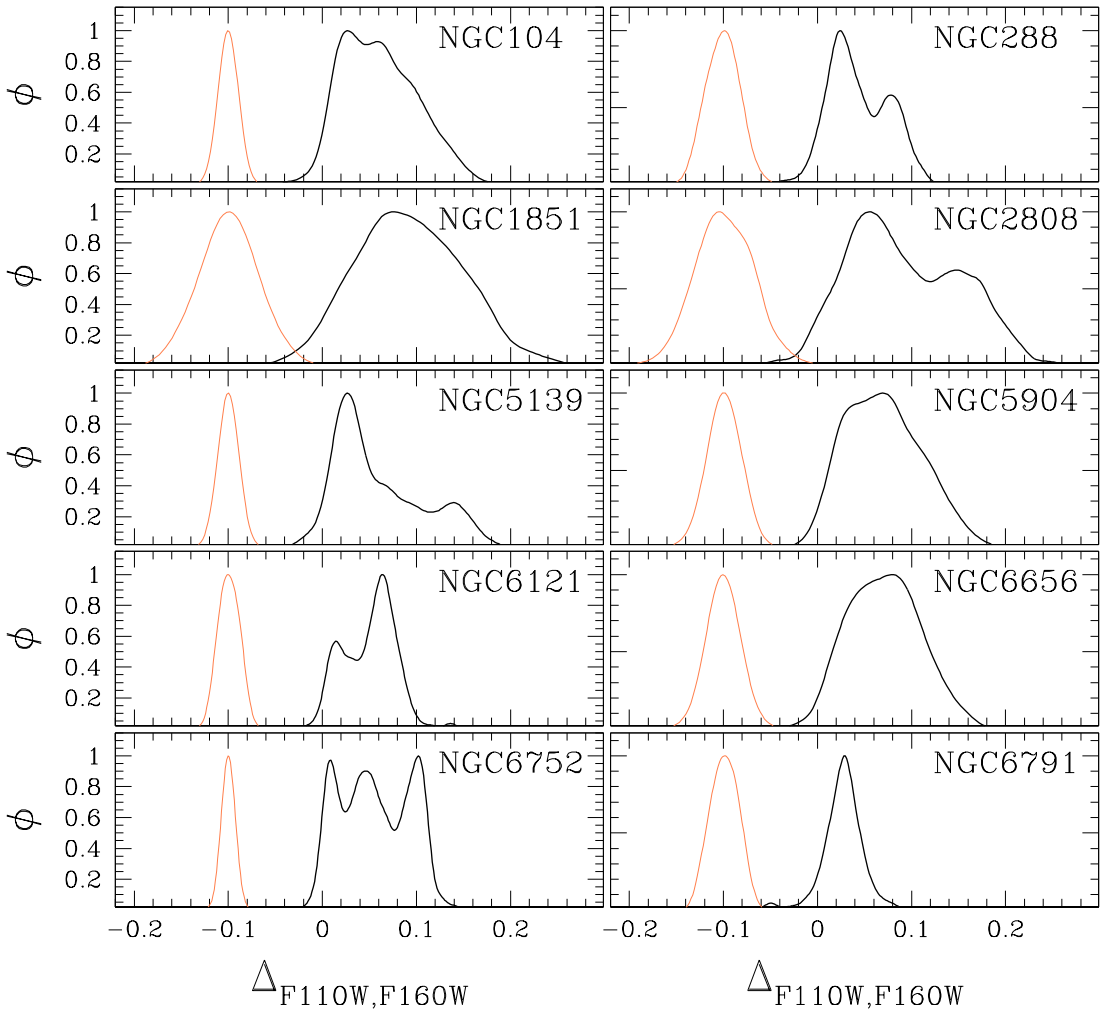

Figure 3.4: $\Delta_{\mathrm{F110W,F160W}}$ kernel-density distributions for M-dwarfs in the F160W magnitude interval between 0.5 and 2.5 mag below the MS knee (black). Orange curves indicate the corresponding distributions of observational errors. For clearness, the error distributions are shifted by -0.1 mag in $\Delta_{\mathrm{F110W,F160W}}$.

correlate with metallicity (taken from Harris, 1996; Villanova et al., 2010), but correlates significantly with cluster mass (from Platais et al., 2011; Baumgardt & Hilker, 2018), and strongly correlates with the oxygen difference between 2G and 1G stars inferred by Marino et al. (2019a) using high-resolution spectroscopy. This latter correlation further supports the effectiveness of the $m_{\mathrm{F110W}} - m_{\mathrm{F160W}}$ color in mapping oxygen variations among VLM stars.

3.4 Multiple Populations in NGC 2808 and M4

Here, we present the two GCs to which we are going to calculate the MF of their multiple populations. Both are widely studied in this context and represent optimal targets for

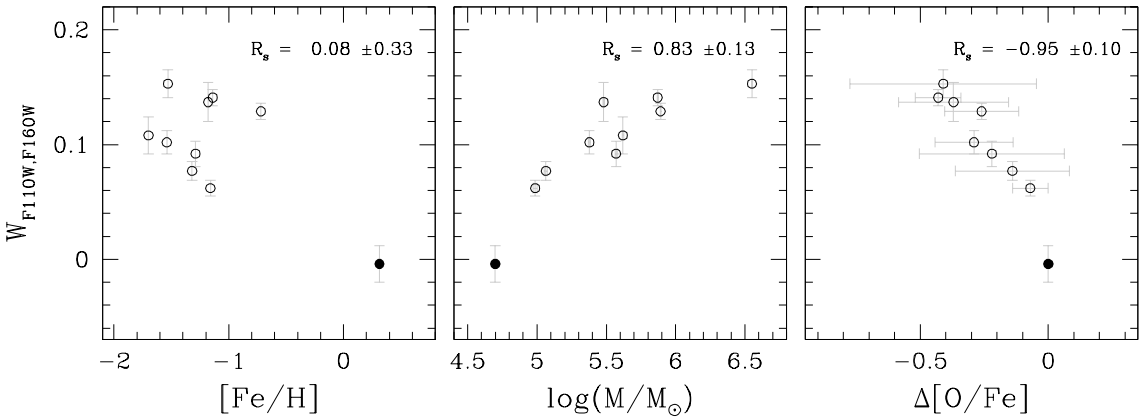

Figure 3.5: The MS width $W_{\rm F110W,F160W}$, is plotted against cluster metallicity (left), logarithm of cluster mass (middle) and average oxygen difference between of 2G and 1G (right). The black dots indicate the NGC 6791 measurements. The Spearman's rank correlation coefficients for GC measurements are reported in each panel.

our goals. We summarize the current knowledge of their multiple population features in the following:

1 NGC 2808 is one of the most complex and unique clusters in the Milky Way, hosting stellar populations with extreme helium abundances, detected by both photometry and spectroscopy (e.g., D'Antona et al., 2005; Piotto et al., 2007; Marino et al., 2014b). Moreover, it is also the first GC in which evidence of multiple populations among VLM stars was found (Milone et al., 2012d). In the RGB, the ChM reveals at least five distinct stellar populations (called A, B, C, D, and E) with different helium abundances: populations A, B, and C exhibit nearly pristine helium contents, while the D and E stellar populations are strongly helium enhanced, having Y∼0.31 and Y∼0.36, respectively (Milone et al., 2015). The helium-rich populations are also the most extreme in terms of light elements such as C, N, O, Na, Mg, Al, Si, and K (see Carretta et al., 2009b, 2018; Carretta, 2015; Mucciarelli et al., 2015; Marino et al., 2017, 2019a; Latour et al., 2019, and references therein, for details on the chemical composition of stellar populations in NGC 2808).

2 M4 is a very different GC, characterized by two stellar populations that differ in C, N, O, Na, and Al (e.g., Marino et al., 2008, 2011b, 2017; Carretta et al., 2009b; Villanova & Geisler, 2011) and have similar helium abundances (e.g., Milone et al., 2018b; Lagioia et al., 2018; Tailo et al., 2019b). The distinct groups of stars have been identified along basically the entire CMD, from the AGB, HB, and RGB stars to the MS and VLM stars (e.g., Marino et al., 2011b; Milone et al., 2014; Marino et al., 2017).

We first derive the Luminosity Functions (LFs) and then the MFs of multiple populations in both clusters over a wide stellar mass range, from the brightest MS stars to the

bottom of the VLM regime[7]. We select these two GCs for three regions. First, as discussed above, their multiple populations have been already well identified and extensively studied in literature both between the MS turnoff and knee (hereafter upper MS) and below the MS knee (hereafter lower MS). Hence, we can spot the same populations and connect them along the whole MS. Second, available archive *HST* observations allow the detection of these populations among both MS regimes in the same FoV, therefore at the same radial distance from the center, which is a crucial requirement to properly compare the phenomenon without introducing any bias related to different radial mapping. Third, the F110W-F160W color distribution of VLM stars in these two clusters is bimodal, thus allowing us to disentangle the chemically different populations in the lower MS and derive their MFs.

For both clusters, we perform AS tests to infer the completeness level in function of the magnitude. All the stars that we consider to measure the LFs and MFs of different populations have a completeness level larger than $\sim$60%.

To identify the multiple stellar populations along the upper MS of NGC 2808, we use the $m_{\rm F160W}$ vs. $m_{\rm F110W} - m_{\rm F160W}$ CMD portrayed in the left panel of Figure 3.6, in which three sequences are separable between $19.0 < m_{\rm F160W} < 20.5$. Regarding M4, we show in the right panel of the Figure the $m_{\rm F438W}$ vs. $C_{\rm F275W,F336W,F438W}$ diagram, where two sequences are visible at $18.2 < m_{\rm F438W} < 20.0$. This diagram, combined with the $m_{\rm F438W}$ vs. $m_{\rm F275W} - m_{\rm F438W}$ CMD, allow us to build a ChM (see Milone et al., 2015, 2017a). Briefly, we obtain this diagram by computing the 4th and the 96th percentile of the $m_{\rm F275W} - m_{\rm F438W}$ color and the $C_{\rm F275W,F336W,F438W}$ pseudo-color distributions of upper MS stars in different 0.2 magnitude-wide bins. These values are then associated with the median of the magnitude in each bin and linearly interpolated to derive the red and blue boundaries for both distributions, thanks to which we obtain the ChM coordinates $\Delta_{\rm F275W,F438W}$ and $\Delta_{\rm CF275W,F336W,F438W}$ by applying the transformations by Milone et al. (2017a, see their Section 3.2). The resulting ChM is presented in the inbox of the right panel of Figure 3.6, and it shows the bulk of the 1G stars (clustered near the origin of the ChM plane) well separated from the blob formed by the 2G stars (clustered at higher $\Delta_{\rm CF275W,F336W,F438W}$).

3.5 Luminosity and Mass Functions of Multiple Populations in NGC 2808

To derive the LFs and the MFs of the different NGC 2808 populations identifiable along the MS, we analyze stars in the upper and lower MS within the $19.0 < m_{\rm F160W} < 20.2$ and $21.0 < m_{\rm F160W} < 22.5$ magnitude intervals, respectively. LFs are obtained by adapting the methods from Milone et al. (2012a) to the two photometric diagrams used to disentangle upper and lower MS populations, as discussed in Section 3.5.1 and 3.5.2.

[7] Due to the small radial sampling of NIR/WFC3, we do not investigate on any radial variation of the MFs inside the FoV. For that, the LFs and MFs of NGC 2808 and M 4 derived in the following Sections are referred to all stars in a given FoV.

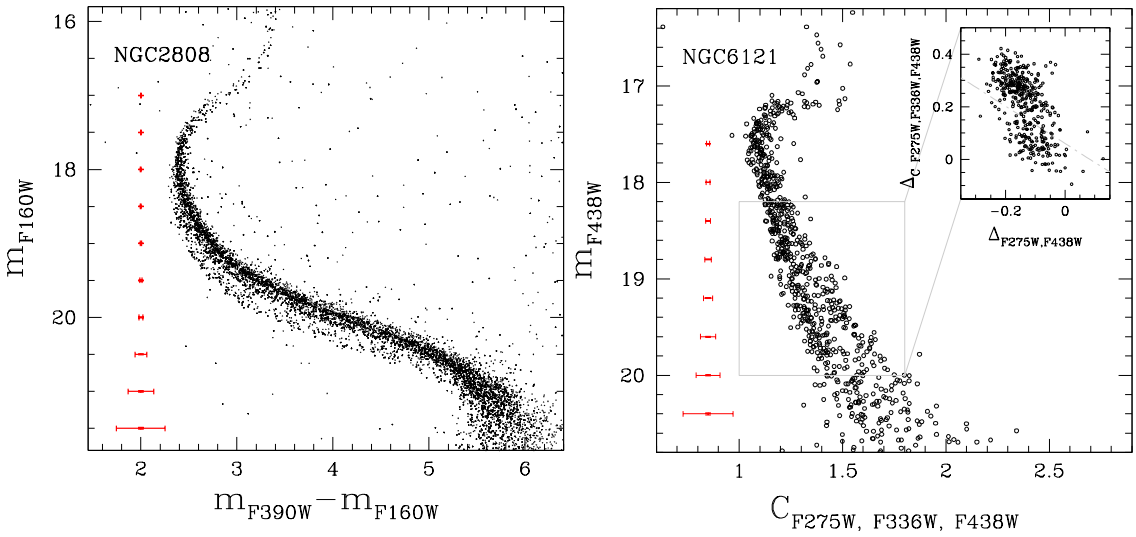

Figure 3.6: $m_{\rm F160W}$ vs. $m_{\rm F390W} - m_{\rm F160W}$ CMD of NGC 2808 (left panel) and $m_{\rm F438W}$ vs. $C_{\rm F275W,F336W,F438W}$ diagram of M 4 (right panel). The inset in the right panel shows the ChM for stars inside the grey box. Red bars indicate the photometric uncertainties at different magnitude levels.

LFs are then converted to MFs by exploiting appropriate mass-luminosity relations, as explained in Section 3.5.3.

3.5.1 Luminosity Functions of Multiple Populations along the Upper MS

To compute the LFs in the upper MS of NGC 2808 we use, as shown in Section 3.4, the $m_{\rm F160W}$ vs. $m_{\rm F390W} - m_{\rm F160W}$ CMD, in which we can clearly spot the three helium-different populations, with Y$\sim$0.25, 0.31, and 0.36, that we dub as red, middle, and blue MS (rMS, mMS, and bMS), respectively. In the following, we extend the procedure presented in Milone et al. (2012a) for these three sequences in the F475W and F814W filters to our F390W and F160W photometry, which is summarized in Figure 3.7.

1 The first step consists of deriving the fiducial lines of the three MSs. We show in panel a) the result for the rMS. To do that, we derive a first guess fiducial line by hand and calculate the color residual $\Delta(m_{\rm F390W} - m_{\rm F160W})$, defined as the color difference between each star and the first-guess fiducial line at the same F160W magnitude. The verticalized $m_{\rm F160W}$ vs. $\Delta(m_{\rm F390W} - m_{\rm F160W})$ diagram is presented in panel b) and is used to derive the $\Delta(m_{\rm F390W} - m_{\rm F160W})$ histogram distribution (panel c)) of upper MS stars in 0.3 mag bin. In each histogram, three peaks are visible, corresponding to the three populations. We show in red the best-fit Gaussian function of the rMS peak. Finally, we associate each Gaussian center with the average stellar magnitude in each bin and linearly interpolated these points to derive the final and improved rMS fiducial line. The procedure is then repeated for mMS and bMS stars.

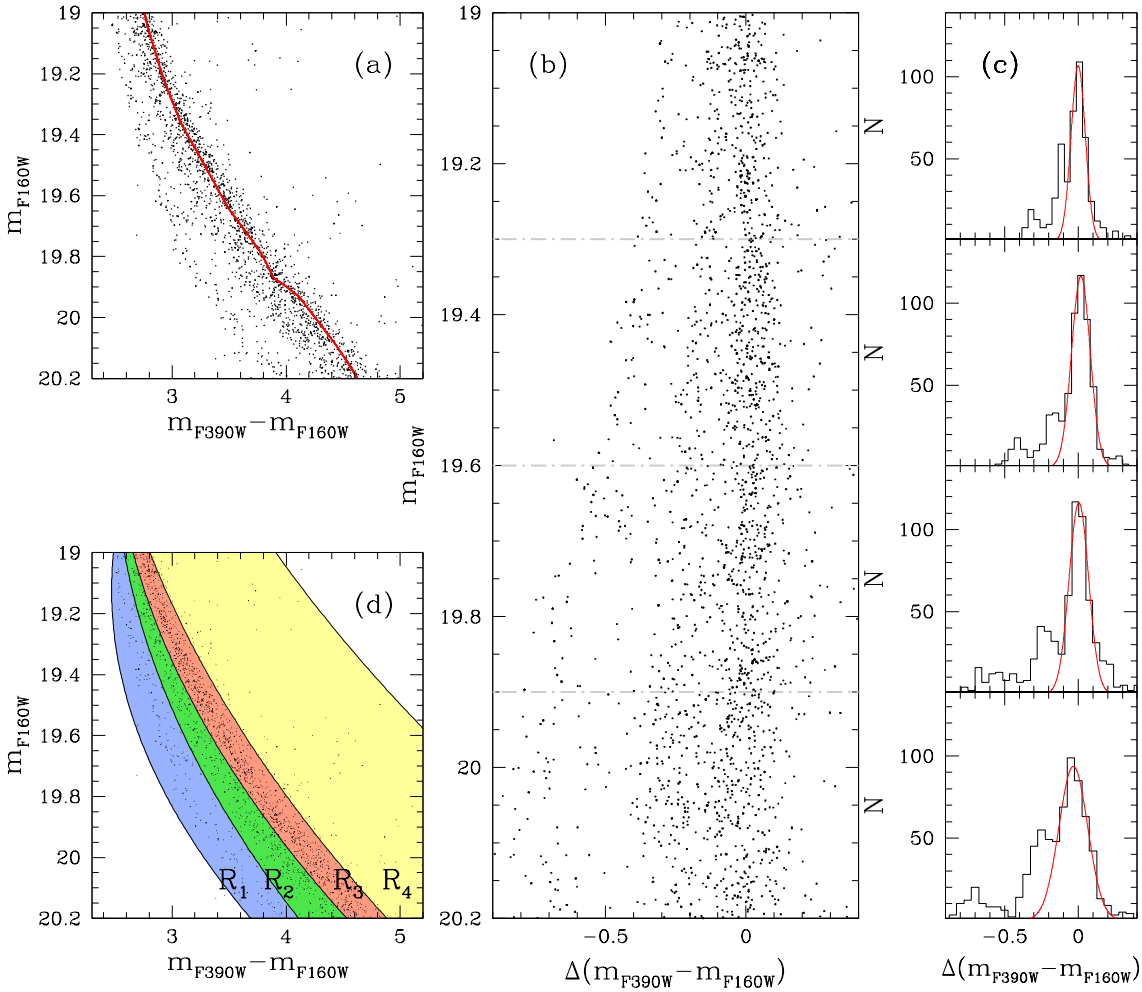

Figure 3.7: *Panel a):* $m_{\rm F160W}$ vs. $m_{\rm F390W} - m_{\rm F160W}$ CMD of all stars in the three fields of NGC 2808. The red line shows the first-guess fiducial line of the rMS. *Panel b):* $m_{\rm F160W}$ vs. $\Delta(m_{\rm F390W} - m_{\rm F160W})$ verticalized diagram obtained from the rMS fiducial line (see text for details). *Panel c):* histogram distribution of $\Delta(m_{\rm F390W} - m_{\rm F160W})$ in four different magnitude bins. The red lines represent the best-fit Gaussian functions of the rMS stars. *Panel d):* R_1, R_2, R_3 and R_4 regions in the $m_{\rm F160W}$ vs. $m_{\rm F390W} - m_{\rm F160W}$ CMD, colored in blue, green, red, and yellow, respectively.

2 We define four regions in the CMD, which we call R_1, R_2, R_3, and R_4 by shifting the three fiducial lines to include the bulk of rMS, mMS, and bMS stars in regions R_1, R_2, and R_3, and binary stars within R_4. The regions are marked with different colors in the CMD presented in panel d) of Figure 3.7. Region R_1 boundaries are obtained by subtracting and adding to the bMS fiducial line $3\times\sigma_{\rm bMS}$, while the blue and red boundaries of R_3 are similarly derived by blue-shifting by $1\times\sigma_{\rm rMS}$ and red-shifting by $3\times\sigma_{\rm rMS}$ the rMS fiducial line. Here, $\sigma_{\rm bMS}$ and $\sigma_{\rm rMS}$ are the color dispersion of bMS and rMS stars, respectively, and are derived from the best-fit Gaussian functions obtained in different magnitudes bin in panel c). Finally, region

R_2 is defined as the region between R_1 and R_3, whereas R_4 includes the CMD area between the red boundary of R_3 and the equal-mass rMS-rMS binaries red-shifted by $3\times\sigma_{\rm rMS}$.

3 The last step consists of deriving each population number of stars at different magnitude bins. To maximize the number of stars (and hence having better statistics), we combine stars in fields A, B, and C (defined in Section 3.2) to compute the fiducial lines and the regions. On the contrary, the LFs have been derived separately for each of the three FoVs. Due to photometric uncertainties, each region is not populated by just the populations of interest but experiences contamination from stars belonging to the other MSs. To account for this effect and derive the correct number of stars, we use the following equation, in which the number of stars $N_{\rm i}$ that falls inside the region $R_{\rm i}$ is

$$\mathbf{N}_{\rm i} = N_{\rm bMS} f_{\rm i}^{\rm bMS} + N_{\rm mMS} f_{\rm i}^{\rm mMS} + N_{\rm rMS} f_{\rm i}^{\rm rMS} + f^{\rm BIN} N_{\rm MS} f_{\rm i}^{\rm BIN} \tag{3.1}$$

where $N_{\rm bMS}$, $N_{\rm mMS}$, and $N_{\rm rMS}$ are the corrected number of stars of each population, $N_{\rm MS}$ their sum, and $f_{\rm i}^{\rm bMS}$, $f_{\rm i}^{\rm mMS}$, and $f_{\rm i}^{\rm rMS}$ the fraction of stars of the three MSs that fall in the i-th region. The last term in the equation accounts for the binaries' contribution. In particular, $f_{\rm i}^{\rm BIN}$ is the fraction of binary stars in the ith region, and $f^{\rm BIN}$ is the total binary fraction. Having four regions, we need to solve a system of four equations to derive the actual number of stars in each of the three populations and of binary stars.

$f_{\rm i}^{\rm bMS}$, $f_{\rm i}^{\rm mMS}$, and $f_{\rm i}^{\rm rMS}$ are inferred from simulated CMDs obtained by performing AS tests (see Section 3.2.1). We build input catalogs of 40,000 ASs for each population, disposed along the corresponding fiducial lines. $f_{\rm i}^{\rm BIN}$ are calculated as the fraction of binary stars in the corresponding region. The degeneracy between the LFs and the fraction of binaries provides the main challenge to estimate $f_{\rm i}^{\rm BIN}$. To break this degeneracy, we adopt the following iterative procedure. At the first iteration, we fix $f^{\rm BIN} = 0$ and solved the system of equations 3.1, thus finding first estimates of $N_{\rm bMS}$, $N_{\rm mMS}$ and $N_{\rm rMS}$. Then, we simulate a CMD composed of MS-MS binaries alone under the assumption that each population hosts the same binary fraction. We adopt a flat mass-ratio distribution for binaries and enhanced by ten times the numbers of bMS-bMS, mMS-mMS, and rMS-rMS binaries to increase the statistics. The resulting CMD has been used to improve the estimates of $f_{\rm i}^{\rm BIN}$. The last step of the first iteration consists in solving equations 3.1 and deriving $N_{\rm bMS}$, $N_{\rm mMS}$, $N_{\rm rMS}$ and $f^{\rm BIN}$.

The subsequent iterations exploit the estimates of $N_{\rm bMS}$, $N_{\rm mMS}$ and $N_{\rm rMS}$ as input to generate a binaries-only CMD to improve the values of $f_{\rm i}^{\rm BIN}$, and then solving the system of equations 3.1. We repeat this step until the $f^{\rm BIN}$ value changed by less than 0.001 between two subsequent iterations. As a result, the total binary fraction obtained in fields A, B, and C values 0.033 ± 0.020, 0.064 ± 0.035, and 0.082 ± 0.036, respectively.

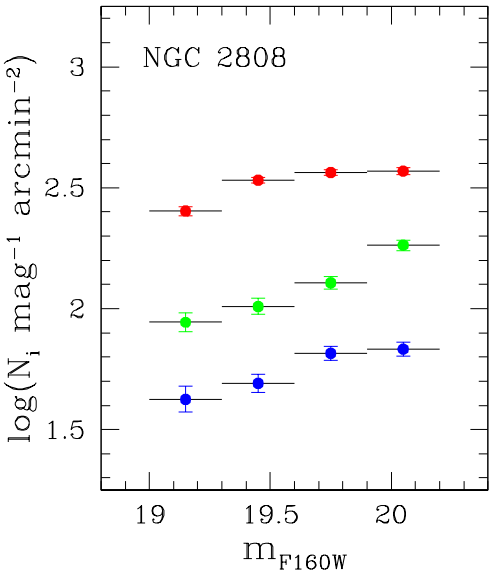

Figure 3.8: Luminosity functions of the three MSs of all stars in NGC 2808. Red, green and blue dots represent rMS, mMS and bMS stars, respectively.

The number of stars in the different magnitude bins, corrected for completeness, provides the LFs of the three populations. Noticeably, the star counts are provided in units of magnitude and area to remove the dependence from the bin size and the area of the analyzed FoV. The LFs of the three populations in the upper MS of NGC 2808 are represented, for the three fields combined, in Figure 3.8.

3.5.2 Luminosity Functions of Multiple Populations along the Lower MS

In the lower MS of NGC 2808, we exploit the $m_{\rm F160W}$ vs. $m_{\rm F110W} - m_{\rm F160W}$ CMD to measure the LFs of its multiple populations. As proven by Milone et al. (2012d), the MS with the blue $m_{\rm F110W} - m_{\rm F160W}$ color, hereafter MS-I, is the counterpart of the rMS, while the mMS and bMS merge in one below the knee, forming the red sequence in the VLM regime (hereafter MS-II). Indeed, helium in NGC 2808 dominates the color position of upper MS stars, making a star hotter (hence bluer) when is more abundant. Moving towards the lower MS, two main mechanisms dominate: the increase in radiative opacity and the collision-induced absorption (CIA) of the H_2 molecule, which make stars redder and bluer, respectively. By further decreasing the stellar mass, the CIA dominates in MS-I, making it bluer. On the other hand, the larger helium amount of the MS-II would make it bluer than MS-I, but its lower H content leads to a drop in the CIA contribution, hence the increase of opacity dominates and its color becomes redder. In NGC 2808 VLM regime, these two effects almost compensate, making the F110W-F160W color unaffected by helium variations, while it is sensitive to oxygen thanks to the F160W band. Since MS-I stars are oxygen-enriched with respect to MS-II stars,

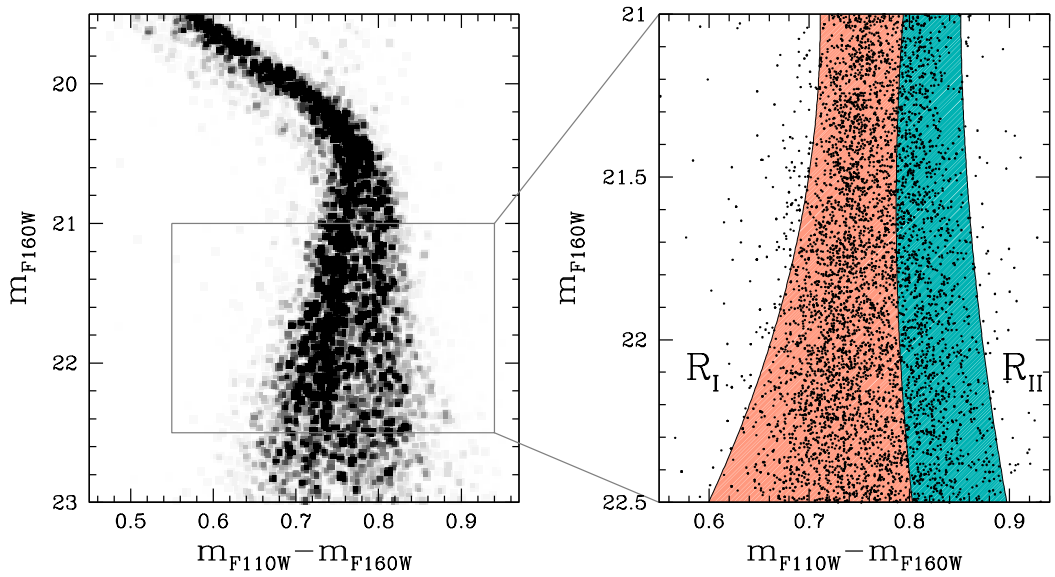

Figure 3.9: *Left panel:* Hess diagram of the $m_{\rm F160W}$ vs. $m_{\rm F110W} - m_{\rm F160W}$ CMD for all the stars in NGC 2808. *Right panel:* CMD of stars inside the black box. Black lines show the boundaries of regions $R_{\rm I}$ and $R_{\rm II}$, colored in red and azure, respectively.

they have fainter $m_{\rm F160W}$ and, as a consequence, bluer $m_{\rm F110W} - m_{\rm F160W}$. With the current available observation, it is impossible to disentangle mMS and bMS below the knee, therefore we can compute the LFs and the MFs over the whole MS only for MS-I and MS-II and their upper MS counterparts.

To derive the LFs of MS-I and MS-II stars, we adapt the procedure described in Section 3.5.1 to the NIR CMD in the $21.0 < m_{\rm F160W} < 22.5$ region, which is highlighted by the gray box in the Hess diagram illustrated in the left panel of Figure 3.9. In the right panels, we show a zoom of the region of interest where we color in red and azure the two areas that encapsulate the bulk of MS-I and MS-II stars ($R_{\rm I}$ and $R_{\rm II}$), respectively. $R_{\rm I}$ is delimited by the fiducial of the MS-I shifted by $2\times\sigma_{\rm MS-I}$ to the blue and by $1\times\sigma_{\rm MS-I}$ to the red (black lines), while the red boundary of $R_{\rm II}$ corresponds to the MS-II fiducial line redshifted by $2\times\sigma_{\rm MS-II}$. The quantities $\sigma_{\rm MS-I}$ and $\sigma_{\rm MS-II}$ represent the color dispersion of MS-I and MS-II stars, respectively, and are derived as in Section 3.5.1.

Since in this mass range the two MSs run almost vertically on the NIR CMD, binary stars are nearly mixed with single stars. For that, we do not account for the binary contribution in deriving the numbers of MS-I and MS-II stars in 0.3-wide F160W magnitude intervals, and we therefore solve the following equations:

$$N_{\rm i} = N_{\rm MS-I} f_{\rm i}^{\rm MS-I} + N_{\rm MS-II} f_{\rm i}^{\rm MS-II}, \tag{3.2}$$

where $N_{\rm i}$ is the number of stars in the i-th region, $N_{\rm MS-I}$ and $N_{\rm MS-II}$ are the numbers of MS-I and MS-II stars, respectively, and $f_{\rm i}^{\rm MS-I}$ and $f_{\rm i}^{\rm MS-II}$ are the fraction of stars of each population that fall into $R_{\rm i}$ and are corrected by contamination utilizing AS tests

as in Section 3.5.1.

The LF of MS-I and MS-II in the A, B, and C FoVs are illustrated in the upper panels of Figure 3.10. They show similar shapes, with the number of stars by unit of area and magnitude bin increasing towards fainter $m_{\rm F160W}$. At $m_{\rm F160W}$ $\sim$20.2 mag, the MS-I shows a slight flattening, but it starts again to get steeper in the low-MS regime. In the middle panels, we display the population ratios in each magnitude bin. Then, we combine the results from the three fields to retrieve the LFs and population ratios for all stars in our NGC 2808 FoVs in the bottom panels of Figure 3.10. We fit the population ratios by means of least squares with a straight line, represented by the gray dot-dashed line. Their slopes, reported in each plot, are consistent with a null value, hence in agreement with a flat dependence on the magnitude. Black bars represent the range of each magnitude bin within which the LF points and the population ratios have been measured. Furthermore, we perform a *p*-value test to evaluate the statistical significance of the observed flat distribution of the MS-I and MS-II fraction, by testing the probability of the null hypothesis, i.e. of an intrinsically flat radial distribution, with the procedure introduced in Chapter 2 (Section 2.9). We find *p*-values of 0.80, 0.15, 0.71, and 0.91 for fields A, B, and C, and their combinations, respectively, confirming the significance of the observed flatness.

Finally, we find that the weighted average fraction of MS-I and MS-II stars, considering both the upper and lower MSs, are 0.67$\pm$0.04 and 0.33$\pm$0.04, respectively.

3.5.3 Mass Functions of Multiple Populations

To measure the MFs, we need to convert magnitudes into masses. For that, we use the magnitude-mass relations provided by the Dartmouth Stellar Evolution Database (Dotter et al., 2008) which best fit the observed CMDs, corresponding to a stellar model with age 11.5 Gyr (Milone et al., 2014), [Fe/H] =-1.14 (Harris, 1996, 2010 edition), and [α/Fe] = 0.4 (Dotter et al., 2010).

Different helium abundances between the three upper MSs of NGC 2808 imply that they do not follow the same mass-luminosity relations. Specifically, we adopt Y = 0.272, 0.336, and 0.386 for the rMS, mMS, and bMS, respectively, which are based on the results obtained by Milone et al. (2015), who inferred their helium content by exploiting RGB stars. The left panel of Figure 3.11 portrays the resulting MFs of the three upper MS populations, where we plot the logarithm of the number of rMS, mMS, and bMS stars in each magnitude bin normalized per unit mass and unit area against the logarithm of the stellar mass. The small number of stars, especially in the bMS, and more importantly the very narrow range of masses (around 0.1 $\mathcal{M}_{\odot}$) covered by these data do not allow us a meaningful estimate of the slopes of the MFs.

To investigate a larger range of stellar mass, we analyze the MFs of MS-I and MS-II, allowing us to reach the VLM regime, as shown in the upper-right panel of Figure 3.11. By least-square-fitting the two MFs with straight lines, we compute their slopes and found that the MFs of MS-I and MS-II stars have slopes consistent at a 1-σ level. In

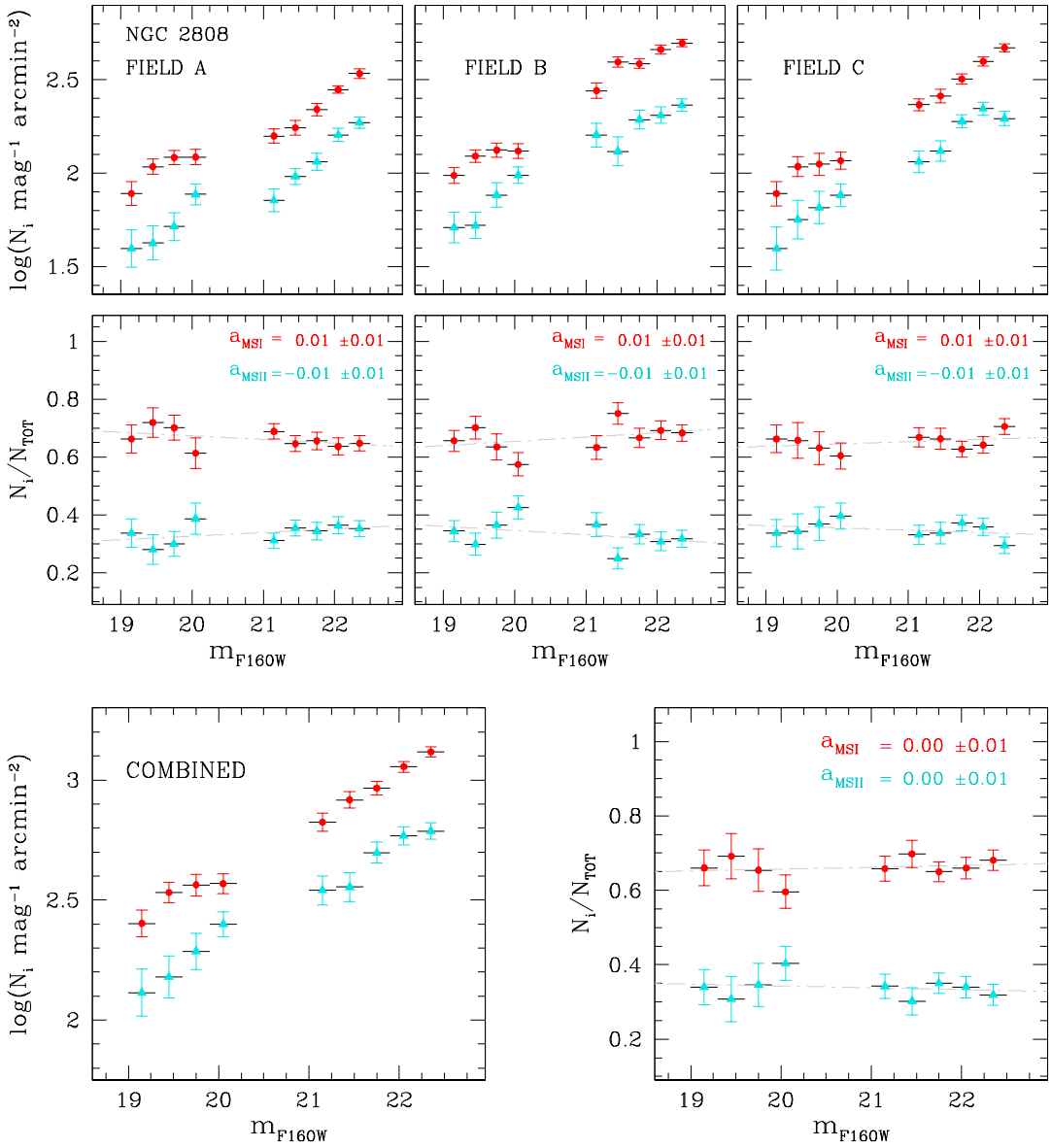

Figure 3.10: *Upper and middle panels:* LFs and populations ratios of NGC 2808 MS-I and MS-II stars (red and cyan dots) in Field A, B, and C. *Lower panels:* LFs and population ratios of multiple populations in NGC 2808 from all the field. The black horizontal bars associated with each point represent the amplitude of the corresponding magnitude bin. The grey dot-dashed lines are the best-fit straight lines and their slopes are reported in the diagrams.

the lower-right panel, we display the population ratios of MS-I and MS-II stars in terms of the stellar mass, which shows, similarly to what was observed when compared to the F160W magnitude, a flat trend, with slopes consistent with zero and a 0.84 *p*-value. Their average fractions are 0.65±0.03 and 0.35±0.03, consistent with the results inferred from the LFs.

We derive the MFs by considering equal-width mass bins. As pointed out by Maíz

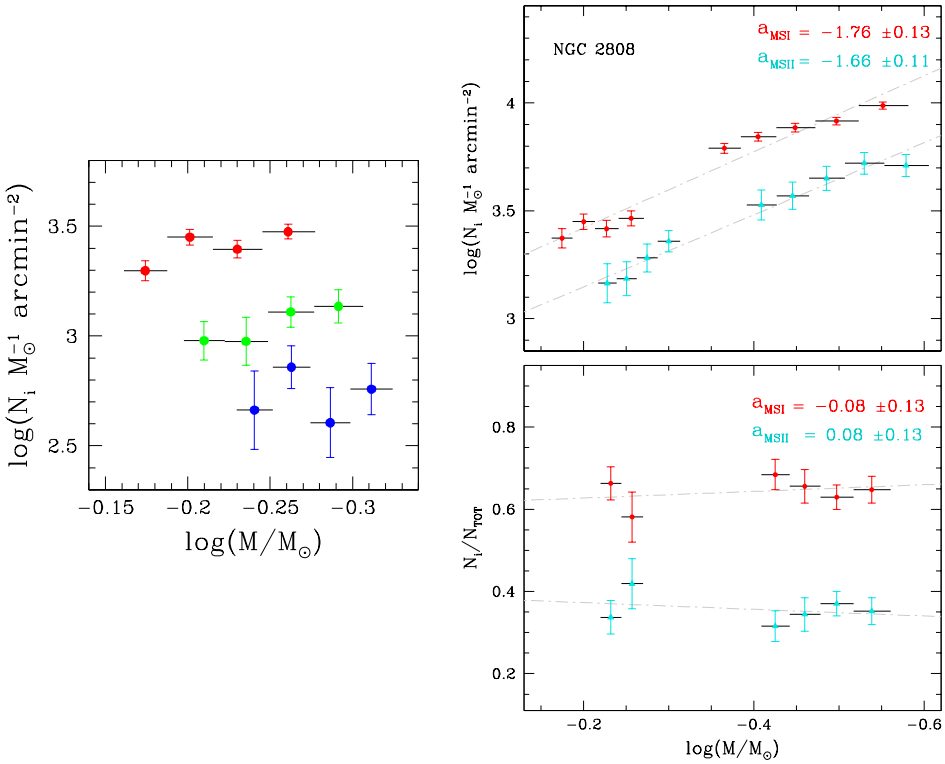

Figure 3.11: *Left panel:* Mass functions of red MS (red), middle MS (green) and blue MS (blue) of the upper MS stars of NGC 2808. *Left panels:* MFs (top) and populations ratios (bottom) of MS-I and MS-II populations (red and cyan dots) for all NGC 2808 stars. Best-fit lines are represented with grey dot-dashed lines and their slopes are reported in the diagram. Black bars illustrate the mass extension of each bin.

Apellániz & Úbeda (2005), this approach could, in principle, introduce some bias in the derivation of the MS slope, especially when the number of stars between different bins varies consistently. To investigate whether our results are affected by this systematic, we repeat the MF derivation considering equal-number-of-stars bins. The resulting slopes, -1.81±0.05 for the MS-I and -1.70±0.15 for the MS-II, are in agreement with what is inferred starting from equal-width intervals, thus proving that different bins assumptions do not have a meaningful impact of our slopes measurements.

3.6 Luminosity and Mass Functions of Multiple Populations in M4

M4 hosts two stellar populations, which are the field-like 1G and the 2G stars, characterized by peculiar light-elements abundances. These populations were spotted along both the upper and lower MS (e.g., Milone et al., 2014, 2020b). We identify them in our FoV by exploiting the ChM made with UV and optical filters and the $m_{\rm F160W}$ vs. $m_{\rm F110W} - m_{\rm F160W}$ NIR CMD for the upper and lower MS stars, respectively (see

Section 3.4). In this Section, we describe the procedure adopted to derive the LFs and the MFs of 1G and 2G stars.

3.6.1 Upper Main Sequence

We consider stars within the $14.4 < m_{\rm F160W} < 16.2$ interval, where the 1G and 2G stars are well distinguishable in the ChM, and we exclude from the analysis the binaries with high mass ratio ($q > 0.2$). To derive the LF, we applied a procedure similar to what was done in NGC 2808 but adapted for the ChM (see also Zennaro et al., 2019). Briefly, we start by identifying a sample of bona fide 1G and 2G stars, defined as the ones with $\Delta_{\rm CF275W,F336W,F438W}$ smaller and larger than 0.155, respectively. Then, we compute the median ChM coordinates of these two groups of stars and used them as the center of elliptical regions with axes equal to photometric uncertainties. These regions, that we call R_1 and R_2, are drawn to encapsulate the bulk of 1G and 2G stars, respectively, and are colored in blue and azure in Figure 3.12.

We divide the magnitude range in 0.6-wide $m_{\rm F160W}$ bins and adapted the equations 3.1 to a diagram with two regions only:

$$N_{\rm i} = N_{\rm 1G} f_{\rm i}^{\rm 1G} + N_{\rm 2G} f_{\rm i}^{\rm 2G}. \tag{3.3}$$

As in previous equations, $N_{\rm i}$ represents the number of stars counted within $R_{\rm i}$, $N_{\rm 1G}$ and $N_{\rm 2G}$ the number of 1G and 2G stars, and $f_{\rm i}^{\rm 1G}$ and $f_{\rm i}^{\rm 2G}$ the fraction of stars from the two populations that fall into $R_{\rm i}$.

Similarly to what was done in the upper MS of NGC 2808, we infer $f_{\rm i}^{\rm 1G}$ and $f_{\rm i}^{\rm 2G}$ through AS tests, simulating 40,000 1G and 2G stars and then measuring the fraction of recovered output stars that fall in each region. Finally, we solve the system of equations 3.3 to derive $N_{\rm 1G}$ and $N_{\rm 2G}$. The fraction that we find does not vary significantly within uncertainties, with average values 0.35$\pm$0.03 and 0.65$\pm$0.03 for 1G and 2G stars, respectively.

3.6.2 Lower Main Sequence

In the lower MS of M4, the LF is measured thanks to the $m_{\rm F160W}$ vs. $m_{\rm F110W} - m_{\rm F160W}$ CMD, following the same procedure introduced in Section 3.5.2. A bifurcation among VLM stars is visible between $16.6 < m_{\rm F160W} < 20.0$, with the 1G and 2G stars forming two separate sequences.

In Figure 3.13, we present the LF of 1G and 2G stars in the upper-left panel, where each point is normalized by unit area and magnitude bin. For both populations, the LF increases when moving from $m_{\rm F160W}$ $\sim$14.5 to $\sim$16.0 and then decreases from $m_{\rm F160W}$ $\sim$17.8 to $\sim$19.8, in contrast with the LFs of NGC 2808. Regarding the population ratios (lower-left panel), no variations have been observed, as confirmed by a p-value of 0.98 and a slope of the trend of the ratio consistent with zero, similar to what detected in NGC 2808.

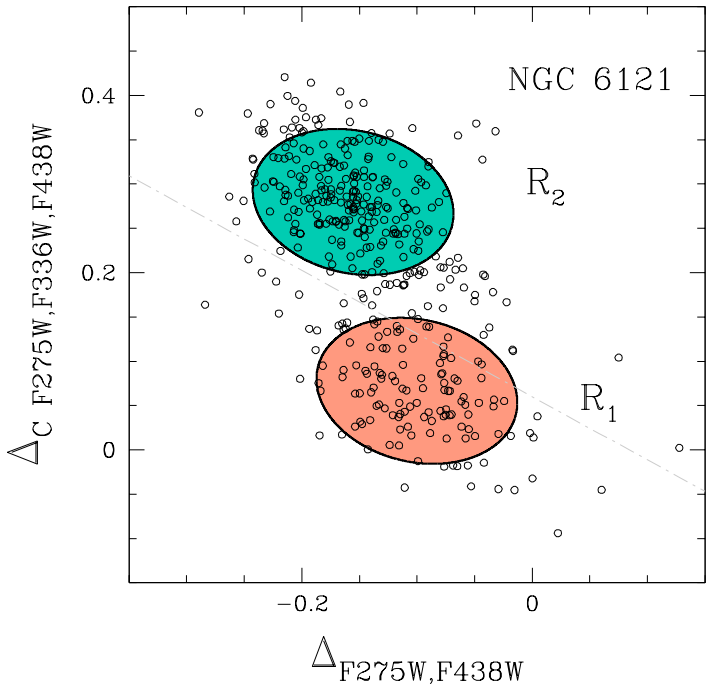

Figure 3.12: Reproduction of the ChM of M 4 displayed in Figure 3.6. The R_1 and R_2 regions are colored in red and blue, respectively (see text for details).

The weighted average of the fraction of 1G and 2G stars inferred in each bin of both the upper and lower MS are 0.36±0.02 and 0.64±0.02, respectively.

3.6.3 Mass Functions of Multiple Populations in M4

To convert the LFs into MFs, we use the same dataset and stellar models of Section 3.5.3, this time with an age of 12.50 Gyr (as estimated by Dotter et al. 2010), [Fe/H] $= -$ 1.16 (Harris, 1996, 2010 edition), and [α/Fe] $= 0.4$ (Dotter et al., 2010)). The helium difference between M4 populations is very small (ΔY ∼0.01, Tailo et al. 2019b), and since such variation does not significantly impact the mass-luminosity relation, we assume a primordial Y =0.246 for all stars. In the upper-right panel of Figure 3.13, we show the MFs of 1G and 2G stars in red and azure, respectively. Both populations share the same MF slope within observational errors, in analogy with what we observed in NGC 2808. As a consequence, the 1G and 2G star fractions do not vary with the stellar mass (p-value of 0.97), as portrayed in the lower-right panel.

Again, we test the derived MFs for possible bias introduced by the different number of stars among the bins by exploiting equal-number mass bins. In this case, the slope values 1.24±0.29 and 1.11±0.39 for 1G and 2G stars, respectively, which are consistent with the results displayed in Figure 3.13, thus proving that our MFs are not significantly affected by the binning strategy.

Although this work focuses on the multiple populations within each GC, it is worth mentioning that the MFs of NGC 2808 and M4 populations behave differently. Indeed, in

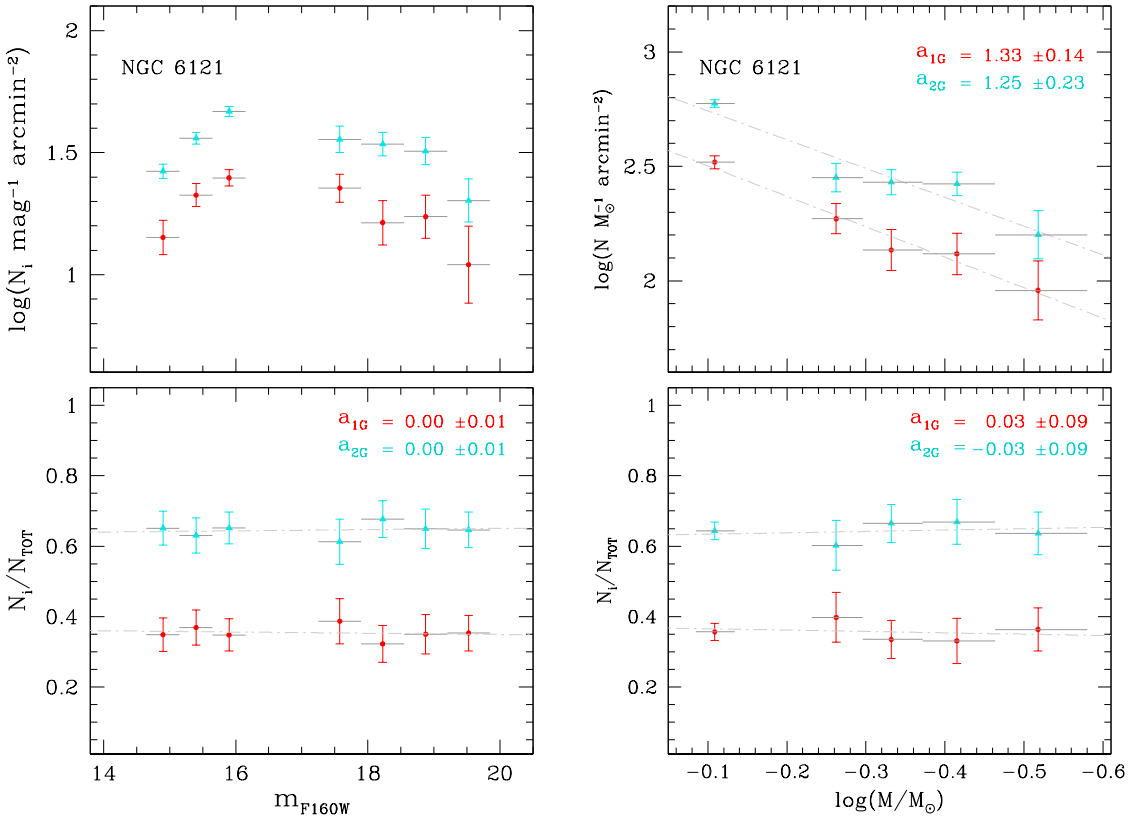

Figure 3.13: *Left panels:* LFs (top) and population ratios (bottom) for 1G and 2G stars in M4, colored in red and azure, respectively. The grey bars and the dot-dashed lines (with their respective slopes) have the same meaning than in Figure 3.10. *Right panels:* same as the right panels of Figure 3.11, but for M4 populations.

NGC 2808 the slopes are negative hence the stellar number increases towards lower stellar masses, while in M4 the positive MF slopes indicate an opposite trend. This observed behavior can be qualitatively explained by considering the expected radial variation of the MF slope. As the cluster evolves, the effects of two-body relaxation (e.g., Spitzer, 1987) drive the segregation of massive stars towards the center and the migration of low-mass stars in the direction of the outskirts. While for NGC 2808 we study stars in an FoV located at $\sim 2r_{\rm hm}$ (with $r_{\rm hm}$ being the half-mass radius of the cluster), for M4 the field includes stars closer to the cluster's center (at $\sim 0.5\ r_{\rm hm}$). For these reasons, we may expect that the MF of NGC 2808 is dominated by low-mass stars, while in the more central FoV covered by our M4 images, the VLM stars constitute the minority of MS stars.

We conclude this Section by noticing that we find only small and not statistically significant differences between the slopes of the different populations in both clusters. As shown in the simulations by Vesperini et al. (2018), small differences between their MF slopes may arise during the dynamical evolution of a GC as a consequence of initial different structural properties (like the 2G stars forming in a more centrally concentrated

Table 3.2: Fraction of MS-II stars in NGC 2808 and fraction of 2G stars in M 4. $R_{\rm min}$ and $R_{\rm max}$ are the minimum and maximum radial distances from the GC centre (in arcmin) of the stars used for each population-ratio measurement.

	$R_{\rm min}$	$R_{\rm max}$	$N_{\rm MSII}/N_{\rm TOT}$	$R_{\rm min}$	$R_{\rm max}$	$N_{\rm MSII}/N_{\rm TOT}$
NGC 2808	0.00	0.60	0.55±0.03[a]	1.63	2.84	0.45±0.04[a]
	0.60	0.82	0.55±0.02[a]	2.86	5.49	0.42±0.03[a]
	0.82	1.03	0.50±0.02[a]	4.20	6.37	0.33±0.04[b]
	1.03	1.63	0.52±0.02[a]	5.50	8.70	0.38±0.05[a]
	$R_{\rm min}$	$R_{\rm max}$	$N_{\rm MSII}/N_{\rm TOT}$			
NGC 6121	0.00	1.69	0.71±0.01[c]			
	0.63	3.31	0.64±0.02[b]			
	5.12	9.63	0.60±0.13[e]			
	9.63	17.81	0.64±0.06[e]			

References: [a]Simioni et al. (2016); [b]this work; [c]Milone et al. (2020b); [d]Milone et al. (2017b); [e]Nardiello et al. (2015).

environment) when they form with the same IMF. Stronger differences between their present-day MFs, according to Vesperini and collaborators, are expected only in case they formed with different IMFs. Therefore, our observations are consistent with 1G and 2G stars sharing the same IMF.

3.7 Radial Distribution of Multiple Populations

In this Section, we investigate the radial distribution of multiple populations by using the fractions inferred in this work combined with literature findings.

In Figure 3.14, we present the radial distribution of the fraction of the most extreme populations detected in both NGC 2808 and M4 (MS-II and 2G, respectively). The filled azure triangles represent the measurements inferred in this study, while the black open dots indicate the literature results. Details about these data are summarized in Table 3.2. The population ratios distributions cover a radial distance up to 8.70 arcmin and 17.8 arcmin in NGC 2808 ($\sim$2.7 $r_{\rm hm}$) and M4 ($\sim$4.2 $r_{\rm hm}$), respectively.

The radial trend of NGC 2808's MS-II (left) clearly shows a decreasing contribution from these stars when moving towards the outer regions, from $\sim$0.55 inside the core radius to $\sim$0.35 at $\sim$2.5 $r_{\rm hm}$. Indeed, the slope of the best-fit straight line of $N_{\rm MSII}/N_{\rm TOT}$ is -0.033±0.0005, consistent with a negative value and hence a decreasing trend.

In the right panel of Figure 3.2, we plot the radial distribution of the fraction of 2G stars in M4, which is consistent with a flat ratio, as demonstrated by the slope of the best-fit straight line (-0.005±0.0004). A possible exception is provided by the innermost bin, in which the 2G stars fraction is slightly higher than the other bins ($\sim$0.71 and

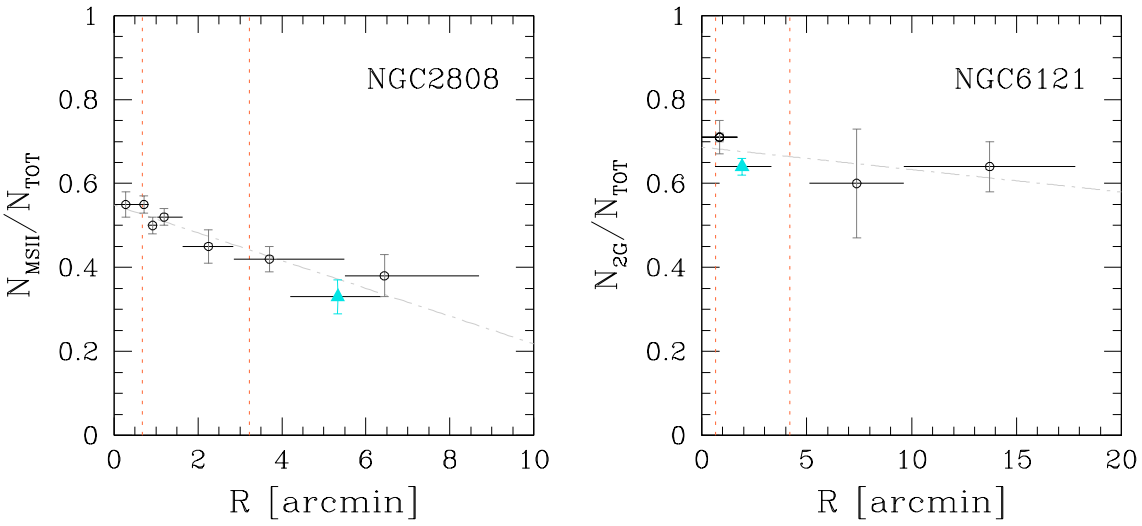

Figure 3.14: Radial distribution of the fraction of MS-II (left panel) and 2G stars (right panel) in NGC 2808 and M 4, respectively. Black circles represent literature results, while the cyan filled triangles show ratios inferred from this work. Black horizontal bars highlight the radial range covered by each measurements. The two dotted-vertical lines indicate the core and half-mass radius. We then show the best-fit straight lines (dot-dashed) in gray.

$\sim$0.63, respectively), but such difference is significant at a 1σ-level only.

3.8 Summary and Conclusions

The early study by Milone et al. (2012b) proved that the F110W-F160W color is an efficient tool to identify multiple stellar populations among GCs' VLM stars. This is because the F160W filter is sensitive to the absorption bands of molecules containing oxygen (mainly water), while the F110W filter is not affected by that. As a consequence, the oxygen-depleted 2G stars in the VLM regime will be redder in the $m_{\rm F110W} - m_{\rm F160W}$ color than the 1G stars. This result allowed subsequent works to study the multiple populations among M-dwarf stars in M4, ωCen, and NGC 6752 (e.g. Milone et al., 2014, 2017b, 2019; Dotter et al., 2015).

In this work, we perform for the first time a homogeneous analysis of the phenomenon for the largest possible sample of clusters with available deep *H*ST NIR images in the F110W and F160W filters, consisting in nine GCs. To that, we also add the open cluster NGC 6791, for which we do not expect the presence of multiple populations.

We find that in all the analyzed GCs, the stars below the MS knee exhibit a color broadening larger than the expectation from observational errors only, which is associated with star-to-star differences in oxygen, i.e., the multiple populations phenomenon. We conclude that it is a widespread phenomenon among M dwarf stars in GCs, as observed for bright MS, RGB, HB, and AGB stars (Carretta et al., 2009b; Piotto et al., 2015; Milone et al., 2017a; Marino et al., 2019a; Lagioia et al., 2021; Dondoglio et al.,

2021). Moreover, the detection of the phenomenon also among the fully convective and unevolved VLM stars corroborates the evidence that the light-elements differences among GC stars are present at their formation rather than being established later due to evolutionary effects.

From our dataset, it is possible to notice how the characteristics of multiple populations significantly change among the GCs in our sample. The F110W-F160W color width, calculated 2 mag below the MS knee, ranges from ∼0.06 in M4 to ∼0.15 mag ωCen, showing a correlation with the mass of the cluster, thus corroborating similar conclusions inferred from the RGB width (e.g. Renzini et al., 2015; Lagioia et al., 2019b; Milone et al., 2017a, 2020a) and from integrated light if GCs (Jang et al., 2021). However, while the F110W-F160W color spread of M dwarf stars is mostly due to oxygen differences, the F275W-F814W color and the $C_{\rm F275W,F336W,F438W}$ used for RGB stars are mainly sensitive to helium and nitrogen. Therefore, our result suggests that the helium, nitrogen, and oxygen abundances are all linked to the mass of the host GC. A remarkable difference between our NIR color and the UV/optical-based filter combinations measured for RGB stars is that the broadening does not correlate with the cluster metallicity. We also find that this quantity strongly correlates with the average 1G-2G [O/Fe] difference inferred by Marino et al. (2019a) from high-resolution spectroscopy of RGB stars, proving that the oxygen variations among VLM and RGB stars are a manifestation of the same phenomenon.

Furthermore, the F110W-F160W color distribution varies from one cluster to another. Indeed, NGC 288, NGC 2808, and M4 exhibit a bimodal VLM stars distribution, whereas NGC 6752 presents a triple sequence of stars. These distributions are consistent with what was found by spectroscopic measurements of giant stars, which revealed a bimodal [O/Fe] distribution in NGC 288 and M4 (Carretta et al., 2009b; Marino et al., 2008, 2011b) and three groups of stars in NGC 6752 (Yong et al., 2005, 2015). On the other hand, NGC 2808 exhibits a more complex pattern, with at least five oxygen-different populations spotted in its RGB (Milone et al., 2015; Carretta, 2015; Marino et al., 2019a). In our observations, the MS-I and MS-II are composed of more than one stellar population each, which our data cannot distinguish. The majority of VLM stars in ωCen define an MS with blue $m_{\rm F110W} - m_{\rm F160W}$ color, but additional stars populate a broader and red sequence (likely hosting more subpopulations that we cannot resolve). In the rest of the GCs, the color distribution appears to be continuous with a predominance of M dwarfs with blue colors. NGC 6656, which exhibits a flatter color distribution, is a possible exception. This is qualitatively consistent with spectroscopic results from the literature, where oxygen variations were detected in these clusters, but without clear signs of discreteness (e.g., Carretta et al., 2009b; Marino et al., 2011c,a; Johnson & Pilachowski, 2010; Gratton et al., 2012b; Cordero et al., 2014). Intensive investigation with photometry and/or spectroscopy is mandatory to dispel all doubts about whether this continuous oxygen distribution is intrinsic or is just the result of observational uncertainties.

In the one open cluster considered in this sample, NGC 6791, the F110W-F160W VLM

distribution defines a narrow sequence consistent with photometric errors, thus indicating no star-to-star oxygen variations. This result is in agreement with the spectroscopic investigations that suggested that NGC 6791 is a single-stellar-population cluster (e.g., Bragaglia et al., 2014; Boberg et al., 2016).

We then exploit our dataset to investigate the LFs and the MFs of multiple populations in NGC 2808 and M4, which are the GCs where the VLM stars define a bimodal behavior. In NGC 2808, we investigate two groups of helium-poor and helium-rich stars, which we call MS-I and MS-II, and are the counterparts of the RGB populations A+B+C and D+E, respectively (see Milone et al., 2015). We combined NIR photometry with observations in F390W to spot the MS-I and MS-II among the upper MS stars in the same three FoVs that we analyze. The main findings on NGC 2808 are summarized as follows:

- The fractions of the MS-I and MS-II stars values 0.67±0.04 and 0.33±0.04, respectively. When comparing this result with similar literature measurements, we notice how the MS-II stars ratio decreases when moving towards the cluster's outskirts, confirming the findings from Simioni et al. (2016), who found that the most helium-rich stars are more centrally concentrated than the helium-poor ones.

- We exploit our photometric tagging of the MS-I and MS-II populations to derive their LF and, through the mass-luminosity relations provided by Dotter et al. (2008), we convert them into MFs (taking into account helium-difference in the stellar models). These quantities are derived over the stellar mass range between ∼0.25 and 0.75 $\mathcal{M}_{\odot}$. We find that the MFs of MS-I and MS-II stars share the same MF slope within uncertainties in this mass range. Moreover, their fractions do not change with stellar mass or luminosity.

We also perform a similar analysis for M4, investigating stars within a FoV located at ∼0.5 half-mass radii from the center of the cluster. We identify two sequences of stars below the MS knee, corresponding to 1G and 2G stars, between ∼0.30 and 0.55 $\mathcal{M}_{\odot}$, using photometry in the F110W and F160W filters of the WFC3/NIR camera. Furthermore, we disentangle the same two populations between ∼0.7 and 0.8 $\mathcal{M}_{\odot}$, thanks to the ChM derived with UV and optical *H*ST filters. Our most relevant results on M4 are the following:

- The fractions of 1G and 2G stars are 0.36±0.02 and 0.64±0.02, respectively, and agree with literature results inferred at a similar radial distance from the center (see Table 3.2). When analyzing the radial behavior of these quantities, which was possible by combining our result with previous findings, we spot no significant radial variation of 1G and 2G fractions, thus suggesting that these two populations are completely mixed in this cluster (with the possible exception of the stars in within the core radius, which exhibits a slightly larger fraction of 2G stars).

- As done for NGC 2808, we compute the LFs and the MFs of 1G and 2G stars. We find no significant differences between the two, with 1G and 2G stars being

consistent with having the same MF slopes. Finally, the population ratios are constant along the whole explored magnitude and stellar mass range.

Our results constrain the multiple populations' formation mechanisms models, in particular the accretion on proto-stellar disk scenarios. Indeed, no differences in MF slopes are found between different stellar populations, thus disagreeing with the prediction of a Bondi-Hoyle-like accretion, where significative differences are instead expected. This is corroborated by the fact that the fraction of multiple populations does not depend on stellar mass, which would be expected in a scenario where 2G stars formed accreting material. Our results on NGC 2808 and M4 are in agreement with the findings of Milone et al. (2019), who compared the three populations of NGC 6752 among RGB and VLM stars and detected no difference in their properties.

Vesperini et al. (2018) investigated, by means of N-body simulations, the long-term evolution of the MF of 1G and 2G stars in GCs. According to their results, the local and global present-day MF slopes of the 1G and 2G populations may show small differences as a result of different dynamical evolution if they formed with the same IMF but the 2G stars were more centrally-concentrated at their birth. In the advanced stages of evolution, when the two populations are mixed, these dynamically induced differences will eventually vanish. Larger discrepancies in the present-day MFs, particularly when considering dynamically old clusters, are instead detected by Vesperini and collaborators in simulations where 1G and 2G stars formed with different IMFs. In this context, the evidence found in this work that the distinct stellar populations of NGC 2808 and M4 share similar MFs is consistent with a scenario where these populations originated with the same IMF (at least in the subsolar range explored here). Notably, if the 2G stars formed in a more centrally-concentrated environment, as suggested by several multiple populations scenarios (e.g., D'Ercole et al., 2010; Calura et al., 2019), the fact that 1G and 2G stars share the same MFs suggests that low-mass star formation is not significantly affected by the density in the formation environment.

CHAPTER 4

Multiple Populations among anomalous stars: the Case of NGC 1851

Abstract

In this Chapter, I present the work focused on NGC 1851, currently accepted for publication in the MNRAS (Dondoglio et al., 2023). This cluster is one of the most studied Type II GCs, surrounded by several controversies regarding the spatial distribution of its populations and the presence of star-to-star [Fe/H], C+N+O, and age differences. We provide a detailed characterization of its stellar groups through *HST*, ground-based, and Gaia photometry.

We identify two distinct populations with different abundances of s-process elements along the RGB and the SGB, detecting two sub-populations among both s-poor (canonical) and s-rich (anomalous) stars. To constrain the chemical composition of these stellar populations, we compare observed and simulated colors of stars with different abundances of helium, carbon, nitrogen, and oxygen, finding that the anomalous has a higher total C+N+O compared to the canonical population and that both display internal light-elements spread.

No significant differences in radial segregation between canonical and anomalous stars are detected, while we find that among their sub-populations, the two most chemically extremes are more centrally concentrated. Anomalous and canonical stars show different 2D spatial distributions outside ∼3 arcmin, with the latter developing an elliptical shape and a stellar overdensity in the northeast direction. We confirm the presence of a stellar halo up to ∼80 arcmin with Gaia photometry, tagging 14 and five of its stars as canonical

and anomalous, respectively, finding a lack of the latter in the south/southeast field.

4.1 Introduction

The existence of a subclass of Galactic GCs that host an additional group of stars beyond the typical 1G-2G pattern -the so-called Type II GCs introduced in Section 1.3- constitutes one of the most obscure sides of GCs. Recalling what stated in Chapter 1, Type II (or anomalous) GCs host a group of stars with the following three observational features: (i) a split SGB in optical CMDs, with the additional population populating the faintest of the two, (ii) a secondary redder RGB, connected to the faint SGB, and (iii) chemical abundances variations in C+N+O, metallicity and/or s-process elements (see Milone et al., 2017a). In the rest of this Chapter, we will refer hereafter as 'canonical' the stars that yield the multiple population patterns observed in all GCs and as 'anomalous' the stars present in Type II only.

A lot of questions remain unsolved regarding the nature of these objects. What is the origin of anomalous stars? Why do they appear in some GCs and not in others? Did these GCs originate through different mechanisms than the Type I clusters? Which is the sequence of events in the star formation history of these objects that led to such a complex chemical pattern?

In this context, NGC 1851 is one of the most studied GCs, which thanks to its relative proximity and not excessive complexity, makes it possible to investigate the anomalous stars in detail. Indeed, NGC 1851 has been historically one of the most appealing targets for studies, using both photometry and spectroscopy, aimed to shed light on the mechanisms that produced the Type II clusters we nowadays observe. Photometry allowed the discovery of the first sign of anomaly, i.e. the presence of a split SGB in CMDs built with optical filters (Milone et al., 2008, 2009b; Zoccali et al., 2009). The faint and bright SGBs evolve into the red and blue RGBs, respectively, a feature visible especially in the $U - I$ colors (Han et al., 2009; Milone et al., 2017a; Jang et al., 2022).

Intensive spectroscopy studies from the past $\sim$15 years showed that the anomalous SGB and RGB stars are enhanced in their s-process elements abundances (e.g., Yong et al., 2008; Villanova et al., 2010; Carretta et al., 2011; Gratton et al., 2012b; Marino et al., 2014b; McKenzie et al., 2022; Tautvaišienė et al., 2022) and that the bulk of anomalous stars, as the canonical, exhibit internal light-elements variations in elements such as carbon, nitrogen, oxygen, and sodium (e.g., Yong et al., 2009, 2008; Lardo et al., 2012; Carretta et al., 2010, 2014; Campbell et al., 2012; Simpson et al., 2017).

No agreement has been currently reached on the nature of the physical phenomenon that produced stars with these observational features. Works based on the comparison between photometry and stellar models reveal that the faint SGB is consistent with a stellar population that is either $\sim$1 Gyr older or has nearly the same age but is enhanced in its overall C+N+O content by a factor of $\sim$3 than the bright-SGB population (Cassisi et al., 2008; D'Antona et al., 2009; Ventura et al., 2009). However, the spectroscopic

investigation led to contrasting results. The works by Yong et al. (2009, 2015) and Simpson et al. (2017) detected a large difference in the overall C+N+O content between s-rich and s-poor stars, whereas according to other authors (e.g., Villanova et al., 2010; Tautvaišienė et al., 2022) the canonical and anomalous stars in NGC 1851 share the total C+N+O amount. Furthermore, debate is also present on whether the anomalous population is enriched in [Fe/H] of about 0.05-0.10 dex or not (see Gratton et al., 2012b; Lardo et al., 2012; Tautvaišienė et al., 2022, for discussion on the presence or lack of metallicity difference between s-rich and s-poor stars in NGC 1851).

Moreover, another controversial topic regarding this GC is the presence or lack thereof of radial distribution differences between the canonical and anomalous stars. For example, Zoccali et al. (2009) concluded that the faint SGB stars are more centrally concentrated and tend to disappear when moving toward the cluster's outskirts. On the other hand, Milone et al. (2009b) found no significant differences between the radial distribution of the two SGB populations (see also Cummings et al., 2014).

In this Chapter, we exploit photometry from different space- and ground-based facilities to provide new tools for the characterization of the several populations harbored in NGC 1851, focusing on their chemical composition and spatial distribution. Section 4.2 describes the dataset used in our work. Section 4.3 presents the main photometric tools adopted to disentangle the multiple populations of NGC 1851 among RGB stars, while in Section 4.4, we use them to infer the chemical composition of the groups of stars that we can disentangle. Section 4.5 is dedicated to hunting canonical and anomalous stars, as well as their subpopulations, along the SGB and the MS. In Section 4.6, we calculate the fraction of the spotted multiple stellar populations and investigate their radial distribution, whereas in Section 4.7, we explore the 2D spacial distribution of canonical and anomalous stars. We conclude by summarizing the results of this Chapter in Section 4.8.

4.2 Dataset

In this work, we exploit three photometric datasets. First, we build a catalog of the innermost $\sim$2.7$\times$2.7 arcmin^2 stars by exploiting *HST* observations taken with the WFC3/UVIS filters F275W, F336W, and F438W (GO-13297), ACS/WFC filters F606W and F814W (GO-10775). We reduce these images by performing PSF photometry following the procedure introduced in Section 2.2 and the same recipes to calibrate and select well-measured stars. To investigate the cluster regions outside the *H*ST FoV, we use the ground-based catalog by Stetson et al. (2019). Again, we treat this dataset as in Section 2.2. Well-measured stars in this catalog reach distances around 20 arcmin from the center, allowing us to cover the cluster from its center to beyond the tidal radius.

No correction for differential reddening has been performed in both datasets since this cluster is characterized by very small reddening variations (Jang et al., 2022; Legnardi et al., 2023), which produce negligible effects on the photometric quality. We instead correct this catalog for zero-point spatial variations effects, following the recipe presented in Milone et al. (2012c, see their Section 3.2).

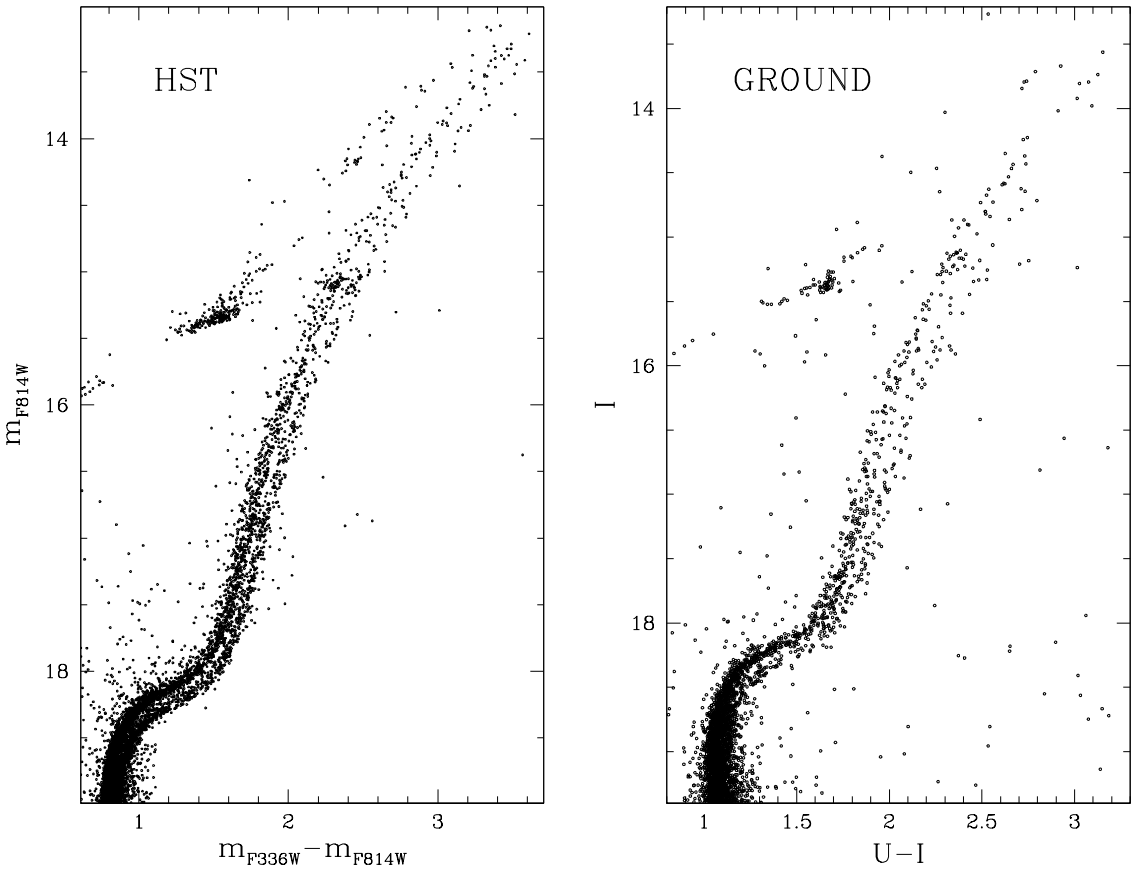

Figure 4.1: *Left panel:* $m_{\rm F814W}$ vs. $m_{\rm F336W} - m_{\rm F814W}$ CMD obtained from *H*ST photometry. *Right panel:* I vs. $U - I$ CMD obtained from the ground-based observations.

Figure 4.1 illustrates the resulting CMDs in both catalogs. Specifically, we show the $m_{\rm F814W}$ vs. $m_{\rm F336W} - m_{\rm F814W}$ CMD (left panel) from *H*ST photometry, and the I vs. $U - I$ (right panel) CMD from ground-based photometry. In both diagrams, two sequences are distinguishable from the SGB up to the RGB tip.

Finally, we exploit Gaia Data Release 3 (DR3, Gaia Collaboration et al., 2021) observations to explore the stars in the halo of NGC 1851 (i.e., at distances much larger than the tidal radius), reaching a radial distance of about 80 arcmin from the center. This feature will be discussed in Section 4.7.

4.3 A Zoo of Populations Along the Red Giant Branch

Here, we exploit *H*ST and ground-based photometry to investigate multiple populations among the RGB of NGC 1851. To do that, we use the ChM approach (see Section 3.6.1) to build a new ChM optimized for disentangling canonical and anomalous stars and spotting, at the same time, light element variations among these groups.

The $m_{\rm F336W} - m_{\rm F814W}$ and the analogous $U - I$ colors are effective tools in separating the canonical and anomalous RGBs (see discussion in the introduction of this Chapter). For the *H*ST dataset, we combine this information with the $C_{\rm F275W,F336W,F438W}$ pseudo-

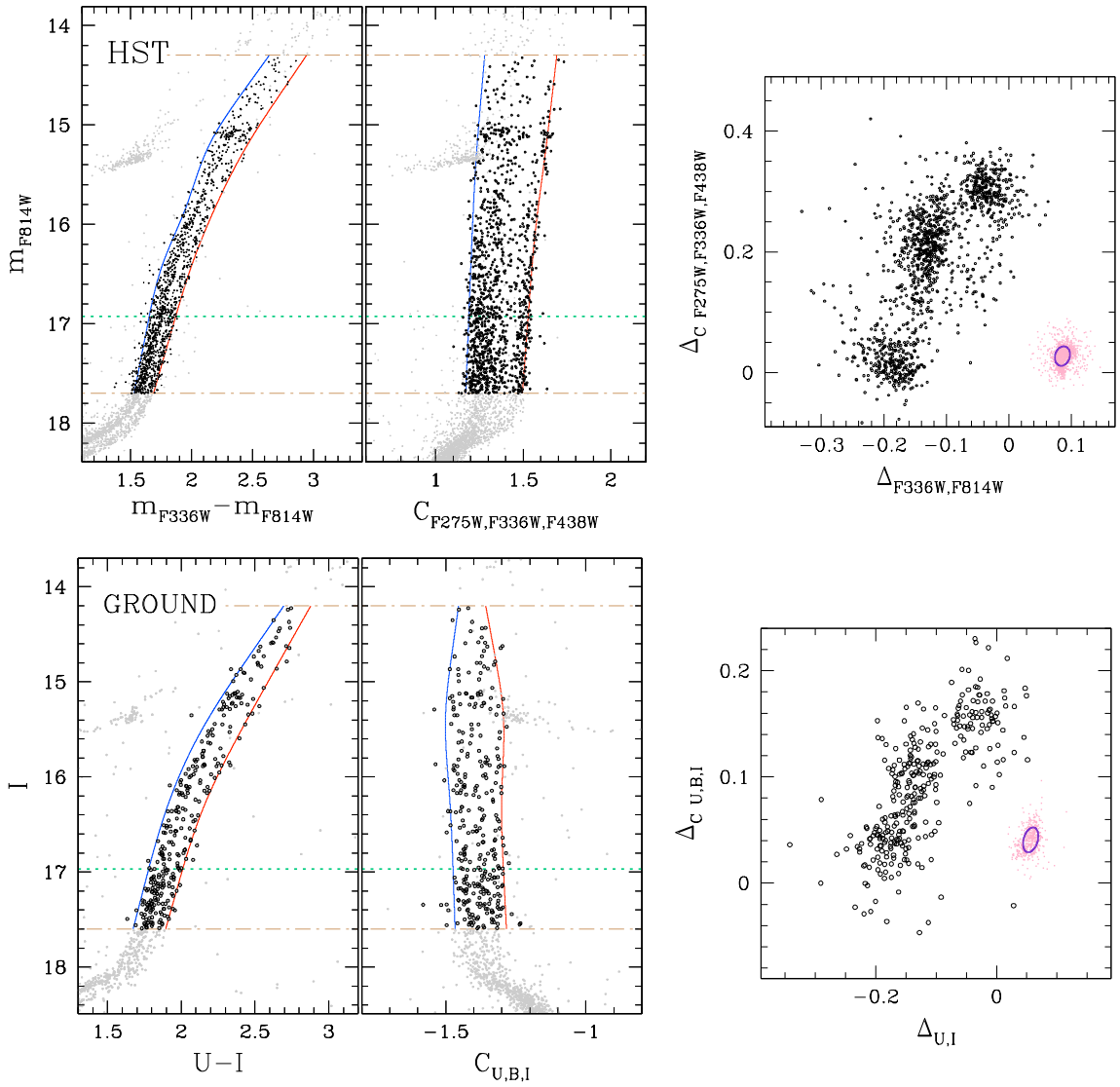

Figure 4.2: *Top-left and -middle panels:* m_{F814W} vs. $m_{\rm F336W} - m_{F814W}$ CMD and m_{F814W} vs. $C_{\rm F275W,F336W,F438W}$ pseudo-CMD of stars in the *H*ST FoV. *Top-right panel:* $\Delta_{\rm CF275W,F336W,F438W}$ vs. $\Delta_{\rm F336W,F814W}$ ChM of RGB stars. *Bottom-Left and -middle panels:* I vs. $U-I$ CMD and I vs. $C_{\rm U,B,I}$ pseudo-CMD of stars in the ground field. *Bottom-right panel:* $\Delta_{\rm CU,B,I}$ vs. $\Delta_{\rm U,I}$ ChM of RGB stars. The brown dot-dashed horizontal lines separate the stars included (black points) and excluded (grey points) from each ChM determination. The dotted aqua lines indicate the magnitude level at which the ChM widths were normalized (see the text for details). Pink points illustrate the distribution in both ChMs of a simulated single stellar population, while the purple ellipses include 68.27% of the simulated stars.

color, which is particularly effective in spotting star-to-star carbon, nitrogen, and oxygen variations (see Milone & Marino 2022 and reference therein).

In Figure 4.2, we present the procedure to derive the ChM that combines these two filter combinations for the RGB stars within $14.3 < m_{\rm F814W} < 17.7$ (black dots), a

magnitude interval where the different sequences are well separated in both the $m_{\rm F814W}$ vs. $m_{\rm F336W} - m_{\rm F814W}$ CMD (upper-left panel) and the $m_{\rm F814W}$ vs. $C_{\rm F275W,F336W,F438W}$ pseudo-CMD (upper-middle panel). We follow the method by Milone et al. (2017a, see their Section 3.1 and 3.2) to derive the red and blue boundaries in both diagrams. Moreover, we estimate the RGB width, defined as the difference between the red and blue boundaries at a magnitude level of 2 $m_{\rm F814W}$ above the MS Turn-Off (dotted aqua line). Finally, by applying their equations (1) and (2), we calculate the ChM coordinates $\Delta_{\rm F336W,F814W}$ and $\Delta_{\rm CF275W,F336W,F438W}$, which we plot in the upper-right panel of Figure 4.2. We simulate, through AS tests, how a simple stellar population would behave in the ChM plane. The simulated points are arbitrarily shifted near the bottom-right corner of the ChM and represented in pink, while the purple ellipse includes 68.27% of them.

We then follow a similar approach to analyze the ground-based $U-I$ color, analogous to $m_{\rm F336W} - m_{\rm F814W}$, and $C_{\rm U,B,I}$ pseudo-color, which can efficiently separate stellar populations with different light-elements abundances (e.g., Jang et al., 2022). The I vs. $U-I$ and I vs. $C_{\rm U,B,I}$ diagrams are displayed in the bottom-left and middle panels, respectively, whereas the resulting $\Delta_{\rm CU,B,I}$ vs $\Delta_{\rm U,I}$ ChM is plotted in the bottom-right panel of Figure 4.2.

From a visual inspection of the derived ChMs, both canonical and anomalous stars define two distinct sequences with $\Delta_{\rm F336W,F814W}$ (and $\Delta_{\rm U,I}$) smaller and larger than ~ -0.1, respectively. Furthermore, both groups of stars show a $\Delta_{\rm CF275W,F336W,F438W}$ and $\Delta_{\rm CU,B,I}$ distributions wider than what expected from observational errors only. This proves that both RGBs harbor stars with light-elements differences. Specifically, we detect the 1G and 2G stars typically present in all GCs among the canonical stars, forming two blobs in the ChMs and two anomalous populations distinguishable in the *H*ST-based ChM (hereafter AI and AII). Notably, the 2G population spans a $\Delta_{\rm CF275W,F336W,F438W}$ and $\Delta_{\rm CU,B,I}$ interval not consistent with a chemically-homogeneous population, thus indicating a complex chemical composition of its stars.

In Figure 4.3, we highlight with ellipses the ChM regions that host the bulk of 1G, 2G, AI, and AII stars. These ellipses are defined following a similar procedure of Dondoglio et al. (2022, see also Section 3.6.1) and are used to derive the fraction of each population. Briefly, we first select by hand the bonafide members of each blob of stars corresponding to a stellar population in the ChM. We measure the median of their ChM coordinates to define the center of our elliptic regions. Secondly, to find the major axis direction, we consider the direction of a line that crosses the center and minimizes the orthogonal dispersion of the bonafide members. The third and final step consists of setting the semi-major and -minor axis length of each ellipse as 2.5 times the dispersion of stars along the directions parallel and orthogonal to the major axis direction, respectively. The ellipses that encapsulate 1G and 2G stars are colored green and azure, respectively, while the bulk of AI and AII stars lie within the yellow and purple ellipses, respectively. Being a poorly populated group, the AI stars do not form a distinguishable blob in the ground-based ChM. Although we could not classify them with confidence as a distinct

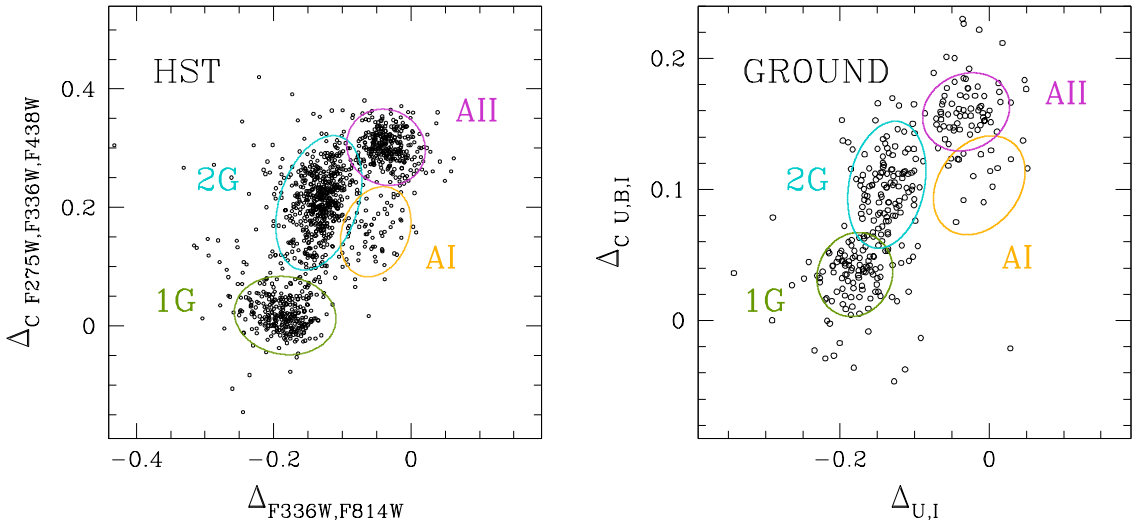

Figure 4.3: Elliptical regions that encapsulate each spotted population in the *H*ST and ground-based (left and right panels, respectively) ChMs. Green and azure ellipses define the 1G and 2G regions of canonical stars, while the yellow and purple ones are the AI and AII regions of anomalous stars.

population by using this diagram alone, guided by the separation observed in the *H*ST ChM, we define by eye an ellipse that encloses the probable AI stars identified from ground-based photometry.

To calculate the fraction of each RGB population, we follow a procedure widely adopted by our group throughout the years. As an example, to estimate the fraction of 1G stars, we start by counting the stars within the green ellipse, which provides a crude estimate of their contribution. Then, we subtract from this value the number of expected 2G, AI, and AII stars falling within the 1G region and added the number of 1G stars expected to fall outside the green ellipse due to photometric errors to derive a more accurate estimate of the fraction of 1G stars. These quantities are derived utilizing AS tests (see Section 3.2.1 and Milone et al., 2012a; Zennaro et al., 2019; Dondoglio et al., 2022, for details). We repeat the procedure for the other three populations to derive the fraction of 2G, AI, and AII stars.

The results are reported in Table 4.1. We find that canonical and anomalous stars include ∼70% and ∼30% of the RGB stars, respectively. 1G stars comprise more than one-third of the total number of canonical stars, whereas AI stars include less than 10% of the anomalous stars.

4.4 The Chemical Composition of the Multiple Stellar Populations in NGC 1851

We dedicate this Section to derive the average chemical composition of the four stellar populations identified along the RGB. To do that, we combine our photometric tagging with GIRAFFE spectroscopy of 124 RGB stars of NGC 1851 from Carretta et al. (2011).

Table 4.1: Average fraction of the populations identified in NGC 1851 inferred from *HST* (within the innermost 1.5 arcmin), ground-based photometry (outside 1.5 arcmin) and over the whole cluster field from its center to the tidal radius. Values inside brackets indicate, when present, the analogous fraction estimated from SGB stars.

	Fraction <1.5 arcmin)	Fraction (>1.5 arcmin)	Fraction (global)
CANONICAL	0.701 ± 0.014 (0.706 ± 0.027)	0.721 ± 0.031 (0.728 ± 0.031)	0.705 ± 0.029 (0.720 ± 0.030)
1G	0.368 ± 0.018	0.437 ± 0.039	0.330 ± 0.038
2G	0.632 ± 0.018	0.563 ± 0.039	0.670 ± 0.038
ANOMALOUS	0.299 ± 0.014 (0.294 ± 0.027)	0.279 ± 0.031 (0.272 ± 0.031)	0.295 ± 0.029 (0.280 ± 0.030)
AI	0.094 ± 0.027	0.229 ± 0.057	0.097 ± 0.051
AII	0.906 ± 0.027	0.771 ± 0.057	0.903 ± 0.051

The left panels of Figure 4.4 represent the ChMs introduced in Figure 4.2, where we encircle stars in common with this spectroscopic dataset, color-coded according to their belonging to the ellipses defined in Figure 4.3. The upper-middle and -right panels display the sodium-oxygen anticorrelation among the canonical and anomalous stars for which both our photometric tagging and abundance measurements from Carretta and collaborators are available. Filled points with black contours indicate the average abundances. The anomalous stars span [Na/Fe] and [O/Fe] intervals smaller than the canonical ones, but both populations are not consistent with being chemically homogeneous. As expected, we find that 2G stars have on average larger sodium and smaller oxygen than 1G stars -and similarly- the AII stars display larger sodium and smaller sodium than AI stars. Intriguingly, AI stars are sodium-richer than the 1G, in analogy with what is observed in other Type II GCs (e.g., Marino et al., 2009, 2011b,c).

In the lower-middle and -right panels of Figure 4.4, we illustrate the [Ba/Fe] vs. [Fe/H] diagram, from which it is clear that the anomalous stars present a higher barium abundance, while no significant iron differences are detected. There is no evidence of internal variations among canonical stars, while the anomalous population spans a larger [Ba/Fe] range. Notably, AI stars show a larger average barium abundance than the AII (even though we are limited by a sample of just three AI stars). Table 4.2 reports the average [O/Fe], [Na/Fe], [Ba/Fe], and [Fe/H] of canonical and anomalous stars and their subpopulations.

This comparison corroborates our results inferred from photometry alone. Indeed, our finding of separate 1G and 2G stars and AI and AII stars sequences, and that these stars occupy different regions in the [Na/Fe] vs. [O/Fe] plane, are in agreement with previous spectroscopic determinations (see Carretta et al., 2010; Tautvaišienė et al., 2022). We also note that the three AI stars (two of which are tagged with the ground-based ChM) with available spectroscopy are well separated from the AII blob in the sodium-oxygen

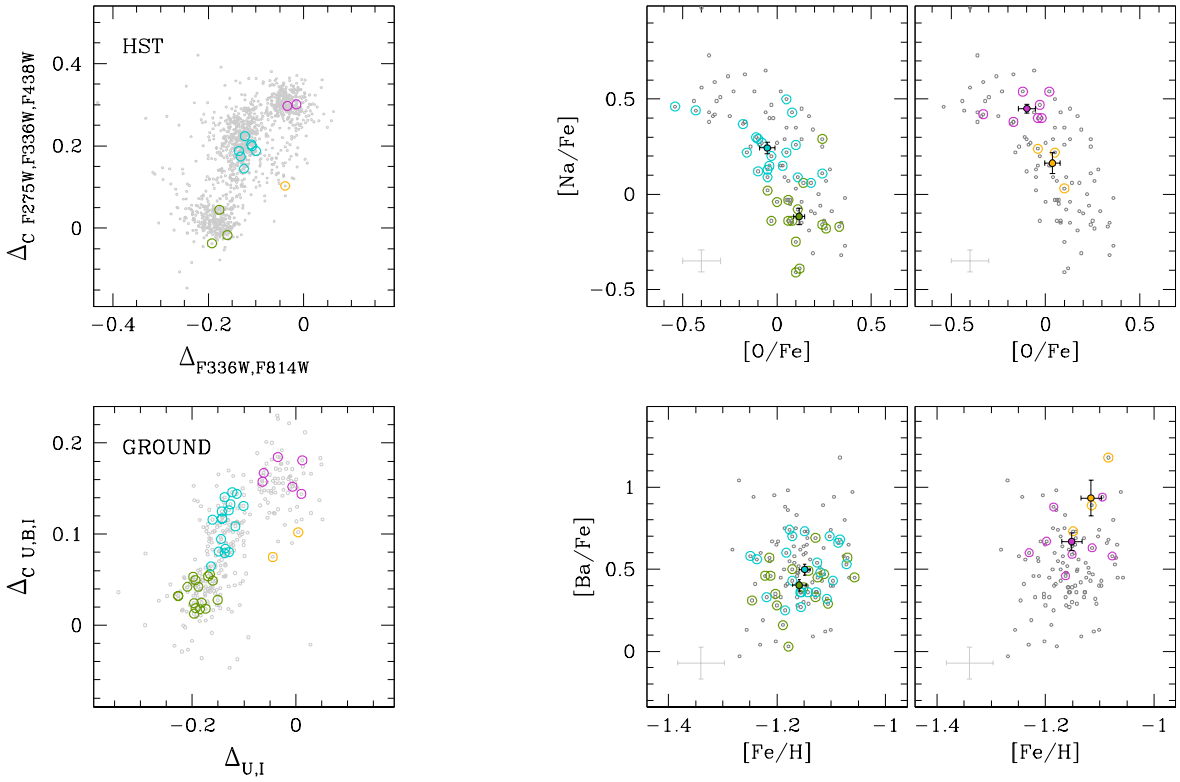

Figure 4.4: *Left panels:* HST (upper) and ground-based (bottom) ChMs where the stars in common with the spectroscopic datset from Carretta et al. (2011) are highlighted with open bullets, color-coded following the prescriptions of Figure 4.3. *Middle panels:* Reproduction of the [Na/Fe] vs. [O/Fe] and [Ba/Fe] vs. [Fe/H] relations for the two canonical populations (upper and lower panels, respectively). Dark-grey points represent all the stars in the Carretta and collaborators' dataset. Filled dots with black contours mark the average abundance of stars in each population and black bars indicate their errors. Gray bars highlight the average uncertainties of the spectroscopic measurements. *Right panels:* same as the middle panels but for the two anomalous populations.

diagram, thus independently supporting the validity of our photometric tagging in both the *H*ST- and ground-based ChMs.

We further investigate the chemical composition of the different populations harbored by NGC 1851 by comparing the information from multi-band photometry with synthetic spectra. To do that, we adopt a method that was extensively applied by our group (Milone et al., 2012b; Milone et al., 2018b; Lagioia et al., 2019b), which allows us to constrain the relative differences of helium, carbon, nitrogen, and oxygen between two populations. Here, we compare 1G and 2G, canonical and anomalous, and AI and AII stars. In a nutshell, this method consists in deriving the RGB fiducial line of each population in the $m_{\rm F814W}$ vs. $m_{\rm X} - m_{\rm F814W}$ (for *H*ST observations) and in the I vs. $X-I$ (in the ground-based catalog) CMDs, where X=F275W, F336W, F438W, F606W, and F814W and U, B, V, R, and I, respectively. Then, we select three equally-spaced reference magnitudes ($m_{\rm ref}$) fainter than the RGB bump. For each $m_{\rm ref}$, we measure

Table 4.2: Average chemical abundances (from Carretta et al., 2011) of the populations photometrically tagged among RGB stars.

	[O/Fe]	[Na/Fe]	[Ba/Fe]	[Fe/H]
CANONICAL	0.209 ± 0.030	0.089 ± 0.040	0.456 ± 0.029	-1.153 ± 0.008
1G	0.117 ± 0.028	-0.117 ± 0.045	0.403 ± 0.037	-1.159 ± 0.013
2G	-0.052 ± 0.041	0.243 ± 0.031	0.499 ± 0.034	-1.149 ± 0.010
ANOMALOUS	-0.058 ± 0.039	0.364 ± 0.050	0.741 ± 0.063	-1.142 ± 0.016
AI	0.037 ± 0.041	0.163 ± 0.067	0.933 ± 0.132	-1.116 ± 0.019
AII	-0.099 ± 0.046	0.450 ± 0.026	0.669 ± 0.057	-1.152 ± 0.019

the color difference $\Delta(m_{\rm X} - m_{\rm F814W})$ and $\Delta(X - I)$ between the fiducial lines of the two populations that we are comparing. Figure 4.5 portrays the example for $m_{\rm ref}$ =15.5 mag, where the results from *HST* and ground-based observations are shown in the left and right panels, respectively.

From the upper panels, we notice that the 1G and 2G color differences display a typical pattern for this kind of populations, as observed in several GCs (Milone et al., 2018b). 2G stars are typically bluer than the 1G, with the maximum color separation for X=F275W, except the F336W-F814W (and $U - I$) color, in which 2G stars are the reddest of the two populations.

To infer the relative helium, carbon, nitrogen, and oxygen abundances between 1G and 2G stars, we first derive the effective $T_{\rm eff}$ and gravity (g) corresponding to a given $m_{\rm ref}$ by using the best-fitting isochrones from Ventura et al. (2009) and D'Antona et al. (2009). We compute a reference spectrum for a star with these $T_{\rm eff}$ and g fixing a primordial helium, Y =0.246, and 1G-like chemical composition with [O/Fe]=0.4 dex, solar carbon abundance, and [N/Fe]=0.5 dex. Then, we build a grid of comparison spectra varying Y from 0.246 to 0.280 with steps of 0.001, [O/Fe] from 0.0 to 0.6 dex in steps of 0.01 dex, while both [C/Fe] and [N/Fe] span the intervals between -0.5 to 0.2 dex and between 0.5 and 2.0 dex, in steps of 0.01 dex. When we use the He-enhanced chemical composition, we adopt the corresponding values for the $T_{\rm eff}$ and gravity derived by the isochrones. We use spectra computed with the ATLAS12 and SYNTHE computer programs (e.g., Castelli, 2005; Kurucz, 2005; Sbordone et al., 2007). We do not vary the total C+N+O abundance in the isochrones. We find that 2G stars are enhanced in nitrogen by 0.80±0.10 dex, and depleted in carbon and oxygen by 0.25±0.10 and 0.20±0.10, respectively, with respect to 1G stars. Furthermore, 2G stars have a slightly larger helium mass fraction, being increased by ΔY =0.008±0.006.

The errors are estimated as the dispersion of the abundance determinations corresponding to the three magnitude levels, divided by the square root of two. We repeat the same analysis by using isochrones from the Dartmouth database (Dotter et al., 2008).

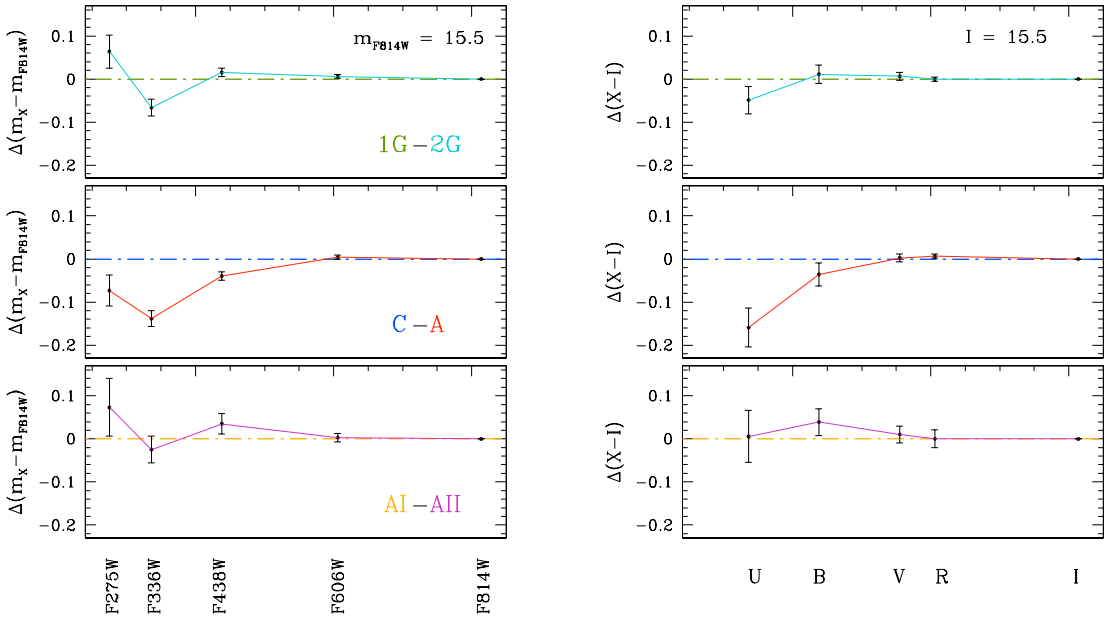

Figure 4.5: *Left panels:* $\Delta(m_{\rm X} - m_{\rm F814W})$ between different populations in the *H*ST filters at a magnitude level $m_{\rm F814W}$ 15.5, with X=F275W, F336W, F438W, F606W, and F814W. From top to bottom, 1G and 2G, canonical and anomalous, AI and AII stellar populations are compared. *Right panels:* same as left panels but for the ground-based filters. Here, X=U, B, V, R, and I.

Specifically, we infer differences in [C/Fe], [N/Fe], and [O/Fe] between 2G and 1G stars of 0.85∼0.10 dex, and depleted in carbon and oxygen of 0.25∼0.10 and 0.30∼0.10, respectively. Moreover, we find a difference in helium mass fraction of ΔY =0.007±0.005.

We repeat the same approach to infer the relative abundance differences of canonical and anomalous stars (middle panels). The latter are redder than the former when X=F275W, F336W, and F438W for *H*ST observation and when X=U and B in the ground-based photometry. Conversely, the color differences disappear in the F606W-F814W, $V - I$, and $R - I$ combinations.

We first compare our photometry with synthetic spectra by considering isochrones that share the same total C+N+O and helium component. In this configuration, we find that to justify the observed colors the anomalous stars should be enhanced in both carbon and nitrogen by ∼0.9 dex and in oxygen by ∼0.8 dex compared to the canonical population. The results on carbon and oxygen are in strong contrast with several spectroscopic investigations, where no significant carbon differences were detected, and with the oxygen being either consistent with no variations or with being less abundant in the anomalous populations (Yong et al., 2015; Tautvaišienė et al., 2022). Moreover, this result implies that anomalous stars are indeed enhanced in total C+N+O hence the atmospheric parameters that we use to compute the spectra of the anomalous stars are based on the wrong isochrones (i.e., nonrealistic $T_{\rm eff}$ and g).

As a consequence, we take into account isochrones with enhanced total C+N+O to

derive the atmospheric parameters of anomalous stars. Specifically, we exploit the stellar models provided by D'Antona et al. (2009); Ventura et al. (2009), which are enhanced in a total C+N+O values such that they can reproduce the double SGB of NGC 1851 and have pristine helium abundance Y =0.25. The most remarkable difference for RGB stars consists of the CNO-enhanced isochrone being about 30 K colder than the model that reproduces the canonical stars.

By assuming that the canonical and anomalous stars share the same helium content, we reproduce their relative colors by assuming that the anomalous are enhanced in nitrogen by 0.90±0.15 dex and share the same carbon and oxygen abundances (Δ[C/Fe]=0.10±0.15 and Δ[O/Fe]=-0.05±0.15) within observational errors. We thus confirm the results by Yong et al. (2015) based on high-resolution spectroscopy.

Finally, we infer the relative abundances of AI and AII stars (lower panels), by using the same approach used for the 1G and 2G stars. Based on the isochrones from the Roma database (Ventura et al., 2009; D'Antona et al., 2009), we find that AII stars have slightly higher content of helium and nitrogen (ΔY=0.005±0.013 and Δ[N/Fe]=0.30±0.20), and lower abundances of carbon and oxygen (Δ[C/Fe]=-0.25±0.15 and Δ[O/Fe]=-0.20±0.10 dex) than AI stars. We obtain similar conclusions by using the ischrones from Dotter et al. (2008) (ΔY=0.006±0.011, Δ[C/Fe]=-0.30±0.15, Δ[N/Fe]=0.40±0.20, and Δ[O/Fe]=-0.15±0.15 dex).

4.4.1 Comparison with Yong et al. (2015)

The relative difference in the F438W/B bands between canonical and anomalous stars can explain the distribution in the $C_{\rm B,V,I}$ pseudo-color of RGB stars shown in panel a) of Figure 4.6. This color combination, as first discovered by Marino et al. (2015), is effective in separating canonical and anomalous stars in all the studied Type II GCs (see also Marino et al. 2019a). Here, the anomalous stars display a redder and wider $C_{\rm B,V,I}$ pseudo-color distribution than the canonicals. To highlight these features, we build the $\Delta_{\rm CB,V,I}$ vs. $\Delta_{\rm U,I}$ ChM for the RGB stars between $17.2 < I < 11.8$ mag (the black stars in panel a)), portrayed in panel b). In this plot, canonical and anomalous stars (at $\Delta_{\rm U,I}$ smaller and larger than ~ -0.1) show a different extension along the y-axis, with the latter spanning a larger $\Delta_{\rm CB,V,I}$ range. To better highlight that, we show in panel c1) the kernel density distributions of both populations, whereas panel c2) represents the same quantity but for their subpopulations. While the canonical 1G and 2G stars overlap in their $\Delta_{\rm CB,V,I}$ distribution, the AI and AII populations are only partially superimposed and peak at ∼0.04 and ∼0.02, respectively. These results are consistent with what we found in Figure 4.5, so with a null F438W/B spread among canonical stars and with the anomalous being enhanced in these bands and showing an internal spread.

We now exploit the $\Delta_{\rm CB,V,I}$ quantity to explore its link with the C, N, and O measurements by Yong et al. (2015), who measured their abundances for a sample of 15 giants and concluded that the anomalous stars are enriched in total C+N+O. In panels d1)-d4), from left to right, we illustrate the $\Delta_{\rm CB,V,I}$ vs. carbon, nitrogen, oxygen, and

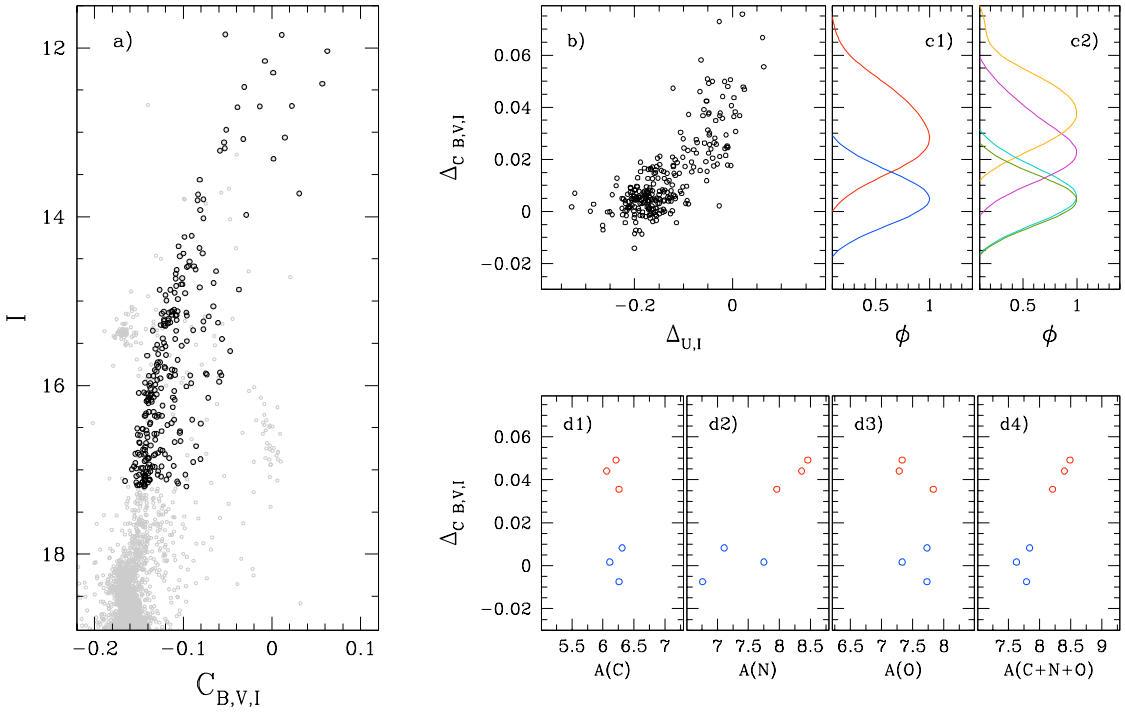

Figure 4.6: *Panel a):* I vs. $C_{\rm B,V,I}$ pseudo-CMD. RGB stars with $11.8 < I < 17.2$ are highlighted with black points, while the remaining stars are colored in grey. *Panel b):* $\Delta_{\rm CB,V,I}$ vs. $\Delta_{\rm U,I}$ ChM for stars marked with black points in panel a). *Panels c1) and c2):* $\Delta_{\rm CB,V,I}$ kernel density distribution of canonical and anomalous stars and their sub-populations, respectively. *Panels d1)-d4):* $\Delta_{\rm CB,V,I}$ vs. C, N, O, and C+N+O abundances for stars in common with the Yong et al. (2015) dataset. Blue and red points highlight the stars that, according to their position on the $\Delta_{\rm CB,V,I}$ vs. $\Delta_{\rm U,I}$ ChM, are canonical and anomalous, respectively.

their sum derived by Yong and collaborators for the six stars tagged in both datasets. We color in blue and red the stars that, based on our photometric investigation, we classify as canonical and anomalous. The carbon and oxygen element abundances span similar range, independently of their classification, thus suggesting no significant differences between the two populations, while the nitrogen abundance changes between the two, increasing among the anomalous stars, presenting a correlation with $\Delta_{\rm CB,V,I}$ (Spearman's rank correlation coefficient 0.94). The nitrogen variation, as a consequence, drives the observed correlation between $\Delta_{\rm CB,V,I}$ and the total C+N+O. These results corroborate our findings from synthetic spectra on the presence of a total C+N+O enhancement among anomalous stars.

4.5 Multiple Populations along the Sub-Giant branch and the Main Sequence

RGB stars are the ideal target for the study of multiple populations in GCs, thanks in part to their brightness that ensures low photometric errors. Moreover, their structure and atmospheric parameters make these stars' colors and magnitudes particularly sensitive to light-elements abundance differences. But can we identify the counterparts of the populations defined in the previous Section even among fainter stars? In this Section, we explore the SGB and the MS of NGC 1851 to hunt for the multiple populations in these evolutionary phases.

4.5.1 The Sub-Giant Branch of NGC 1851

From the CMDs in Figure 4.1, a double SGB is visible, with the bright and faint sequences being connected to the blue and red RGBs, hence they are the counterparts of the canonical and anomalous stars, respectively.

Figure 4.7 illustrates the procedure to identify the multiple populations among the SGB in the *H*ST dataset. The first step consists of selecting the bulk of bright and faint SGB stars from the $m_{\rm F336W}$ vs. $m_{\rm F336W} - m_{\rm F814W}$ CMD (panel a)). For that, we derive the fiducial lines of the two SGBs by selecting by eye bonafide stars, calculating the median color and magnitude in different color bins, and fitting these pairs of points with cubic splines (blue and red lines in panel a)). We then calculate the maximum and minimum magnitude of both fiducials, displayed with aqua bullets, and exploit them to define our sample of faint and bright SGB stars at similar evolutionary stages (black points in Figure 4.7a) as the ones between the two lines that cross the bluest and reddest pair of aqua points.

The next step involves verticalizing the SGB stars' distribution to better investigate their subpopulations. To do that, we apply to colors and magnitudes in the CMD the transformations by Milone et al. (2009b, see their Appendix A), to move into the reference frame ('abscissa', 'ordinate') shown in panel b), where the two brown lines defined in panel a) are vertical, and the aqua points lie at coordinates (0,0), (0,1), (1,0), and (1,1). Here, the canonical and anomalous stars form sequences centered around 'abscissa' 0 and 1, respectively. Then, we apply the method described in Section 4.3 to derive the blue and red boundaries of the stellar 'abscissa' distribution to derive the verticalized Δ'abscissa', which is plotted in panel c) against the 'ordinate'.

To improve our selection of SGB stars, we compute the histogram distribution of Δ'abscissa', displayed in panel d), and fit its two peaks with the sum of two Gaussian functions employing least squares. The two components of this function are represented in blue and red. We exclude from our sample of SGB stars the ones lying outside the external dot-dashed lines, which are obtained by shifting the center of the blue and the red Gaussian function by three times their standard deviations. The central lines divide the SGB region into two areas, which are populated by the bulk of canonical and

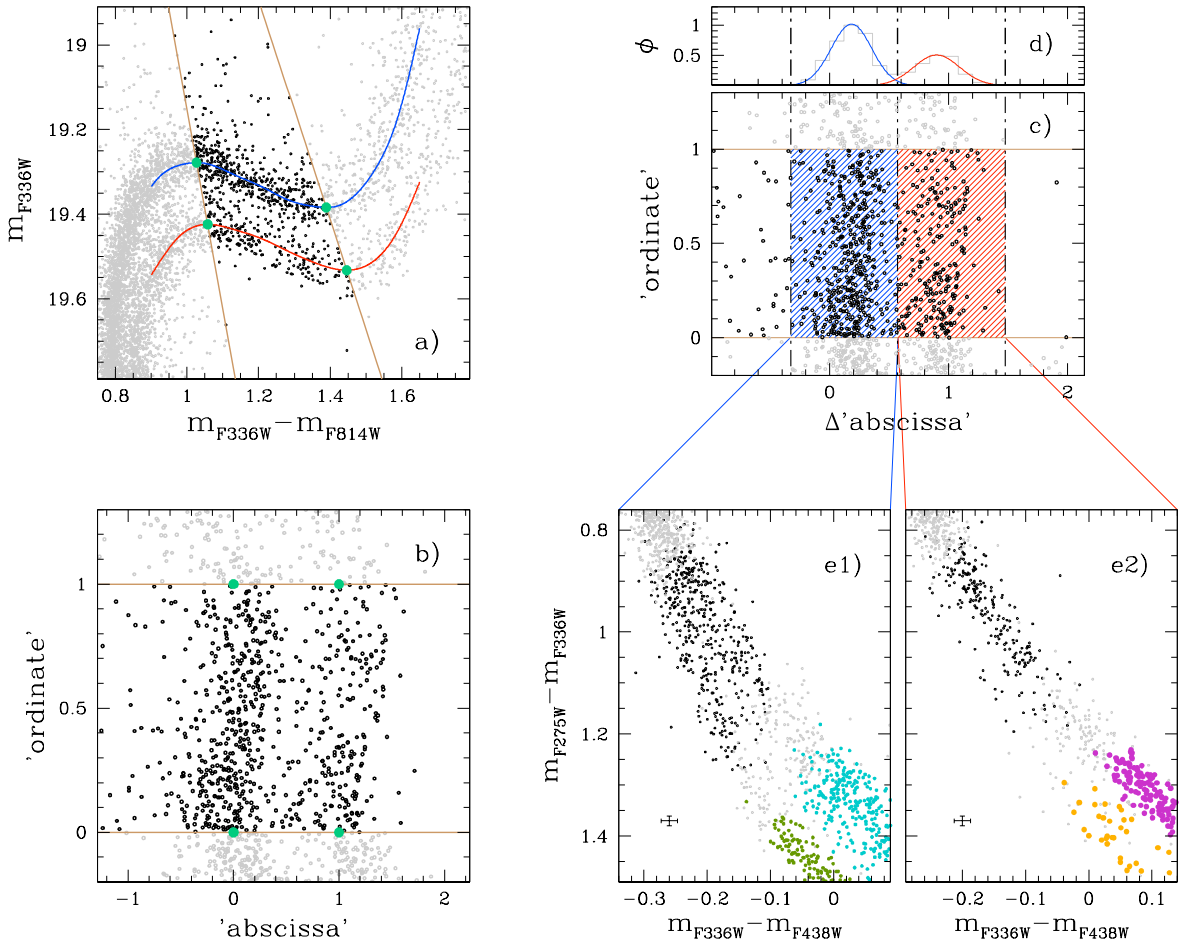

Figure 4.7: *Panel a):* $m_{\rm F336W}$ vs. $m_{\rm F336W} - m_{\rm F814W}$ CMD zoomed around the SGB. The blue and red lines indicate the fiducials of the canonical and anomalous SGB stars, respectively, while the aqua points represent their median brightest and faintest magnitude. The two brown lines delimit the considered SGB sample of stars. *Panel b):* 'ordinate' vs. 'abscissa' diagram of SGB stars, where lines, symbols, and colors have the same meaning as the previous panel (see text for details). *Panel c):* verticalized 'ordinate' vs. 'Δabscissa' diagram, where the three vertical black dot-dashed lines delimit the region within which canonical and anomalous stars lie, colored in blue and red, respectively. *Panel d):* histogram (in grey) and best-fit Gaussian functions of the two SGB populations (colored as in panel c)). *Panel e1) and e2):* $m_{\rm F275W} - m_{\rm F336W}$ vs. $m_{\rm F336W} - m_{\rm F438W}$ two-color diagrams for stars inside the blue and red regions identified in panel c), respectively (black dots). Blue and red lines connect these two regions to their respective two-color diagram. Grey points represent the MS and RGB prosecutions of each SGB (selected on the CMD). RGB stars tagged with the ChM presented in Section 4.3 are color-coded as in Figure 4.3. Error bars are shown in black.

anomalous stars, and correspond to the minimum of the bi-Gaussian function between its two peaks. With these three lines we define the two regions in panel c), colored in red and blue, that include the bulk of canonical and anomalous stars, respectively. Thanks

to these regions, we can now evaluate the fraction of the two populations by counting the number of stars within them and then correct these first estimates by contamination through AS tests (see Section 3.2.1), following the same procedure of Section 4.3. The fraction values are listed in Table 4.1 and are consistent within 1σ with the canonical and anomalous ratios inferred from RGB stars.

Finally, in panels e1) and e2) of Figure 4.7, we show the $m_{\rm F275W} - m_{\rm F336W}$ vs. $m_{\rm F336W} - m_{\rm F438W}$ two-color diagrams of the canonical and anomalous stars, respectively, highlighting in black the stars included in our sample of SGB stars defined in panel c) and in gray the MS and RGB stars that belong to the same branch (selected by eye). As demonstrated by Milone et al. (2012b), this two-color diagram is an efficient tool to separate populations with different carbon, nitrogen, and oxygen abundances since the F275W, F336W, and F438W filters are sensitive to the absorption bands of the OH, NH and CH, and CN molecules, respectively, thus being able to identify the same populations of $\Delta_{\rm CF275W,F336W,F438W}$ on the ChM. Indeed, stars with smaller $\Delta_{\rm CF275W,F336W,F438W}$ (hence larger carbon and oxygen and smaller nitrogen), have smaller $m_{\rm F336W} - m_{\rm F438W}$ and larger $m_{\rm F275W} - m_{\rm F336W}$ values than the stars with larger $\Delta_{\rm CF275W,F336W,F438W}$ (smaller carbon and oxygen and larger nitrogen). Populations with different carbon, nitrogen, and oxygen describe discrete sequences that run almost parallel (forming a V-like shape that merges towards the MS Turn-Off) on this two-color diagram. In both panels, each SGB splits into two sequences which are connected to two separated RGB sequences. By coloring the RGB stars tagged in Section 4.3, it becomes clear how the two sequences visible in panel e1) are the prosecution of the 1G and 2G populations while two anomalous SGB populations are the counterparts of the AI and AII stars. This finding confirms independently the quadrimodality observed in Section 4.3.

We repeat the whole procedure even in the ground-based catalog, starting with the U vs. $U-I$ CMD, to define a sample of SGB stars and calculate their fraction (reported in Table 4.1). However, with the available filters, it is not possible to identify among the SGB stars the counterparts of the 1G, 2G, AI, and AII populations in the outer part of the cluster.

4.5.2 The Main Sequence

In the MS regime, we explore the multiple populations that inhabit NGC 1851 by using the $m_{\rm F814W}$ vs $m_{\rm F336W} - m_{\rm F814W}$ CMD and excluding, from the *HST* catalog, the stars within the innermost 0.7 arcmin to consider only the stars with the most accurate photometry, avoiding the central area where the crowding effects affect the photometric quality. Indeed, while these effects are negligible for brighter stars, among the relatively faint MS stars (thus characterized by higher photometric error) they play a crucial role in allowing us to detect canonical and anomalous stars. We present in the left panel of Figure 4.8 the resulting CMD of the stars outside 0.7 arcmin, which form two distinguished upper MSs, which are clearly the prosecution of the two SGBs. Therefore, the blue and red MSs are populated by canonical and anomalous stars, respectively.

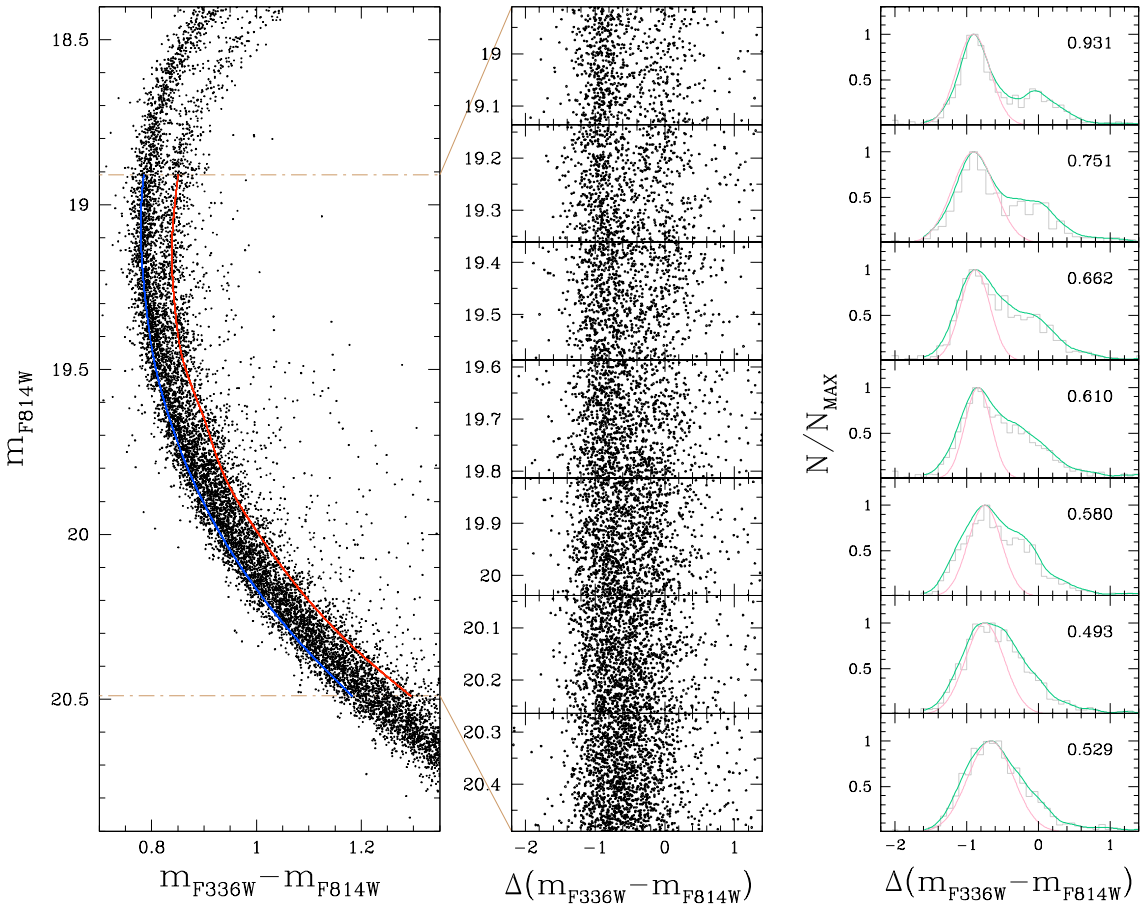

Figure 4.8: *Left panel:* $m_{\rm F814W}$ vs. $m_{\rm F336W} - m_{\rm F814W}$ CMD of stars in the *H*ST catalog outside the innermost 0.7 arcmin. Blue and red lines represent the boundaries used to verticalize the color distribution (see text for details), while the brown dot-dashed horizontal lines define the magnitude interval considered in our MS analysis. *Middle panels:* verticalized $\Delta(m_{\rm F336W} - m_{\rm F814W})$ distribution of MS stars in the $18.9 < m_{\rm F814W} < 20.5$ interval, divided into 7 magnitude bins. *Right panels:* $\Delta(m_{\rm F336W} - m_{\rm F814W})$ histogram (in grey) and kernel density (in aqua) distributions of MS stars in each bin defined by the middle panels. The pink line represents the distribution expected from observational errors.

To further investigate the double MS, we consider stars in the $18.9 < m_{\rm F814W} < 20.5$ mag interval and verticalized their color by following the procedure introduced in Section 4.3, deriving the $\Delta(m_{\rm F336W} - m_{\rm F814W})$ quantity. We plot the result in seven different magnitude bins in the middle panels, whereas in the right panels we show, for each bin, the histogram (in gray) and kernel density distribution (in aqua) of $\Delta(m_{\rm F336W} - m_{\rm F814W})$. We represent in pink the expected distribution of observational errors in each bin derived by performing AS tests, arbitrarily shifted at the maximum of the aqua distribution, and report the value of the BC (see Section 2.4) of the $\Delta(m_{\rm F336W} - m_{\rm F814W})$ distribution of stars.

Moving from brighter to fainter magnitudes, we notice: (i) the bimodality becomes

less and less clear-cut, as shown by the decrease of the BC, and (ii) the color distribution becomes narrower even if the error increases. These facts agree with two distinct MSs that merge going through fainter magnitudes, with a statistically significant bimodality (i.e., BC>0.555) down to ∼20.05 mag.

4.6 The Radial Distribution of Multiple Stellar Populations

In this Section, we investigate the radial distribution of the multiple populations harbored by NGC 1851. We start by focusing on the canonical and anomalous stars. We divide our FoV into five (four) circular regions that include the same number of RGB (SGB) stars. To each region, we apply the procedure described in Section 4.3 and 4.5 to measure the fraction of both populations along the RGB and SGB, respectively.

Figure 4.9 displays the radial trend of the fractions of canonical and anomalous stars, colored in blue and red, respectively. In both the RGB and SGB (upper and lower panels), the ratios are consistent within 1σ over the whole radial interval, from the center to the tidal radius, thus showing no differences in their radial distributions. We then perform a p-value test to infer the probability that the observed behavior is produced by a flat distribution. The derived p-values are 0.92 and 0.29 for RGB and SGB stars, respectively, which strongly support the flat-trend hypothesis (which would be disproved at values <0.05).

Since we divide our FoV into equal-number areas, the less-populated outermost cover an extended radial interval that includes the whole ground-based catalog region, from 1.5 arcmin to the tidal radius. To improve our resolution on the radial trend outside ∼2 arcmin, we consider the ground-based catalog only and divided it into two annulus that include an equal number of stars. The right panels represent the resulting distribution, in which again no significant radial variation is detected. In each Figure, the grey dot-dashed vertical lines represent the core, half-mass, and tidal radius of NGC 1851[8].

Then, we shift our focus to the canonical and anomalous subgroups of stars, taking different pairs of populations and deriving their fraction in equal-number bins. As done in Figure 4.9, we first consider the whole dataset and then the ground-based catalog only. Figure 4.10 displays our results. The left column represents the radial trend of the 2G, AI, and AII populations with respect to the 1G stars, revealing that the 2G and AII are more centrally concentrated than the 1G stars, while no significant differences emerge from the comparison with the AI population. In the central column, we present the radial distribution of the 2G and AII populations compared to the AI stars, from which both populations are more centrally concentrated than the AI. The comparison between 2G and AII stars (right panels) does not reveal any significant radial differences.

Finally, we measure the global fractions of the different populations spotted in NGC 1851. To do that, we convolve, from the center to the tidal radius, the radial trends illustrated

[8] According to Harris (1996, 2010 edition), the values of the core, half-mass, and tidal radius are 0.09, 0.51, and 6.52 arcmin, respectively. To study the cluster halo (see Section 4.7.1), we want to be as conservative as possible in selecting stars that lie outside the tidal radius. For that, we follow the approach by Marino et al. (2014b) and consider as our tidal radius the largest estimate present in literature, which is from Trager et al. (1993) and values 11.7 arcmin.

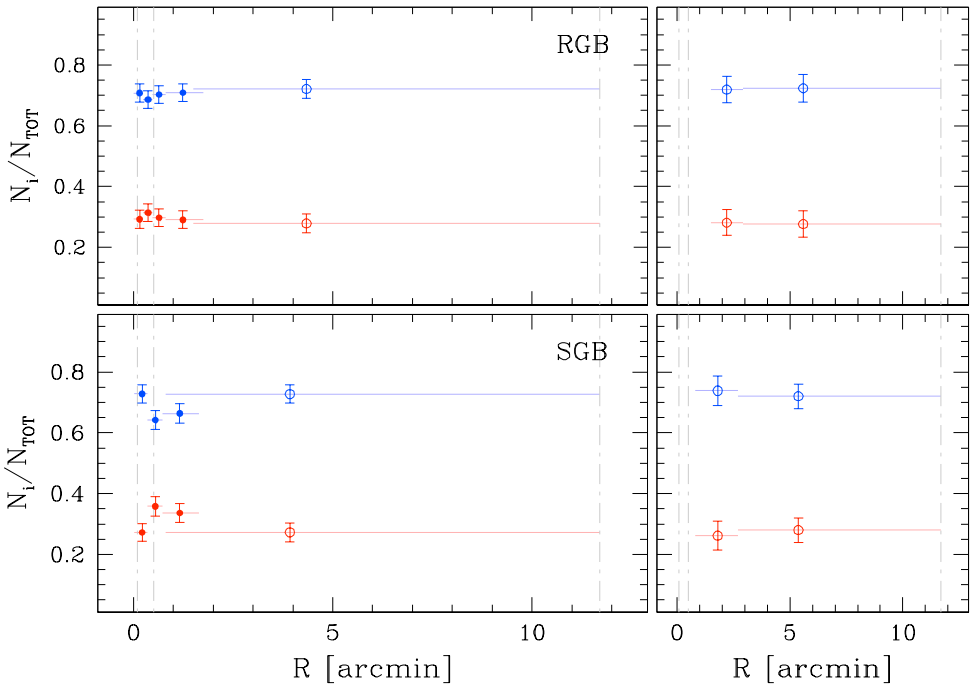

Figure 4.9: *Top panels:* radial trend of the canonical and anomalous RGB star fractions, colored in blue and red respectively, in the *H*ST and ground-based combined catalog (left panel) and the ground-based catalog only (right panel). Filled and open dots represent measurements obtained from the *H*ST and ground-based catalog, respectively. *Bottom panels:* same but for SGB stars. The three vertical dot-dashed lines highlight the core, half-mass, and tidal radius values.

in Figures 4.9 and 4.10 by the best-fit King profile (King, 1962) derived with the parameters from Harris (1996, 2010 edition) to account for the radial density distribution of the cluster stars. Our resulting fractions, derived from RGB stars, are listed in Table 4.1. To estimate the uncertainties, we simulate 10,000 radial distributions by scattering the observed trends by their errors. Then, we repeat the procedure to infer the global ratios for each sample and consider as our uncertainties the 68-th percentiles of the distribution of the global fraction obtained from all the simulations.

4.7 Spacial Distribution of the Canonical and Anomalous Populations

To investigate the 2D spacial distribution of the canonical and anomalous populations, we consider the RGB and SGB stars belonging to them according to our tagging performed in Sections 4.3 and 4.5. We apply the method described by Cordoni et al. (2020, see their Section 3), which is based on a 2D kernel smoothing of of their coordinates with respect to the center (ΔRA and ΔDEC).

The resulting smoothed distribution of canonical and anomalous stars are displayed in panels a1) and b1) of Figure 4.11, respectively. We then compute the isodensity

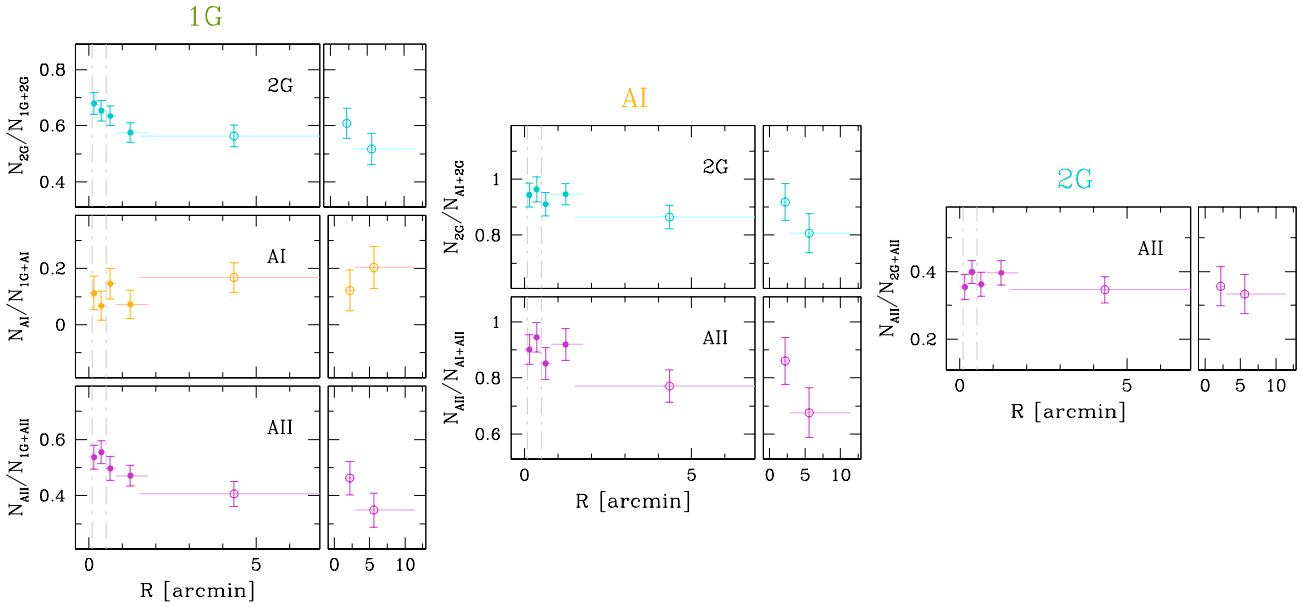

Figure 4.10: *Left panels:* radial distribution of the fraction of the 2G (top), AI (middle), and AII (bottom) populations with respect to the amount of 1G stars. *Middle panels:* same as the right panels but with the 2G and AII populations with respect to AI stars. *Right panel:* fraction of AII stars with respect to the 2G population.

contours of these two distributions and fit them with ellipses by means of least squares using the algorithm provided by Halir & Flusser (1998). Panels a2) and b2) illustrate the resulting best-fit ellipses, where we highlight their major axis (grey lines) and the averaged center of all the ellipses (aqua bullet). Panels a3) and a4) show a zoom of panels a1) and a2) in the innermost ∼1.5 arcmin, obtained by analyzing the *HST* data only, while, similarly, panels b3) and b4) represent a zoom of b1) and b2).

From this Figure, some differences arise between the two populations. Canonical stars exhibit a nearly circular distribution over the whole explored radial range, with a position angle showing high variability between different ellipses. Conversely, the anomalous population presents a circular distribution in the innermost area only, while moving towards larger radii it develops a degree of ellipticity[9] from ∼3.5 arcmin. Moreover, all the best-fitting ellipses share a similar orientation, with a position angle around 30° (measured east-wise from the north direction), in opposition to what is observed in canonical stars. In panel c), we plot the ellipticity of each ellipse in terms of their major axis, in which, outside 3.5 arcmin, the anomalous stars are larger at 1-σ level than the canonical ones. The uncertainty associated with the ellipticity is derived by simulating 1,000 random samples of stars with the same number and spatial distributions as canonical and anomalous stars. For each simulation, we measure the ellipticities with the same method used for real stars. The error associated with each measurement is derived as the 68th percentile of the distribution of the simulated ellipticities. Finally, we notice an overdensity of anomalous stars in the north-eastern quadrant, forming an elongation in both the

[9] The ellipticity is defined as $1 - \frac{b}{a}$, where a and b are the major and minor axis, respectively.

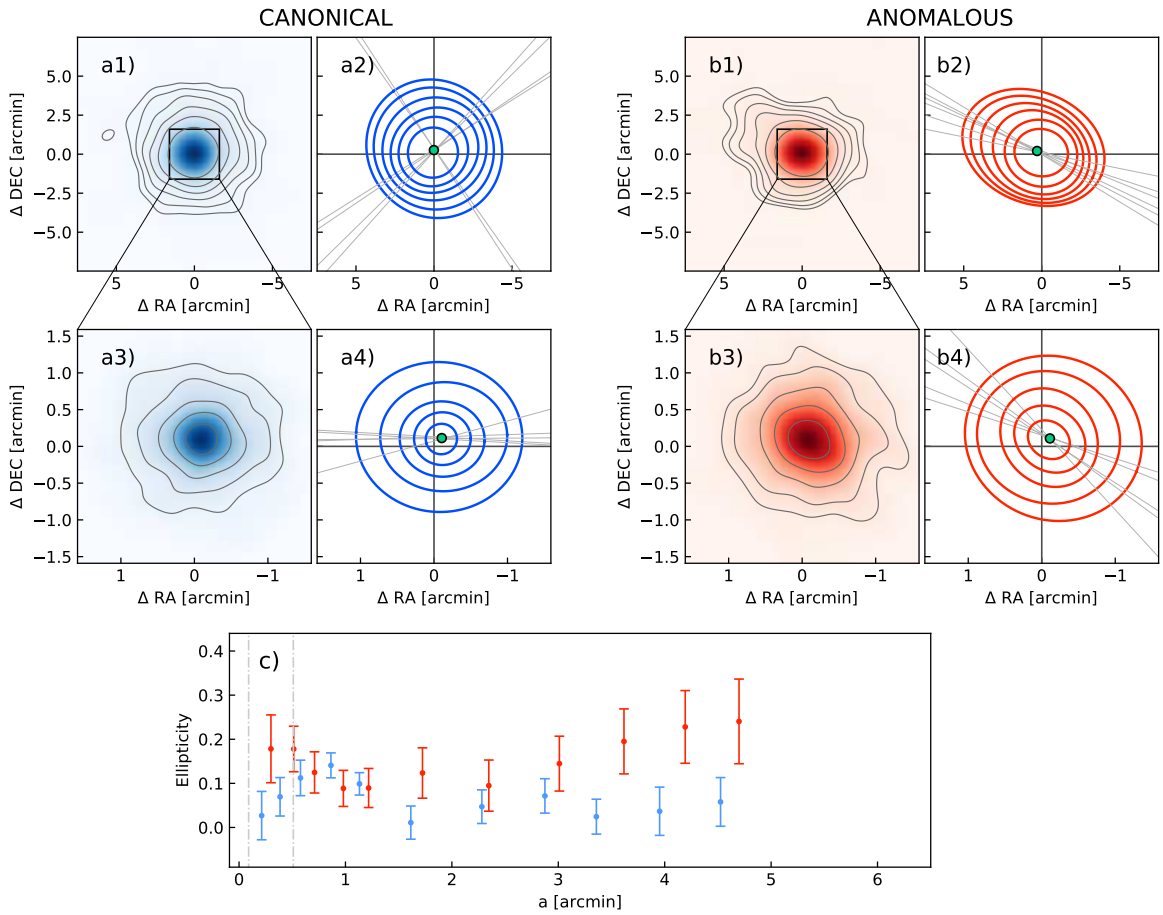

Figure 4.11: *Panels a1) and b1):* spatial distribution of canonical and anomalous stars in the ground FoV, represented in blue and red color scale, respectively. Dark grey lines are the isodensity contours. *Panels a2) and b2):* best-fit ellipses of canonical (in blue) and anomalous (in red) isodensity lines. Grey straight lines represent the major-axis direction of each ellipse, while aqua dots display the averaged ellipse centers. *Panels a3), b3), a4), and b4):* same as panels a1), b1), a2), and b2) but for stars in the *HST* FoV (within the black boxes in panels a1) and a2)). *Panel c):* Ellipticity of canonical and anomalous stars with respect to the major axis of their isodensity contours best-fit ellipses. The two dot-dashed lines represent the core and the half-mass radius.

isodensity and the best-fitting ellipses plots around $(\Delta RA, \Delta DEC) \sim (3.5, 3.0)$. As a consequence, the fraction of canonical stars in this quadrant (by considering the ground-based catalog only) is significantly larger than the average value, being 0.38±0.05 and 0.28±0.03, respectively.

We also consider the 2D spatial distribution of the canonical 1G and 2G populations in the RGB only, because in the SGB their separation is not clear enough for a reliable quantitative analysis. This leads to having a poor number of stars and poor statistics, hence large uncertainties in our fitting process. That said, we still point out that we detect no significant differences between 1G and 2G stellar distributions, obtaining ellipticies of 0.128±0.069 and 0.086±0.062 for 1G and 2G stars, respectively.

4.7.1 Stars outside the tidal radius

An intriguing feature of NGC 1851 consists in the presence of an extended halo of stars that surrounds the cluster up to several times the tidal radius, reaching a distance of about ∼500 pc as discovered by Olszewski et al. (2009) and further explored by Carballo-Bello et al. (2018); Kuzma et al. (2018); Ibata et al. (2021).

By exploiting the recent Gaia DR3, we explore the halo population of NGC 1851. To do that, we need to identify probable cluster members in the Gaia catalog. We apply to the Gaia photometry the following criteria to isolate them: (i) we consider only sources with G <20 mag to exclude the ones with low signal-to-noise ratio. (ii) We use the `As_gof_al`, the `RUWE` (see Section 2.2), and the parallax diagnostics provided in the Gaia catalog to select only the sources with high-quality photometry. (iii) We analyze the Gaia proper motions and select the stars within a radius of 0.9 mas yr^{-1} centered on the average proper motion. (iv) In the G vs. $G_{\rm BP} - G_{\rm RP}$ CMD, we select by eye the stars that lie on the MS-SGB-RGB-HB evolutionary sequence, hence that are reasonable cluster members. Panel a1) of Figure 4.12 represents the G vs. $G_{\rm BP} - G_{\rm RP}$ CMD, where we color in gray the stars that fulfill (i), (ii), and (iii), while the ones in the halo (i.e., outside the tidal radius) that also satisfy (iv) are displayed as black points. Azure crosses indicate the extra-tidal sources that do not belong to the cluster according to the CMD selection criterion.

Up to ∼80 arcmin from the center (∼260 pc), we can still detect probable members of NGC 1851 even after applying our strict selection criteria, thus confirming the presence of stars outside the tidal radius. Moreover -for some of the detected cluster stars- radial velocity measurements are available in the Gaia catalog, which can serve as further diagnostics for cluster membership. Indeed, based on spectroscopic studies (Sollima et al., 2012; Marino et al., 2014b), we expect that the stars of NGC 1851 have a radial velocity consistent with the cluster average motion, hence we consider as members of the stars with radial velocities between 300 and 350 km s^{-1}. The ones that, beyond respecting the aforementioned selection criteria, also fulfill the radial velocity criteria are encircled in aqua and can be observed up to a radius of ∼38 arcmin.

We then measured the contamination of field stars with similar proper motions and CMD position than cluster members that affect our halo stars sample. To do that, we consider an annulus with the same on-sky area of the FoV analyzed in panel a1) located further away from the cluster center, covering a radial range from ∼140 to 160 arcmin, where we expect a negligible contribution of cluster stars in the Gaia catalog. We show the CMD of this field in panel a2), where the color coding of stars is assigned by following the same criteria as panel a1). From the tidal radius up to 80 arcmin, we find 140 halo stars and 1,256 field stars. In the outer annulus, the number of field stars is comparable (1,401), while only 35 stars share the same colors, magnitude, and proper motions as cluster members. This finding demonstrates that our selection of halo members is not consistent with being made by field stars only (as in the outer annulus). Specifically, by assuming a uniform distribution in the considered sky area, we expect

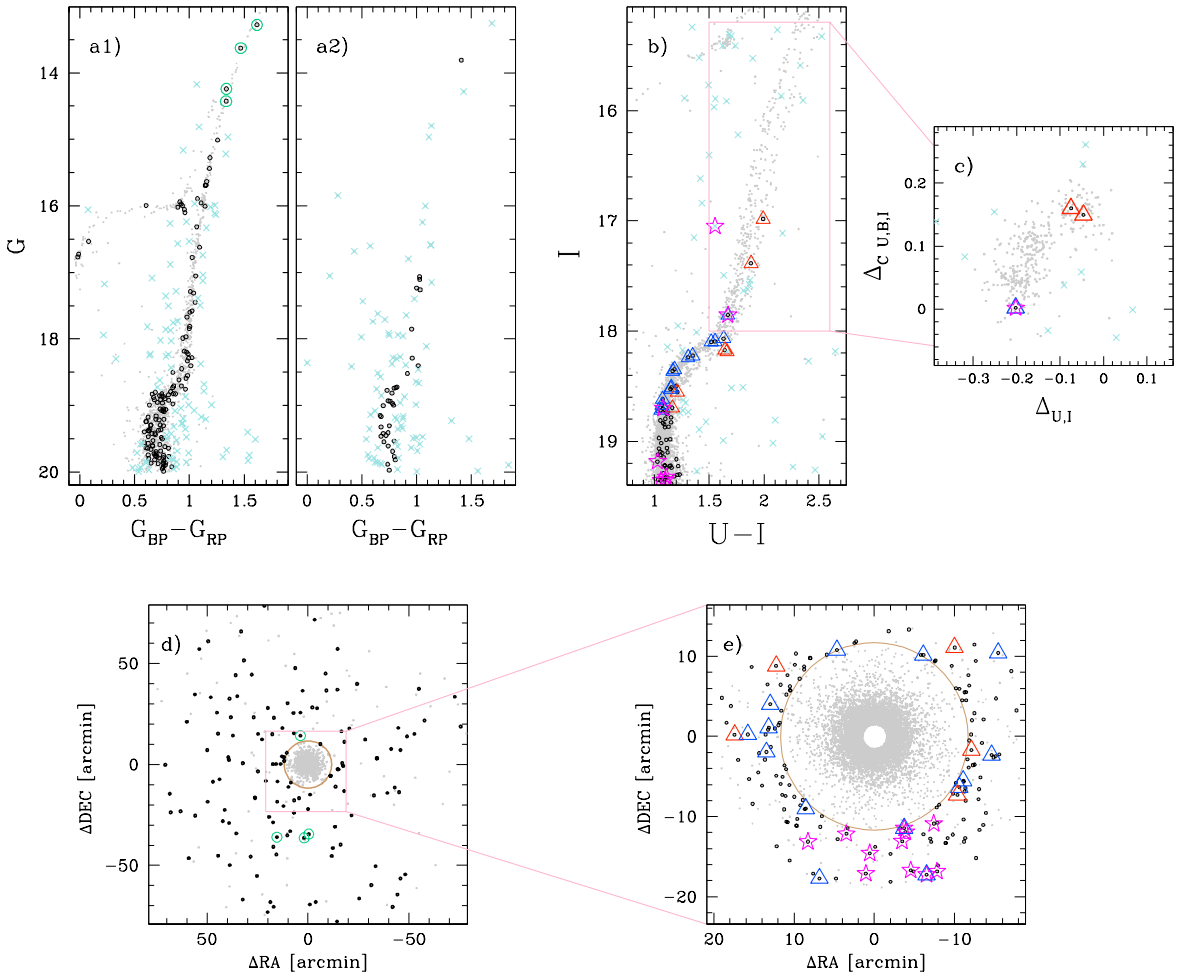

Figure 4.12: *Panel a1) and a2):* Gaia G vs. $G_{\rm BP} - G_{\rm RP}$ CMD of stars within 80 arcmin from the cluster center and from the FoV dominated by field stars, respectively. Stars that pass the photometric diagnostics and the proper motion selection are marked with gray points. Black points and azure crosses represent the extratidal stars that are consistent with belonging to NGC 1851 and to the field according to the CMD selection, respectively. Stars with radial velocity measurements consistent with the cluster motion are encircled in aqua (see text for details). *Panel b):* I vs. $U - I$ CMD from ground-based photometry. Grey and black points and azure crosses have the same meaning than in panel a1) and a2). Halo canonical and anomalous stars are displayed with blue and red triangles, respectively, while magenta starred symbols display the stars in common with the work by Marino et al. (2014b). *Panel c):* $\Delta_{\rm CU,B,I}$ vs. $\Delta_{\rm U,I}$ ChM for RGB stars within the pink box in panel b). *Panel d):* ΔDEC vs. ΔRA position of stars in the Gaia FoV, color-coded as in panel a1) and a2). *Panel e):* zoom of the Gaia ΔDEC vs. ΔRA diagram within the pink rectangle representing the position of stars in the ground-based FoV. The brown circle in panels d) and e) indicates the tidal radius.

that the contamination from field stars is about 25% (35/140).

The FoV of the ground-based catalog used in this Chapter reaches areas beyond the

tidal radius, hence its UBVRI photometry allows us to investigate the canonical and anomalous populations in the inner part of the cluster halo. Specifically, the catalog of well-measured stars with available multi-band photometry is extended up to ∼20 arcmin in east and south directions and up to about 13 and 18 arcmin towards north and west, respectively.

A similar investigation was performed by Marino et al. (2014b) through spectroscopy of stars located in the southern area of the halo. They measured s-process elements' abundances to disentangle canonical and anomalous stars, finding 15 probable cluster members (based on metallicity and radial velocity), all sharing content of s-process elements consistent with them being canonical stars only. In panel b) of Figure 4.12, we show the I vs. $U-I$ CMD, where black points and azure crosses, similarly to panels a1) and a2), represent the extratidal stars that we included and excluded in our sample of cluster stars, respectively, based on their CMD position. Stars in common with the sample by Marino and collaborators that are well measured in the ground-based catalog are indicated with magenta starred symbols. Blue and red triangles indicate the candidate canonical and anomalous halo stars in the SGB and the RGB. The former are identified by their position on the I vs. $U-I$ CMD, while the latter through the $\Delta_{\rm CU.B.I}$ vs. $\Delta_{\rm U,I}$ ChM (in panel c)), derived as explained in Section 4.3, extended down to $I\sim 18$. In the ChM plane, we identify three stars as reliable RGB candidates, among which one of them is a probable canonical star, consistent with belonging to the 1G population, and the other two are likely to be anomalous AII stars. We show in panel d) the on-sky coordinates relative to the cluster center, ΔRA and ΔDEC, of the stars portrayed in panel a1), highlighting the halo members identified through Gaia photometry. Finally, panel e) presents a zoom of panel d) in the area covered by well-measured stars in the Stetson et al. (2019) ground-based dataset. Here, NGC 1851 stars are color-coded as in panels b) and c). In the southern direction, we do not detect anomalous stars below $\Delta DEC\sim 10$ arcmin, in agreement with the results from Marino et al. (2014b). Notably, two stars were tagged by both photometry and spectroscopy, which gave consistent results on their nature. Along the other directions, we identify five anomalous stars, whereas the total 14 canonical halo stars are distributed evenly in the analyzed field.

These results, even though based on a relatively low number of stars, suggest different 2D distributions between canonical and anomalous stars in the halo, with a lack of the latter in the south and southeast directions. Noticeably, this is qualitatively consistent with what is found in Figure 4.11, where the anomalous population appears to be distributed unevenly, showing a smaller extension towards these two directions.

4.8 Summary and Conclusions

By exploiting photometry from *H*ST, ground-based facilities, and Gaia, we explored and characterized the stellar populations of the Type II GC NGC 1851. Thanks to our dataset, the multiple populations have been extensively analyzed throughout the cluster

area, from the center to its outskirts. The following summarized the results:

- We derive ChMs with multi-band *H*ST and ground-based photometry, which both reveal that canonical and anomalous RGB stars are not consistent with a single stellar population. The canonical population comprises the s-poor stars while the anomalous population hosts the s-rich stars discovered by Yong et al. (2008). These two populations can be followed continuously among fainter stars, in the SGB and the upper MS, where they merge in one at around one F814W magnitude below the MS Turn-Off.

- Based on the ChMs, we identify two sub-populations within both the canonical and anomalous stars. The former hosts the 1G and 2G populations that can be observed in all the old and massive Type I and Type II GCs. These two populations, as expected, differ in their helium, carbon, nitrogen, and oxygen abundances. Their extension on the ChMs reveals that both 1G and 2G are not consistent with being chemically homogeneous. Similarly, among anomalous stars, we identify two separate populations, dubbed AI and AII, with different light-elements abundances.

- We constrain the difference in total CNO between canonical and anomalous stars by comparing our photometry with synthetic spectra characterized by different content of carbon, nitrogen, and oxygen. We find that anomalous stars share the same carbon content as the canonical ones, while they are enhanced in nitrogen by $\sim$1 dex and slightly depleted in oxygen (even though the latter is also consistent with a nil variation within errorbars). Hence, anomalous stars are enhanced in the overall C+N+O abundance with respect to the canonical population. Our results based on multi-band photometry confirm the findings by Yong et al. (2015) based on high-resolution spectra.

- We investigate the radial distribution of the stellar populations identified in NGC 1851. We find no significant differences between the fraction of canonical and anomalous stars by analyzing separately different radial intervals from the center up to the tidal radius. Conversely, we detect radial differences between the sub-populations of both groups of stars. Indeed, the most chemically extreme populations, 2G and AII, are more centrally concentrated than the 1G and AI stars, respectively. We do not find any radial differences when comparing 1G and AI and 2G and AII.

- By combining the radial trend information up to the tidal radius with King's density profiles, we estimate the global fraction of each population, reported in Table 4.2. The global fractions of the four disentangled populations to the total number of stars value $f^{\rm G}_{\rm 1G} = 0.229 \pm 0.030$, $f^{\rm G}_{\rm 2G} = 0.474 \pm 0.030$, $f^{\rm G}_{\rm AI} = 0.027 \pm 0.030$, and $f^{\rm G}_{\rm AII} = 0.270 \pm 0.030$.

- Intriguingly, canonical and anomalous stars exhibit different 2D spatial distributions. While the isodensity contours of canonical stars present a circular-like shape, with ellipticity $\sim$0.1, the anomalous stars density contours develop an elliptical shape

outside ∼3.5 arcmin, reaching an average ellipticity of ∼0.3, with its best-fit ellipses having their major axis oriented along the north-east/south-west direction. Moreover, we detect the presence of an overdensity of anomalous stars in the northeast direction, where their fraction increase of about 10% than the average value which, as shown in Section 4.7, is significant at a 2σ level.

By combining the information from the radial and spatial distribution, we find that the overall fractions of canonical and anomalous stars do not vary with the distance from the cluster's center, as found by Milone et al. (2009b), but the uneven spatial distribution between the two introduces local gradients. In particular, their drop in the south/southeast outer field of the cluster may explain the results by Zoccali et al. (2009), who detected a decrease in the anomalous fraction by studying a similar FoV.

- We identify halo stars around NGC 1851, located several times farther than its tidal radius, employing Gaia photometry, thus confirming previous results (Olszewski et al., 2009; Sollima et al., 2012; Marino et al., 2014b; Kuzma et al., 2018). We detect cluster members up to about 80 arcmin (∼260 pc) from the cluster center. We spot 14 canonical and five anomalous halo stars by considering multi-band ground-based photometry, which covers the inner part of the halo (from ∼12 to 20 arcmin). Our tagging corroborates the findings by Marino et al. (2014b), who found that anomalous extratidal stars in the southern area of the halo nearly disappear but, according to our analysis, are still visible along the other directions. Since the available multi-band photometry necessary to disentangle canonical and anomalous stars reaches radial distance up to 20 arcmin and the halo is extended up to (at least) 80 arcmin, further analysis extended to higher radii is mandatory to shed light on this phenomenon.

We conclude by providing some considerations, although strictly qualitative, about the formation of anomalous stars in Type II GCs, comparing our results with the two possible formation scenarios for these objects presented in Section 1.3.

In the idea proposed by (Carretta et al., 2010; Bekki & Tsujimoto, 2016), anomalous are the product of a merging between (at least) two initially separated GCs. This idea naturally accounts for the presence of two anomalous populations, AI and AII, which would be the first and second generation of a distinct GC. Moreover, the 1G-2G and AI-AII patterns also share similar relative chemical differences and radial distribution, which would indicate them being produced by the same mechanisms. On the other hand, the large C+N+O difference observed between canonical and anomalous stars in NGC 1851 is not straightforward in this scenario, which would require excessively long timescales to produce. This could be possible by introducing the ad-hoc assumption that new stars can form from AGB ejecta without mixing so well with the medium (see the discussion in Bekki & Tsujimoto, 2016, Section 4.2). Finally, we notice how AI stars would have a rather extreme chemical composition for being first-generation stars, having intermediate [Na/Fe] and [O/Fe] between 1G and 2G stars, and it is not clear if

the chemical evolution of a host dwarf galaxy could account, in the required timescales, to such chemical differences.

According to the scenario proposed by D'Antona et al. (2016) and D'Ercole et al. (2016), NGC 1851 experienced a prolonged star formation compared to Type I GCs, undergoing the effect of additional polluters. In this case, the total CNO difference and the s-process abundances spread would be introduced by the winds ejected from $\sim$3.5$-$4 $M_{\odot}$ AGB that contributed in the formation of anomalous stars. The lack of a significant [Fe/H] variations, in this scenario, would be the sign of a negligible delayed SNe contribution in the medium that produced AI and AII stars. Moreover, the light-elements abundances spread among anomalous stars would be introduced by inhomogeneous mixing between different ejecta (D'Ercole et al., 2016, see their Section 4.2).

Both scenarios agree on the possibility that Type II GCs may be remnants of a larger structure, like a dwarf galaxy. The presence of a halo of stars more extended than the tidal radius of NGC 1851 could be a sign that this cluster was originally a larger structure. An extensive study of the halo, aimed at identifying the populations that compose it, will provide additional constraints on the origin of NGC 1851 and, possibly, of other Type II GCs.

Our results provide new constraints and challenges to the Type II GC formation scenarios. To unveil the origin of these structures further works based on investigating anomalous stars in a wider sample of clusters, combining photometry, spectroscopy, and theoretical modeling, are mandatory.

CHAPTER 5

Conclusions

In this thesis, I presented the published studies to which I dedicated my efforts -as the first author- during the three years of my Ph.D. The results of the three projects presented in Capther 2, 3, and 4 are all focused on different aspects of the multiple populations phenomenon and share the goal of providing new ingredients to unveil the nature of this enigmatic phenomenon. As anticipated in Chapter 1, these results will help in the long-term task of building a comprehensive picture of the history of GCs, both by solidifying the current knowledge on fundamental properties of multiple populations and by producing among the first works to address some of the new questions related to the phenomenon, which are going to polarize the debate in the coming years/decades.

The thesis defines several photometric tools useful to gain fresh information on GC's stars, which will be pivotal for future investigations. The following summarizes the results obtained in the three studies that constitute the body of this document:

- **Multiple Populations in the red HB.** In this work, presented in Chapter 2, I showed how multiband *HST* and ground-based photometry can separate the 1G and 2G populations among red HB and red clump stars in GCs, providing new tools for the investigation of the phenomenon. This study brings independent confirmation of results inferred from RGB stars. Moreover, in three clusters, namely NGC 5927, NGC 6304, and NGC 6441, this approach allowed spotting the multiple populations with detail not reachable through the available RGB photometry, granting the first-ever measures of their 1G-2G fractions.

  Particularly intriguing is the possibility of applying this method to extragalactic clusters, as done in this work for NGC 416 in the SMC and NGC 1978 in the LMC, for which we detected multiple populations and measured their populations' frac-

tions. This study is fundamental to exploring the connection between the multiple populations phenomenon and the host galaxy. Indeed, while it is well established that the incidence of 2G stars grows with the GC mass (see Section 2.3), it is not clear which other agents influence the chemical inhomogeneities.

Our finding that the fraction of 1G stars in the two extragalactic clusters is higher than the same quantity among Galactic GCs with similar mass suggests that the formation environment plays a role in shaping the observed phenomenon. A possible scenario to justify the observation foresees that 1G stars dominate GCs at their formation, to then being stripped from the interaction with the host galaxy during their lifetime. The studied Magellanic Clouds GCs are younger than the Galactic ones and lie within less massive galaxies than the Milky Way, thus suggesting that they had less time to lose 1G stars and lived in an environment less efficient to strip their 1G stars. This would also imply that 2G stars were more centrally concentrated than 1G at their formation, such that the outskirts stars that escape the clusters are 1G stars only.

- **Multiple Populations among VLM stars.** The study presented in Chapter 3 represents decisive evidence of the primordial nature of the multiple populations phenomenon, having detected their presence among fully convective stars in the most numerous sample of GCs with suitable archive NIR observations to date. We proved how several characteristics of the multiple populations are still present among stars fainter than the MS knee, even when considering just the oxygen variation (which NIR passbands are sensitive to). This unique dataset, combined with information from UV and optical photometry, opens the possibility of measuring one of the fundamental parameters to describe a stellar population, the MF, for the chemically different stars within GCs along basically the whole MS, from the MS turn-off ($\sim$0.8 $\mathcal{M}_{\odot}$) down to $\sim$0.2 $\mathcal{M}_{\odot}$. With the current archive observations, this is possible for NGC 2808, and M 4 since images in UV, optical, and NIR are available in the same FoV.

  Our detection of no slope variations among low-mass stars constitutes a crucial constraint to any theoretical scenario that aims to explain the mechanisms that produced multiple populations. In particular, this result is in disagreement with the prediction that 2G stars formed by accreting material through a Bondi-Hoyle-like mechanism, thus suggesting that if they formed by accreting material rather than in different stellar generation (see Section 1.2), this process should not strongly depend on stellar mass. The lack of slope differences also suggests that multiple populations may formed with the same IMF (see the discussion in Section 3.8), thus implying that, in a scenario where 2G stars formed in a more centrally concentrated environment, the shape of the IMF is not influenced by stellar density.

- **The anomalous GC NGC 1851.** Chapter 4 describes our work on NGC 1851, one of the so-called anomalous (or Type II) GCs, which, beyond the typical 1G and 2G, hosts a further group of stars. We performed an unprecedented in-depth inves-

tigation on its populations, especially on anomalous stars, combining multi-band photometry from different facilities. This detail allowed us to detect anomalous stars from the RGB tip down to the MS, revealing that they exhibit similar light-elements inhomogeneities to 1G-2G patterns.

The comparison between the new ChMs introduced in this Chapter and synthetic spectra revealed that the anomalous are enhanced in total CNO with respect to the canonical stars. Specifically, nitrogen is the element that drives the difference, with carbon and oxygen showing little-to-nil variations. The spatial analysis revealed that, while no radial differences between canonical and anomalous stars are present, there are significant variations in their 2D distribution, with the latter developing an elliptical shape outside about three arcmin, thus introducing local gradients in the fraction of these two groups of stars. By combining ground-based and Gaia photometry and spectroscopy from the literature, we provided an in-depth characterization of the halo that surrounds NGC 1851, identifying 14 and five canonical and anomalous stars, respectively, and corroborating the idea that the latter are not distributed uniformly, since they disappear in the southern area of the halo.

These results provide the first proving ground for the two principal scenarios that aim at justifying the existence of Type II GCs (see the discussion in Section 1.3). The idea of them originating from the merging of two initially separated GCs is supported by the presence of qualitatively similar star-to-star variations between the canonical and anomalous populations, with the AI and AII being the first- and second-generation stars of the latter. The observation of the AII being more centrally concentrated than the AI fits well this hypothesis since it is a typical behavior observed among multiple-population patterns. However, as discussed in Section 4.8, the comparison between the chemical composition of the bulk of anomalous and canonical stars raises few concerns on this possibility since it is not well known yet if the chemical evolution of dwarf galaxies can account for the observed patterns, such as the total C+N+O variation.

On the other hand, the hypothesis that NGC 1851 experienced a prolonged star formation, such that anomalous stars would consist in stellar generations subsequent to the 1G and 2G stars, very well fits the observed chemical differences between the bulk of canonical and anomalous stars. In principle, this idea could also account for the star-to-star variations within anomalous stars, even though more modeling is necessary to explore in detail this possibility, in particular on how the observed AI-AII radial differences could originate.

The task of unveiling the mystery of multiple populations is bound to play a crucial role in the following decades of stellar astrophysics since massive efforts, both on the observational and theoretical sides, are still required. In particular, several key points will polarize future research and debate, likely serving as cornerstones to solve this riddle, and therefore need to be addressed in the coming years. Here, I present the future task of observational astrophysics that will benefit from the results and the techniques

introduced in this thesis:

- **1G spread.** The unexpected detection of a spread among 1G stars recently opened new exciting questions about the nature of GCs. As detailed in Section 1.1, [Fe/H] and/or helium variations are thought to be the main responsible. Red HB stars are fertile ground to detect the phenomenon, as shown in Chapter 2. Indeed, the collection of two-color diagrams presented in Figure 2.4 can highlight its presence and variations among different clusters, with an accuracy that is not always reachable through other evolutionary phases (like for NGC 5927, NGC 6304, and NGC 6441).

- **Reaching further galaxies.** At the moment, only the closest galaxies have been explored in the multiple populations context. This is because it is very challenging to observe stars with high precision that lie far away from our Galaxy. Extending the sample of explored galaxies is pivotal in shedding light on the role of the environment in which GCs formed and evolved, and to evaluate the impact that other factors (like cluster age) may or may not had on the phenomenon. The new set of tools introduced to spot multiple populations in the red HB can be particularly advantageous in metal-rich GCs (that exhibit this feature) where the necessary high-accuracy RGB photometry would take a large amount of telescope time. On the other hand, red HB and red clump stars are commonly brighter than RGB stars, thus displaying a smaller photometric error with the same observing effort[10]. Thereupon, this method has the potential of being very profitable when analyzing clusters close to the Galactic bulge, like the three from our sample with no available RGB fraction measurements, and far away GCs, like the metal-rich ones that populate M31.

- **GCs in the Galactic bulge.** Clusters that lie within (or very close to) the Galactic bulge are characterized by heavy contamination and, as a consequence, less quality in their observational data. Indeed, the three clusters studied in Chapter 2 for which no RGB-based measurement of the 1G-2G fraction are the ones closest to the Milky Way bulge. Since the GCs in the bulge area are typically metal-rich, the benefits of red HB photometry explained in the previous point for M31 GCs are still valid in these conditions.

  However, the high dust contamination present in the bulge could degrade the UV photometry in the innermost clusters. To avoid the issue and minimize extinction, NIR observations are mandatory. In this context, the work presented in Chapter 3 proved that these kinds of observations are also effective in detecting multiple populations, thus opening the possibility of studying the metal-rich and poorly-explored GCs population in the innermost regions of the Milky Way.

- **The VLM stars realm.** The multiple populations phenomenon among M-dwarf stars can only be observed with infrared observations. Even though they constitute the preponderance of a cluster's stellar population, they are relatively poorly

[10] The brightest part of the RGB, approaching the tip, is more luminous than these stars. However, it is less populated than the lowest part of the RGB, and the separation between 1G and 2G stars is typically less clear.

studied in this context due to the observational challenges related to their faintness. Chapter 3 presents the widest study of multiple populations among VLM stars, highlighting their crucial role in studying the MF of these groups of stars and disentangling between different formation scenarios. However, only nine GCs are available for observation suited for spotting oxygen variation in this evolutionary phase, and only for two of them it is currently possible to derive the MF along a wide stellar mass range. The work done in this thesis constitutes one of the first steps in this field, and extensive work in the near future is mandatory to extend the number of analyzed GCs with these tools.

Finally, this work acts as a trailblazer for a future where the *J*ames Webb Space Telescope (JWST) will dominate the NIR studies of GCs, in particular by further improving the quality of VLM stars photometry.

- **The origin of Type II GCs.** Understanding why a fraction of Galactic GCs present an extra population with chemical peculiarities (see Section 1.3) is a crucial step to comprehend the origin of multiple populations in GCs. In particular, massive work is needed to test the two main scenarios and clarify their implications in galaxy formation and assembly. Our work on NGC 1851 represents one of the first attempts to provide a comprehensive description of the observational characteristics of anomalous stars, combining photometry, spectroscopy, and synthetic spectra, and comparing observations with theoretical works. Our results point out that both the considered scenarios are potentially appealing, but further modeling tuned around these results is necessary to draw firm conclusions. On the observational side, it is mandatory to extend our approach to the other known Galactic Type II GCs beyond NGC 1851 and to hunt for similar structures in other galaxies (like M31) to clarify their relation with disrupted dwarf galaxies.

All these topics constitute the crucial steps for understanding the origin of GCs and their multiple populations that we can make through photometry, which is the protagonist of this thesis. Clearly, the complexity of this phenomenon highlights the necessity and the importance of an interplay between the investigation of the several features of the multiple populations, combining photometry with all the information that stellar astrophysics can currently provide, such as spectroscopy, kinematics, and stellar population modeling. Only by connecting the different pieces of the puzzle the final picture can reveal itself.

List of Figures

List of Tables

Bibliography

Afşar M., et al., 2018, ApJ, 865, 44

Allard F., Hauschildt P. H., 1995, ApJ, 445, 433

Anderson J., et al., 2008, AJ, 135, 2055

Anderson J., Piotto G., King I. R., Bedin L. R., Guhathakurta P., 2009, ApJ, 697, L58

Ballesteros-Paredes J., Hartmann L. W., Pérez-Goytia N., Kuznetsova A., 2015, MNRAS, 452, 566

Bastian N., Lardo C., 2018, ARA&A, 56, 83

Bastian N., Lamers H. J. G. L. M., de Mink S. E., Longmore S. N., Goodwin S. P., Gieles M., 2013, MNRAS, 436, 2398

Baumgardt H., Hilker M., 2018, MNRAS, 478, 1520

Bedin L. R., Piotto G., Anderson J., Cassisi S., King I. R., Momany Y., Carraro G., 2004, ApJ, 605, L125

Bedin L. R., Cassisi S., Castelli F., Piotto G., Anderson J., Salaris M., Momany Y., Pietrinferni A., 2005, MNRAS, 357, 1038

Bedin L. R., King I. R., Anderson J., Piotto G., Salaris M., Cassisi S., Serenelli A., 2008, ApJ, 678, 1279

Behr B. B., 2003, ApJS, 149, 67

Bekki K., Tsujimoto T., 2016, ApJ, 831, 70

Bekki K., Yong D., 2012, MNRAS, 419, 2063

Bellazzini M., et al., 2008, AJ, 136, 1147

Bellini A., Bedin L. R., 2009, PASP, 121, 1419

Bellini A., Anderson J., Bedin L. R., 2011, PASP, 123, 622

Bellini A., et al., 2013, ApJ, 765, 32

Bellini A., et al., 2015, ApJ, 810, L13

Bellini A., Anderson J., Bedin L. R., King I. R., van der Marel R. P., Piotto G., Cool A., 2017, ApJ, 842, 6

Bellini A., et al., 2018, ApJ, 853, 86

Boberg O. M., Gerber J. M., Friel E. D., Martell S., Briley M. M., Morrison H. L., 2016, AJ, 151, 127

Bragaglia A., Gratton R. G., Carretta E., D'Orazi V., Sneden C., Lucatello S., 2012, A&A, 548, A122

Bragaglia A., Sneden C., Carretta E., Gratton R. G., Lucatello S., Bernath P. F., Brooke J. S. A., Ram R. S., 2014, ApJ, 796, 68

Briley M. M., Cohen J. G., Stetson P. B., 2004, AJ, 127, 1579

Brown J. A., Wallerstein G., Oke J. B., 1991, AJ, 101, 1693

Brown J. A., Wallerstein G., Gonzalez G., 1999, AJ, 118, 1245

Cadelano M., Dalessandro E., Salaris M., Bastian N., Mucciarelli A., Saracino S., Martocchia S., Cabrera-Ziri I., 2022, ApJ, 924, L2

Calura F., D'Ercole A., Vesperini E., Vanzella E., Sollima A., 2019, MNRAS, 489, 3269

Campbell S. W., et al., 2012, ApJ, 761, L2

Carballo-Bello J. A., Martínez-Delgado D., Navarrete C., Catelan M., Muñoz R. R., Antoja T., Sollima A., 2018, MNRAS, 474, 683

Carretta E., 2015, ApJ, 810, 148

Carretta E., et al., 2009a, A&A, 505, 117

Carretta E., Bragaglia A., Gratton R., Lucatello S., 2009b, A&A, 505, 139

Carretta E., et al., 2010, ApJ, 722, L1

Carretta E., Lucatello S., Gratton R. G., Bragaglia A., D'Orazi V., 2011, A&A, 533, A69

Carretta E., D'Orazi V., Gratton R. G., Lucatello S., 2014, A&A, 563, A32

Carretta E., Bragaglia A., Lucatello S., Gratton R. G., D'Orazi V., Sollima A., 2018, A&A, 615, A17

Cassisi S., Salaris M., Pietrinferni A., Piotto G., Milone A. P., Bedin L. R., Anderson J., 2008, ApJ, 672, L115

Castelli F., 2005, Memorie della Societa Astronomica Italiana Supplementi, 8, 25

Chantereau W., Salaris M., Bastian N., Martocchia S., 2019, MNRAS, 484, 5236

Charbonnel C., Chantereau W., Krause M., Primas F., Wang Y., 2014, A&A, 569, L6

Choi J., Dotter A., Conroy C., Cantiello M., Paxton B., Johnson B. D., 2016, ApJ, 823, 102

Cohen J. G., 1978, ApJ, 223, 487

Cordero M. J., Pilachowski C. A., Johnson C. I., McDonald I., Zijlstra A. A., Simmerer J., 2014, ApJ, 780, 94

Cordoni G., Milone A. P., Marino A. F., Di Criscienzo M., D'Antona F., Dotter A., Lagioia E. P., Tailo M., 2018, ApJ, 869, 139

Cordoni G., Milone A. P., Mastrobuono-Battisti A., Marino A. F., Lagioia E. P., Tailo M., Baumgardt H., Hilker M., 2020, ApJ, 889, 18

Cottrell P. L., Da Costa G. S., 1981, ApJ, 245, L79

Cummings J. D., Geisler D., Villanova S., Carraro G., 2014, AJ, 148, 27

D'Antona F., Caloi V., 2008, MNRAS, 390, 693

D'Antona F., Caloi V., Montalbán J., Ventura P., Gratton R., 2002, A&A, 395, 69

D'Antona F., Bellazzini M., Caloi V., Pecci F. F., Galleti S., Rood R. T., 2005, ApJ, 631, 868

D'Antona F., Stetson P. B., Ventura P., Milone A. P., Piotto G., Caloi V., 2009, MNRAS, 399, L151

D'Antona F., Vesperini E., D'Ercole A., Ventura P., Milone A. P., Marino A. F., Tailo M., 2016, MNRAS, 458, 2122

D'Ercole A., Vesperini E., D'Antona F., McMillan S. L. W., Recchi S., 2008, MNRAS, 391, 825

D'Ercole A., D'Antona F., Ventura P., Vesperini E., McMillan S. L. W., 2010, MNRAS, 407, 854

D'Ercole A., D'Antona F., Vesperini E., 2016, MNRAS, 461, 4088

Dalessandro E., Lapenna E., Mucciarelli A., Origlia L., Ferraro F. R., Lanzoni B., 2016, ApJ, 829, 77

Dalessandro E., et al., 2018, ApJ, 864, 33

Decressin T., Meynet G., Charbonnel C., Prantzos N., Ekström S., 2007, A&A, 464, 1029

Denissenkov P. A., Hartwick F. D. A., 2014, MNRAS, 437, L21

Dondoglio E., Milone A. P., Lagioia E. P., Marino A. F., Tailo M., Cordoni G., Jang S., Carlos M., 2021, ApJ, 906, 76

Dondoglio E., et al., 2022, ApJ, 927, 207

Dondoglio E., et al., 2023, MNRAS, 526, 2960

Dorman B., 1992, ApJS, 80, 701

Dotter A., 2016, ApJS, 222, 8

Dotter A., Chaboyer B., Jevremović D., Kostov V., Baron E., Ferguson J. W., 2008, ApJS, 178, 89

Dotter A., et al., 2010, ApJ, 708, 698

Dotter A., Ferguson J. W., Conroy C., Milone A. P., Marino A. F., Yong D., 2015, MNRAS, 446, 1641

Fischer P., Welch D. L., Mateo M., 1992, AJ, 104, 1086

Fuentes-Carrera I., Jablonka P., Sarajedini A., Bridges T., Djorgovski G., Meylan G., 2008, A&A, 483, 769

Gaia Collaboration et al., 2018, A&A, 616, A1

Gaia Collaboration et al., 2021, A&A, 649, A1

Gieles M., et al., 2018, MNRAS, 478, 2461

Glatt K., et al., 2009, AJ, 138, 1403

Glatt K., et al., 2011, AJ, 142, 36

Goudfrooij P., et al., 2014, ApJ, 797, 35

Gratton R. G., Lucatello S., Carretta E., Bragaglia A., D'Orazi V., Momany Y. A., 2011, A&A, 534, A123

Gratton R. G., Carretta E., Bragaglia A., 2012a, A&A Rev., 20, 50

Gratton R. G., et al., 2012b, A&A, 539, A19

Halir R., Flusser J., 1998, in Skala V., ed., WSCG '98, VOL 1: SIXTH INTERNATIONAL CONFERENCE IN CENTRAL EUROPE ON COMPUTER GRAPHICS AND VISUALIZATION '98. pp 125–132

Han S.-I., Lee Y.-W., Joo S.-J., Sohn S. T., Yoon S.-J., Kim H.-S., Lee J.-W., 2009, ApJ, 707, L190

Harris W. E., 1996, AJ, 112, 1487

Ibata R., et al., 2021, ApJ, 914, 123

Iben Icko J., Rood R. T., 1970, ApJ, 161, 587

Jang S., et al., 2021, ApJ, 920, 129

Jang S., et al., 2022, arXiv e-prints, p. arXiv:2211.00650

Johnson C. I., Pilachowski C. A., 2010, ApJ, 722, 1373

King I., 1962, AJ, 67, 471

Kraft R. P., 1994, PASP, 106, 553

Kraft R. P., Sneden C., Langer G. E., Prosser C. F., 1992, AJ, 104, 645

Krause M., Charbonnel C., Decressin T., Meynet G., Prantzos N., 2013, A&A, 552, A121

Kroupa P., 2001, MNRAS, 322, 231

Kurucz R. L., 1970, SAO Special Report, 309

Kurucz R., 1993, SYNTHE Spectrum Synthesis Programs and Line Data. Kurucz CD-ROM No. 18. Cambridge, 18

Kurucz R. L., 2005, Memorie della Societa Astronomica Italiana Supplementi, 8, 14

Kurucz R. L., Avrett E. H., 1981, SAO Special Report, 391

Kuzma P. B., Da Costa G. S., Mackey A. D., 2018, MNRAS, 473, 2881

Lagioia E. P., et al., 2018, MNRAS, 475, 4088

Lagioia E. P., Milone A. P., Marino A. F., Cordoni G., Tailo M., 2019a, AJ, 158, 202

Lagioia E. P., Milone A. P., Marino A. F., Dotter A., 2019b, ApJ, 871, 140

Lagioia E. P., et al., 2021, ApJ, 910, 6

Lardo C., et al., 2012, A&A, 541, A141

Larsen S. S., Brodie J. P., Grundahl F., Strader J., 2014, ApJ, 797, 15

Latour M., et al., 2019, A&A, 631, A14

Lee J.-W., 2017, ApJ, 844, 77

Lee J.-W., 2018, ApJS, 238, 24

Lee J.-W., 2019, ApJ, 875, L27

Lee J.-W., Sneden C., 2020, arXiv e-prints, p. arXiv:2006.01274

Legnardi M. V., et al., 2023, MNRAS, 522, 367

Leitinger E., Baumgardt H., Cabrera-Ziri I., Hilker M., Pancino E., 2023, MNRAS, 520, 1456

Lindegren L., et al., 2018, A&A, 616, A2

Maíz Apellániz J., Úbeda L., 2005, ApJ, 629, 873

Marino A. F., Villanova S., Piotto G., Milone A. P., Momany Y., Bedin L. R., Medling A. M., 2008, A&A, 490, 625

Marino A. F., Milone A. P., Piotto G., Villanova S., Bedin L. R., Bellini A., Renzini A., 2009, A&A, 505, 1099

Marino A. F., et al., 2011a, A&A, 532, A8

Marino A. F., Villanova S., Milone A. P., Piotto G., Lind K., Geisler D., Stetson P. B., 2011b, ApJ, 730, L16

Marino A. F., et al., 2011c, ApJ, 731, 64

Marino A. F., et al., 2012, ApJ, 746, 14

Marino A. F., et al., 2014a, MNRAS, 437, 1609

Marino A. F., et al., 2014b, MNRAS, 442, 3044

Marino A. F., et al., 2015, MNRAS, 450, 815

Marino A. F., et al., 2017, ApJ, 843, 66

Marino A. F., et al., 2019a, MNRAS, 487, 3815

Marino A. F., et al., 2019b, ApJ, 887, 91

Marino A. F., et al., 2021, ApJ, 923, 22

Marino A. F., et al., 2023, ApJ, 958, 31

Martell S. L., Smolinski J. P., Beers T. C., Grebel E. K., 2011, A&A, 534, A136

Martocchia S., et al., 2018a, MNRAS, 473, 2688

Martocchia S., et al., 2018b, MNRAS, 477, 4696

Martocchia S., et al., 2019, MNRAS, 487, 5324

Mastrobuono-Battisti A., Perets H. B., 2013, ApJ, 779, 85

Mastrobuono-Battisti A., Perets H. B., 2016, ApJ, 823, 61

Mateo M., 1987, ApJ, 323, L41

McKenzie M., et al., 2022, MNRAS, 516, 3515

McLaughlin D. E., van der Marel R. P., 2005, ApJS, 161, 304

Michaud G., Vauclair G., Vauclair S., 1983, ApJ, 267, 256

Milone A. P., Marino A. F., 2022, Universe, 8, 359

Milone A. P., et al., 2008, ApJ, 673, 241

Milone A. P., Bedin L. R., Piotto G., Anderson J., 2009a, A&A, 497, 755

Milone A. P., Stetson P. B., Piotto G., Bedin L. R., Anderson J., Cassisi S., Salaris M., 2009b, A&A, 503, 755

Milone A. P., et al., 2010, ApJ, 709, 1183

Milone A. P., Piotto G., Bedin L. R., Cassisi S., Anderson J., Marino A. F., Pietrinferni A., Aparicio A., 2012a, A&A, 537, A77

Milone A. P., et al., 2012b, ApJ, 744, 58

Milone A. P., Marino A. F., Piotto G., Bedin L. R., Anderson J., Aparicio A., Cassisi S., Rich R. M., 2012c, ApJ, 745, 27

Milone A. P., et al., 2012d, ApJ, 754, L34

Milone A. P., et al., 2013, ApJ, 767, 120

Milone A. P., et al., 2014, ApJ, 785, 21

Milone A. P., et al., 2015, ApJ, 808, 51

Milone A. P., et al., 2016, MNRAS, 455, 3009

Milone A. P., et al., 2017a, MNRAS, 464, 3636

Milone A. P., et al., 2017b, MNRAS, 469, 800

Milone A. P., Marino A. F., Mastrobuono-Battisti A., Lagioia E. P., 2018a, MNRAS, 479, 5005

Milone A. P., et al., 2018b, MNRAS, 481, 5098

Milone A. P., et al., 2019, MNRAS, 484, 4046

Milone A. P., et al., 2020a, MNRAS, 491, 515

Milone A. P., et al., 2020b, MNRAS, 492, 5457

Monelli M., et al., 2013, MNRAS, 431, 2126

Mucciarelli A., Origlia L., Ferraro F. R., Pancino E., 2009, ApJ, 695, L134

Mucciarelli A., Bellazzini M., Merle T., Plez B., Dalessandro E., Ibata R., 2015, ApJ, 801, 68

Nardiello D., Milone A. P., Piotto G., Marino A. F., Bellini A., Cassisi S., 2015, A&A, 573, A70

Nardiello D., et al., 2018, MNRAS, 481, 3382

Nardiello D., Piotto G., Milone A. P., Rich R. M., Cassisi S., Bedin L. R., Bellini A., Renzini A., 2019, MNRAS, 485, 3076

Niederhofer F., et al., 2017, MNRAS, 465, 4159

Norris J., 1981, ApJ, 248, 177

Norris J., Freeman K. C., 1982, ApJ, 254, 143

Olszewski E. W., Saha A., Knezek P., Subramaniam A., de Boer T., Seitzer P., 2009, AJ, 138, 1570

Paxton B., Bildsten L., Dotter A., Herwig F., Lesaffre P., Timmes F., 2011, ApJS, 192, 3

Paxton B., et al., 2013, ApJS, 208, 4

Paxton B., et al., 2015, ApJS, 220, 15

Piotto G., et al., 2007, ApJ, 661, L53

Piotto G., et al., 2012, ApJ, 760, 39

Piotto G., et al., 2015, AJ, 149, 91

Platais I., Cudworth K. M., Kozhurina-Platais V., McLaughlin D. E., Meibom S., Veillet C., 2011, ApJ, 733, L1

Renzini A., 2023, MNRAS, 525, L117

Renzini A., et al., 2015, MNRAS, 454, 4197

Rich R. M., et al., 1997, ApJ, 484, L25

Richer H. B., Heyl J., Anderson J., Kalirai J. S., Shara M. M., Dotter A., Fahlman G. G., Rich R. M., 2013, ApJ, 771, L15

SAS Institute Inc. Staff C., 1988, SAS-STAT User's Guide: Release 6.03 Edition. SAS Institute Inc., USA

Sabbi E., et al., 2016, ApJS, 222, 11

Salaris M., Cassisi S., Pietrinferni A., 2008, ApJ, 678, L25

Salpeter E. E., 1955, ApJ, 121, 161

Sbordone L., Bonifacio P., Castelli F., Kurucz R. L., 2004, Memorie della Societa Astronomica Italiana Supplementi, 5, 93

Sbordone L., Bonifacio P., Castelli F., 2007, in Kupka F., Roxburgh I., Chan K. L., eds, IAU Symposium Vol. 239, Convection in Astrophysics. pp 71–73, doi:10.1017/S1743921307000142

Sbordone L., Salaris M., Weiss A., Cassisi S., 2011, A&A, 534, A9

Simioni M., Milone A. P., Bedin L. R., Aparicio A., Piotto G., Vesperini E., Hong J., 2016, MNRAS, 463, 449

Simpson J. D., Martell S. L., Navin C. A., 2017, MNRAS, 465, 1123

Smith G. H., Penny A. J., 1989, AJ, 97, 1397

Smith G. H., Tout C. A., 1992, MNRAS, 256, 449

Sneden C., Kraft R. P., Prosser C. F., Langer G. E., 1991, AJ, 102, 2001

Sollima A., Ferraro F. R., Bellazzini M., Origlia L., Straniero O., Pancino E., 2007, ApJ, 654, 915

Sollima A., Gratton R. G., Carballo-Bello J. A., Martínez-Delgado D., Carretta E., Bragaglia A., Lucatello S., Peñarrubia J., 2012, MNRAS, 426, 1137

Spitzer L., 1987, Dynamical evolution of globular clusters

Stetson P. B., 2005, PASP, 117, 563

Stetson P. B., Pancino E., Zocchi A., Sanna N., Monelli M., 2019, MNRAS, 485, 3042

Tailo M., Di Criscienzo M., D'Antona F., Caloi V., Ventura P., 2016, MNRAS, 457, 4525

Tailo M., et al., 2017, MNRAS, 465, 1046

Tailo M., D'Antona F., Caloi V., Milone A. P., Marino A. F., Lagioia E., Cordoni G., 2019a, MNRAS, 486, 5895

Tailo M., Milone A. P., Marino A. F., D'Antona F., Lagioia E. P., Cordoni G., 2019b, ApJ, 873, 123

Tailo M., et al., 2020, MNRAS,

Tautvaišienė G., et al., 2022, A&A, 658, A80

Trager S. C., Djorgovski S., King I. R., 1993, in Djorgovski S. G., Meylan G., eds, Astronomical Society of the Pacific Conference Series Vol. 50, Structure and Dynamics of Globular Clusters. p. 347

Ventura P., Caloi V., D'Antona F., Ferguson J., Milone A., Piotto G. P., 2009, MNRAS, 399, 934

Vesperini E., McMillan S. L. W., D'Antona F., D'Ercole A., 2010, ApJ, 718, L112

Vesperini E., McMillan S. L. W., D'Antona F., D'Ercole A., 2013, MNRAS, 429, 1913

Vesperini E., Hong J., Webb J. J., D'Antona F., D'Ercole A., 2018, MNRAS, 476, 2731

Villanova S., Geisler D., 2011, A&A, 535, A31

Villanova S., Geisler D., Piotto G., 2010, ApJ, 722, L18

Wang L., Kroupa P., Takahashi K., Jerabkova T., 2020, MNRAS, 491, 440

Yong D., Grundahl F., Nissen P. E., Jensen H. R., Lambert D. L., 2005, A&A, 438, 875

Yong D., Karakas A. I., Lambert D. L., Chieffi A., Limongi M., 2008, ApJ, 689, 1031

Yong D., Grundahl F., D'Antona F., Karakas A. I., Lattanzio J. C., Norris J. E., 2009, ApJ, 695, L62

Yong D., Grundahl F., Norris J. E., 2015, MNRAS, 446, 3319

Zennaro M., Milone A. P., Marino A. F., Cordoni G., Lagioia E. P., Tailo M., 2019, MNRAS, 487, 3239

Zoccali M., Pancino E., Catelan M., Hempel M., Rejkuba M., Carrera R., 2009, ApJ, 697, L22

de Mink S. E., Pols O. R., Langer N., Izzard R. G., 2009, A&A, 507, L1